Nonlinear localization, controlled transport and collapse suppression in Bose-Einstein condensates

A thesis submitted for the degree
of Doctor of Philosophy of
The Australian National University

Jasur A. Abdullaev

Canberra
July 23 2014

Declaration

This thesis is an account of research undertaken in the Nonlinear Physics Centre within the Research School of Physical Sciences and Engineering at the Australian National University between June 2009 and February 2014 while I was enrolled for the Doctor of Philosophy degree.

The research has been conducted under the supervision of Prof. Yuri S. Kivshar, Dr. Elena A. Ostrovskaya, and Dr. Anton S. Desyatnikov. However, unless specifically stated otherwise, the material presented within this thesis is my own.

None of the work presented here has been submitted for any degree at this or any other institution of learning.

Jasur A. Abdullaev
July 2014

Jasur

List of publications

1. Jasur Abdullaev, Dario Poletti, Elena A. Ostrovskaya, and Yuri S. Kivshar, *"Controlled transport of matter waves in two-dimensional optical lattices"*, Physical Review Letters **105** 090401 (2010).

2. Jasur Abdullaev, Anton S. Desyatnikov and Elena A. Ostrovskaya, *"Suppression of collapse for matter waves with orbital angular momentum"*, Journal of Optics **13** 064023 (2011).

3. Elena A. Ostrovskaya, Jasur Abdullaev, Anton S. Desyatnikov, Michael D. Fraser, and Yuri S. Kivshar, *"Dissipative solitons and vortices in polariton Bose-Einstein condensates"*, Physical Review A **86** 013636 (2012).

4. Elena A. Ostrovskaya, Jasur Abdullaev, Anton S. Desyatnikov, Michael D. Fraser, and Yuri S. Kivshar, *"Self-localization of polariton condensates in periodic potentials"*, Physical Review Letters **110** 170407 (2013).

Conference presentations and proceedings

1. Jasur Abdullaev, Dario Poletti, Elena A. Ostrovskaya, and Yuri S. Kivshar, *"Transport and stability of two-dimensional matter-wave solitons in a driven optical lattice"*, Australasian Conference on Optics, Lasers and Spectroscopy and the Australian Conference on Optical Fibre Technology in association with the International Workshop on Dissipative Solitons (ACOLS ACOFT), ed. Australian Optical Society, Australian Optical Society, Adelaide, Australia, p. 2 (2009).

2. Jasur Abdullaev, Dario Poletti, Elena A. Ostrovskaya, and Yuri S. Kivshar, *"Dynamical transport control of matter waves in two-dimensional optical lattices"*, 22nd International Conference on Atomic Physics (ICAP), Cairns, Tropical North Queensland, Australia, p. 191 (2010).

3. Jasur Abdullaev, Anton S. Desyatnikov, and Elena A. Ostrovskaya, *"Collapse suppression in Bose-Einstein condensate clouds with orbital angular momentum"*, Lasers and Electro-Optics Europe (CLEO EUROPE/EQEC), Conference on and 12th European Quantum Electronics Conference (CLEO EUROPE/E-QEC), Munich, Germany, (2011). DOI:10.1109/CLEOE.2011.5943309

4. Jasur Abdullaev, Anton S. Desyatnikov, and Elena A. Ostrovskaya,*"Matter waves with orbital angular momentum: Collapse suppression and bistability"*, Quantum Electronics Conference and Lasers and Electro-Optics (CLEO/IQEC/PACIFIC RIM), Sydney, Australia, pp.114-115, (2011). DOI:10.1109/IQEC-CLEO.2011.6194020

Ackowledgements

First of all, I would like to thank my supervisors, Prof. Yuri Kishar, Dr. Elena Ostrovskaya and Dr. Anton Desyatnikov. Each of my supervisors have always been ready to make time to see me no matter how busy they are personally. Their guidance and advice has been invaluable. I would especially like to thank Dr. Ostrovskaya for her patience and support. I am sincerely thankful to her for spending so much time going through my work, especially when she was so busy with other things.

And of course, none of this would be complete without mentioning other members of the Nonlinear Physics Centre, both past and present - Kathy Hicks,David Powell, Ilya Shadrivov, Yana Izdebskaya, Vladlen Shvedov, Dragomir Neshev, Alexander Minovich, Arthur Davoyan, Andrey Miroshnichenko, Andrey Sukhorukov, Alexander Solntsev, and Diana Antonosyan who have kept me going through the years. And a big thanks to people outside of the Nonlinear Physics Centre as well - Ali Hennawi, Haitham, Khalil, and Ahsan.

I would also like to thank my family who have supported me for all these long years of my PhD. Even though they did not have much idea what exactly I was studying they had faith enough in me to say "Go and do what you feel is best for you". So big thanks to my parents, to my two sisters and to my wife.

No matter where life eventually leads us, I will always remember you all.

Abstract

This thesis includes theoretical studies regarding stability and manipulation of Bose-Einstein condensates (BECs) of ultra-cold atoms in 2D trapping geometry, as well as formation of steady states of exciton-polariton Bose-Einstein condensates created in solid states. We analyze and numerically model the dynamics and localization of the condensates using mean-field model.

Chapter 1 contains an introduction to the physics of ultra-cold atom BEC and exciton-polariton BEC which provides a framework for the work presented in later chapters.

In *Chapter 2*, we consider a method for achieving dynamically controllable transport of highly mobile matter-wave solitons in an ultra-cold atom BEC with attractive interparticle interaction loaded into a driven two-dimensional optical lattice. Our numerical analysis based on the mean-field model and the theory based on the effective particle approach demonstrate that fast, time-periodic rocking of the two-dimensional optical lattice enables efficient stabilization and manipulation of spatially localized matter wave packets via induced reconfigurable mobility channels.

Chapter 3 consists of an investigation of the instability - collapse of a BEC with attractive interactions. In this chapter we explore the influence of an orbital angular momentum on the collapse of vortex-free elliptic clouds of Bose-Einstein condensates trapped in a radially symmetric harmonic potential or a rotating elliptic potential. The results of our analysis show that the number of trapped ultracold atoms corresponding to the collapse threshold can be radically increased for such rotating nonlinear matter waves in a radially harmonic trap. The results corresponding to a BEC cloud confined in a rotating elliptic trap show that the elongated stationary states can be parallel or perpendicular to the long axis of the trap and display bistable nature.

In *Chapter 4*, we examine spatial localization and dynamical stability of Bose-Einstein condensates of exciton-polaritons in microcavities under the condition of off-resonant spatially inhomogeneous optical pumping both with and without a harmonic trapping potential. We employ the open-dissipative Gross-Pitaevskii model for describing an incoherently pumped polariton condensate coupled to an exciton reservoir. We reveal that spatial localization of the steady-state condensate occurs due to effective self-trapping created by the polariton flows, regardless of the presence of the external potential. A ground state of the polariton condensate with repulsive interactions between the quasi-particles represents a dynamically stable bright dissipative soliton. We also investigate the conditions for sustaining spatially localized structures, with nonzero angular momentum, in the form of single-charge vortices.

Chapter 5 consider the existence of novel spatially localized states of exciton-polariton Bose-Einstein condensates in semiconductor microcavities with fabricated periodic in-plane potentials. Our theory shows that, under the conditions of continuous nonresonant pumping, localization is observed for a wide range of optical pump parameters due to effective potentials self-induced by the polariton flows in the spatially periodic system. We show that the self-localization of exciton-polaritons in the lattice may occur both in the gaps and bands of the single-particle linear spectrum, and is dominated by the ef-

fects of gain and dissipation rather than the structured potential, in sharp contrast to the conservative condensates of ultra-cold alkali atoms.

Contents

Chapter 1

Introduction

1.1 Preliminary remarks

The prediction by Albert Einstein of a new form of matter, which would appear at extremely low temperatures, was the result of his correspondence with Indian scientist Satyendra Nath Bose in 1920th. In this *Bose-Einstein condensate*, or BEC, a macroscopic number of noninteracting atoms would occupy the same quantum state (see [1] and references therein). Although basic theoretical description of BEC dates back to mid-1920s, it was experimentally realized for alkali atom gases in 1995 [2–4]. In 2006 realization of another novel type of BEC was announced [5]. Unlike atomic gas BEC, this condensate was observed for bosonic quasiparticles inside semiconductor microcavities. These quasiparticles, named exciton-polaritons, have become pioneers in formation of BECs in solid state systems.

Both mentioned types of BEC are nonlinear physical systems due to inter-particle interactions, and therefore differ from the Einstein's prediction. However, it was shown that these BECs do correspond to a macroscopically occupied quantum state and can be represented by a macroscopic wavefunction [6, 7]. Thus, BEC could be used to study nonlinear phenomena [7–14]. Moreover, high sensitivity of BECs to external potentials and fields, and the possibility to tune their nonlinearity [10, 11, 15], make these systems very attractive from the viewpoint of both fundamental studies and applications.

In this thesis, we consider special nonlinear collective excitations of the condensate such as solitons and vortices. Solitons are in the centre of attention because of their ability to self-localize and evolve preserving their shape [16]. There has been special interest in solitons because of their ability to transport information, especially in nonlinear optics [16, 17]. On the other hand, vortices are important in understanding the effects of rotations in BECs since they have great relevance to physics of superfluids [7, 13, 14].

The aim of this introductory chapter is to summarise the most relevant and basic physical concepts related to atomic gas and exciton-polariton BECs, which form the foundation of the work we present in this thesis. The multifaceted nature of the subject of this thesis is reflected by the layout of this introductory chapter. The chapter is divided into nine sections-Bose Einstein condensates of ultra-cold atoms, trapping and manipulation of atoms, the Gross-Pitaevskii equation, collapse of BEC with attractive interaction, Bose-Einstein condensate of exciton-polaritons, off-resonant, incoherent excitation schemes, trapping techniques of exciton-polaritons, open dissipative Gross-Pitaevskii equation and similarities and difference with BECs of ultra-cold atoms. We aim to explain each section in a general introductory manner with a basic physical concepts, and then giving an introduction to the underlying physics and the mathematical models used in our work. In each section, we try to tie in new concepts with previously introduced material.

We also briefly discuss the theoretical formalism based on the mean-filed approximation that allows us to describe a large variety of nonlinear effects.

1.2 Bose-Einstein condensate of ultra-cold atoms

1.2.1 A Historical Perspective

In 1924, Indian physicist Satyendra Nath Bose wrote a paper rederiving Plank's quantum radiation law with novel approach-assuming photons as identical particles. He had difficulties to publish the paper, and sent it directly to Albert Einstein. Recognizing the importance of the paper, Einstein translated and submitted it to the prestigious journal "Zeitschrift für Physik" on behalf of Bose. In 1924-25 Einstein extended Bose's work for massive particles - atoms, and came to the result which is well-known today as Bose-Einstein statistics. Analysing the obtained result, Einstein noticed a curious feature and predicted a unique phase transition for massive bosonic particles. At very low but limited temperature, a macroscopic fraction of particles "condenses" into lowest-energy single-particle quantum state. This famous state nowadays is known as Bose-Einstein condensate or BEC. References to the original papers by Bose and Einstein are given in [6]. The early history of BECs is discussed in [1].

Initially Einstein's prediction had no impact in practice. In 1938, the discovery of superfluidity in liquid ^{4}He was announced by the Kapitza group in Moscow and the lab led by Allen and Misener in Cambridge. Fritz London immediately tried to link and explain superfluidity as a manifestation of Bose-Einstein condensation. A combination of new experimental results and the theoretical work of London reignited interest in BEC. From this point on, until the 1960s, liquid ^{4}He was the only candidate for theoretical and experimental work on BEC. However, strong interaction of atoms in liquid ^{4}He prevented the observation of the condensate. Enormous volume of theoretical work was done to understand similarities and differences between BEC and superfluid ^{4}He. In 1941 Landau developed the theory for superfluids. In 1947 Bogolubov followed and wrote the first macroscopic theory for interacting Bose gases. Experiments on superfluid ^{4}He developed and became more accurate in the same years (see [1, 18] and references therein).

To delineate the behaviour of the liquid ^{4}He from that of a BEC, theoreticians begun studying condensation in weakly interacting dilute alkali gases. The experiments on dilute gases also began in 1970s in search of a pure BEC. Spin-polarised hydrogen became the initial favorite candidate. However, significant problems, which were not overcome until 1998 [19], caused that attention to shift to dilute alkali gases such as ^{7}Li, ^{23}Na and ^{87}Rb. Development of new techniques in atom physics, namely, trapping atoms with magnetic and optical traps and advanced cooling mechanisms for atoms, led to experimental studies towards realization of a BEC. In 1980s, laser cooling and optical trapping techniques were developed to cool and trap neutral atoms (see Section 1.2.3 and Section 1.2.4). It was relatively easy to use laser cooling methods for neutral alkali atoms, as their optical transition and internal energy-level structure were favourable for cooling with available lasers. In 1995, a combination of laser cooling with improved trapping and evaporative cooling led to the announcements of successfull creation of BECs in dilute gases. Three different groups achieved realization of an atomic BEC:

- ^{87}Rb, Joint Institute for Laboratory Astrophysics (JILA) [2], see Figure 1.1.
- ^{23}Na, Massachusetts Institute of Technology (MIT) [3],

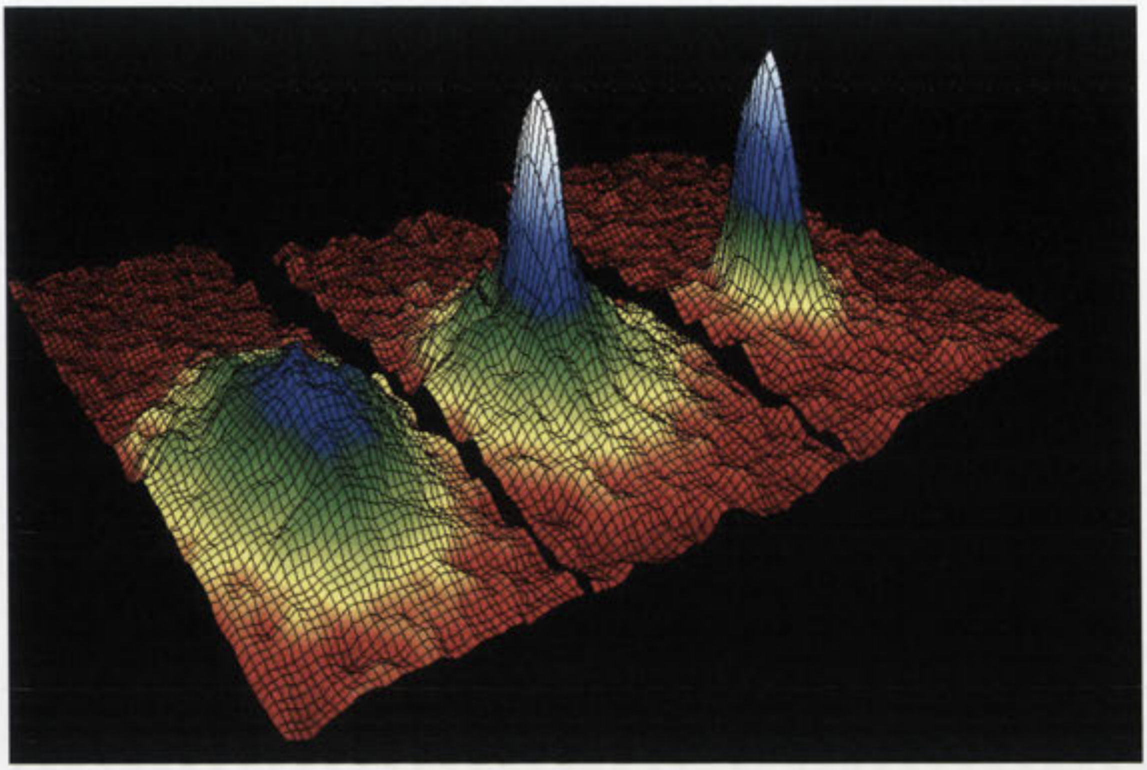

Figure 1.1: Images of the velocity distributions of the trapped ^{87}Rb atoms, taken by the expansion method in the experiment by Anderson *et.al* [2, 25]. The left frame shows the velocity distribution just before the appearance of the Bose-Einstein condensate at $T \sim 400$ nK; the center frame, just after the appearance of the condensate at $T \sim 200$ nK; the right frame, after further evaporation leaves a sample of nearly pure condensate, $T \sim 50$ nK. The size of each frame is 200μm x 270μm, and corresponds to the distance the atoms have moved in about $1/20s$. The color corresponds to the number of atoms at each velocity, with red being the fewest atoms and white being the most. Areas appearing white and light blue indicate lower velocities. (Figure is taken from [25]).

- ^{7}Li, Rice University [4].

Since 1995, there has been an explosive growth in the study of BECs. In spite of being closer to Einstein's original prediction than liquid ^{4}He, BECs of dilute alkali gases still show some features differing from that prediction. They are trapped, interacting and inhomogeneous. Thanks to these features, a BEC can be realized not only in momentum space but also in coordinate space, opening possibility for direct experimental investigations. Experimental behaviour that have been observed so far in BECs include: interference fringes [20], solitons [8–12, 14, 21], vortices [13, 22], and trapping in potentials of various geometry [12, 23, 24]. It is also interesting to point out that a BEC of dilute gases, within a certain approximation, can be described as a macroscopic wavefunction with nonlinearity due to interaction between atoms. In the mean-field approximation, it can be treated as analogous to light wave in a medium with Kerr-type nonlinearity.

1.2.2 Basic physical concepts

Particles are divided into bosons and fermions based on their net spin. When Einstein described the BEC in 1924-25, the division of particles was not well known. However, the properties of matter waves he considered were soon recognised to be those of bosons.

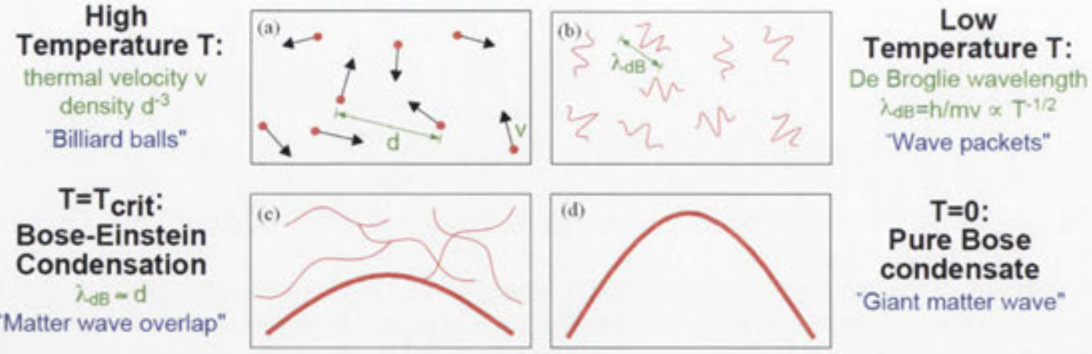

Figure 1.2: T-temperature, T_{crit}- critical temperature for BEC, and λ_{dB} is de Broglie wavelength. (a) $T \gg T_{crit}$: Atoms behave like particles. d is the mean distance between atoms at temperature T. (b) As T decreases, λ_{dB} increases. (c) $T = T_{crit}$: The atomic wavepackets begin to overlap, forming BEC. (d) At $T = 0$, all atoms are in the condensate which is a giant matter-wave. Figure is taken from [26].

The question, which we address in this section, is: why does a BEC occur, i.e. why do bosons "cluster" together into single-particle quantum state?

In classical mechanics, identical particles are treated as distinguishable, meaning that they can be labelled. However, in quantum physics bosons and fermions are treated as indistinguishable, meaning that they can not be labelled. This assumption of indistinguishability leads to counterintuitive result which can be seen even in the simple two-particle, two state example. The probability of having both particles in the same state is $1/2$ in the classical case (distinguishable particles). However, the probability of having both particles in the same state is increased to $2/3$ in the quantum case (indistinguishable particles). The simple fact of indistinguishability of particles leads to increase in the statistical weighting for the cases where a larger number of particles are in the same state. The effect becomes especially important in the degenerate case, where the number of particles, N, is greater than or equal to the number of possible states, i. This effect is generic for bosons as there are no restriction on the number of particles which can be in the same state. Unlike bosons, fermions obey the Pauli exclusion principle which means that no two fermions can be in the same quantum state. Thus fermions do not experience the clustering effect.

The clustering effect for bosons can be mathematically represented by the Bose-Einstein distribution. For non-interacting bosons at thermal equilibrium, without restriction on the number of particles in the same state, the mean number of atoms n_i, in state i with energy ϵ_i at temperature T is given by [27]:

$$n_i = \{\exp[\beta(\epsilon_i - \mu)] - 1\}^{-1} \tag{1.1}$$

where $\beta = (k_B T)^{-1}$, k_B is the Boltzmann's constatnt and μ is an important parameter known as the *chemical potential* (see Section 1.4.1). It is fixed by the condition:

$$\sum_i n_i(\mu, \beta) = N, \tag{1.2}$$

where chemical potential, μ, is very large and negative for high temperatures. As T lowers, μ increases [28]. It is clear from Equation (1.1) that eventually, at certain temperature,

T_c, the occupation of the lowest energy single-particle state is of the order N. At this point the Bose-Einstein condensate is achieved.

Bose-Einstein condensation of ultra cold atoms can be explained with a scheme in Figure 1.2. At high temperature, atoms of dilute gas behave classically. As long as the distance between atoms is large compared to the atom's de Broglie wavelength, $\lambda_{dB} = (2\pi\hbar^2/mk_BT)^{1/2}$, one can describe them as that of classical objects, for instance billiard balls or marbels. De Broglie wavelength is the uncertainty in position connected to thermal momentum distribution. When the temperature, T, decreases, de Broglie wavelength increases. Quantum degeneracy of atoms begins when distance between atoms, d, becomes comparable to λ_{dB}. At this point, atoms' wavepackets begin to overlap, and a condensation emerges. As the temperature approaches zero, the thermal cloud disappears, and pure condensate forms.

1.2.3 A brief overview of cooling processes

The mean interparticle distance can be found from the density of the gas as $n^{-1/3}$. The condition for BEC condensation is: $\lambda_{dB} \sim n^{-1/3}$. It can be rewritten as $\rho = n\lambda_{dB}^3 \sim 1$, where ρ is known as *phase-space density*. To achieve a BEC, it is essential to increase ρ. For example, in order to realize sodium BEC, the phase-space density is increased by *13-20 orders of magnitude* [26]. This is achieved by using a combination of laser cooling and evaporative cooling.

Laser cooling.

It is well known that when an atom absorbs a photon, it receives a momentum "kick" known as "radiation pressure". The atom reemits the energy from the absorbed photon through spontaneous emission. Since spontaneous emission is random, the received net momentum change of the atom is entirely from the absorbed photon, namely h/λ in the direction that the absorbed photon was travelling. Here h is Planck's constant and λ the photon wavelength. This process is the most efficient when the light is at *resonance* with the atom. Spontaneous emission related radiation pressure is the only type of radiative force.

In mid 1970s, Doppler cooling of atoms was first suggested [29–31]. Two counter-propagating laser beams, both with frequencies ω, slightly shifted below resonance, were involved in the simplest case. A stationary atom in the light field will feel equal momentum kicks from both directions and hence remain stationary. However, a moving atom will see the light from the beam it is moving towards Doppler shifted closer to resonance, while the light from the other beam is Doppler shifted further away from resonance. This means that the moving atom receives a net momentum kick opposite to the direction it is travelling. As a result, the moving atom slows down. By using three pairs of counterpropagating laser beams, the atoms can be slowed down in every direction, thus cooling the gas. This six beam configuration is known as *optical molasses* [29–31].

Evaporative cooling.

Laser cooling itself is not sufficient to cool atom gases to the BEC transition. The magnitude of phase-space density required to create a BEC can be achieved using another type of cooling known as *evaporative cooling*.

The technique of evaporative cooling was first developed and used for cooling spin-polarized hydrogen atoms [32]. The basic principle of evaporative cooling is very familiar - we see it at work every day when a cup of hot coffee or tea cools down. The temperature of a gas is proportional to the average kinetic energy of the atoms. By removing atoms with the highest energy, the average kinetic energy can be decreased, and hence the temperature of the gas is lowered. Radio-frequency induced spin flips [3] are often used to remove the most energetic atoms from the gas in a magnetic trap. When radio-frequency radiation is at resonance with the atoms, a spin flip occurs. The trapping potential for the atoms formed by the magnetic field effectively bends over to form a "lip", which allows the most energetic atoms to escape. The potential height where the "lip" occurs can be controlled with applied radio-frequency radiation. The process is repeated until the temperature is low enough for a BEC to form.

1.3 Trapping and manipulation of atoms

Cooling and manipulation of atoms are the most important steps towards realization of Bose-Einstein condensates of alkali atom gases. To reach the condensation phase, atoms should be cooled close to the absolute zero temperature. Therefore, the term "BEC of ultracold atoms" is widely used in literature. Advances in laser physics provided new powerful methods for manipulating and trapping alkali atom vapours [33–39]. In the following sections we describe some experimental techniques related to trapping and manipulation of ultracold atoms.

1.3.1 Influence of magnetic field on atom

Magnetic fields are often used for trapping laser-cooled atom gases [2–4, 32]. Magnetic trapping of neutral atoms is based on the Zeeman effect. Atoms with the magnetic moment $\mu_{\mathbf{B}}$ placed in a magnetic field show a split of sharp spectral lines into several lines. The sign of the interaction energy E_B between atoms and magnetic field, $\mathbf{B}$, depends on the mutual alignment of the atomic magnetic moment $\mu_{\mathbf{B}}$ and $\mathbf{B}$:

- If $\mu_{\mathbf{B}}$ and $\mathbf{B}$ are paralell, atoms are high field seeking $\rightarrow E_B < 0$.
- If $\mu_{\mathbf{B}}$ and $\mathbf{B}$ are anti-paralell, atoms are low field seeking $\rightarrow E_B > 0$.

According to Earnshaw's theorem [40], neutral atoms are only trapped in a minimum of static magnetic fileds. Thus, only low field seeking atoms can be trapped.

Usually the magnetic trapping potentials, $V_B(\mathbf{r})$, are approximated by isotropic or highly anisotropic harmonic potentials:

$$V_B(\mathbf{r}) = \frac{1}{2}m(\omega_x^2 x^2 + \omega_y^2 y^2 + \omega_z^2 z^2), \tag{1.3}$$

where m is the atomic mass and $\omega_{x,y,z}$ are harmonic oscillator (trap) frequencies in x, y and z direction, respectfully.

1.3.2 Influence of laser field on atom

The exploitation of atom's interaction with an off-resonance laser field can be used as the main tool for manipulating the condensate in experiments [37–39]. We give here a general description of the interaction of an atom with a radiation field.

The typical atomic size is small compared to laser radiation wavelength. So the interaction between an atom and the electric field can be written, with high accuracy, in the dipole approximation [41, 42]:

$$\hat{H}_{\text{dip}} = -\hat{\mathbf{d}}\cdot \mathbf{E}(\omega, t), \tag{1.4}$$

where $\hat{\mathbf{d}} = e\hat{\mathbf{r}}$ is dipole moment operator for an atom and

$$\mathbf{E}(\omega, t) = \mathbf{E}_{\omega} e^{-i\omega t} + \mathbf{E}_{-\omega} e^{-i\omega t} \tag{1.5}$$

is time dependent electric field vector with frequency ω and amplitude $\mathbf{E}_{\omega}$. The interaction creates a dipole polarizability in the atom electronic structure which oscillates with the frequency of the laser field. The general form of this dynamical polarizability can be expressed by using the perturbation theory [41, 42],

$$\alpha(\omega) = \hbar^{-1} \sum_{e} |\langle e|\hat{\mathbf{d}}\cdot \hat{\epsilon}|g\rangle|^2 \frac{2\omega_{eg}}{\omega_{eg}^2 - \omega^2}, \tag{1.6}$$

where $|g\rangle$ and $|e\rangle$ are ground and excited states respectively, $\omega_{eg} = (E_e - E_g)/\hbar$ is atomic transition frequency, and $\hat{\epsilon}$ is a unit vector in the direction of electric field. Because of this polarization, the energy of the system will change. This energy change can be considered as the effective potential felt by atoms. If we assume that the polarizability is dominated by a single resonant frequency, the expression above can be reduced to a single term. Taking into account the spontaneous emission rate of the excited level, one can derive the polarizability and the effective potential in the following form [42, 43],

$$\alpha(\omega) = \hbar^{-1} |\langle e|\hat{\mathbf{d}}\cdot \hat{\epsilon}|g\rangle|^2 \frac{(\omega_{eg} - \omega)}{(\omega_{eg} - \omega)^2 + (\Gamma_e/2)^2} \tag{1.7}$$

$$V_{\text{dip}} = -\frac{1}{2}\alpha(\omega)\overline{\mathbf{E}(\omega, t)^2}, \tag{1.8}$$

where Γ_e denotes the spontaneous emission rate of the excited state and the bar over the time dependent electric field denotes a time average. Equation (1.8) shows that the effective potential is proportional to the the intensity of the light field ($I \approx |\mathbf{E}|^2$). For futher convenience of analysis we introduce the *detuning*, which is the difference between atomic transition frequency and laser frequency, $\delta = \omega - \omega_{eg}$. Then the effective potential will have the following form [42, 43],

$$V_{\text{dip}} = \hbar^{-1} |\langle e|\hat{\mathbf{d}}\cdot \hat{\epsilon}|g\rangle|^2 |\mathbf{E}_{\omega}|^2 \frac{\delta}{\delta^2 + \Gamma_e^2/4} = \frac{\hbar\Omega_R^2 \delta}{\delta^2 + \Gamma_e^2/4}, \tag{1.9}$$

$$\Omega_R = |\langle e|\hat{\mathbf{d}}\cdot \mathbf{E}_{\omega}|g\rangle|/\hbar, \tag{1.10}$$

here Ω_R is *Rabi frequency*, the magnitude of the perturbing matrix element.

Influence of laser field on atom energy levels opens possibility to use optical dipole traps as tools for manipulation of BEC atoms [38, 39].

One of the main advantages of using optical traps instead of magnetic traps to confine BECs is that they are independent of the hyperfine spin state of the atom. Magnetic traps are state-dependent and they trap only low field seeking states [32].

Another advantage of using optical traps is that their shape is extremely flexible and

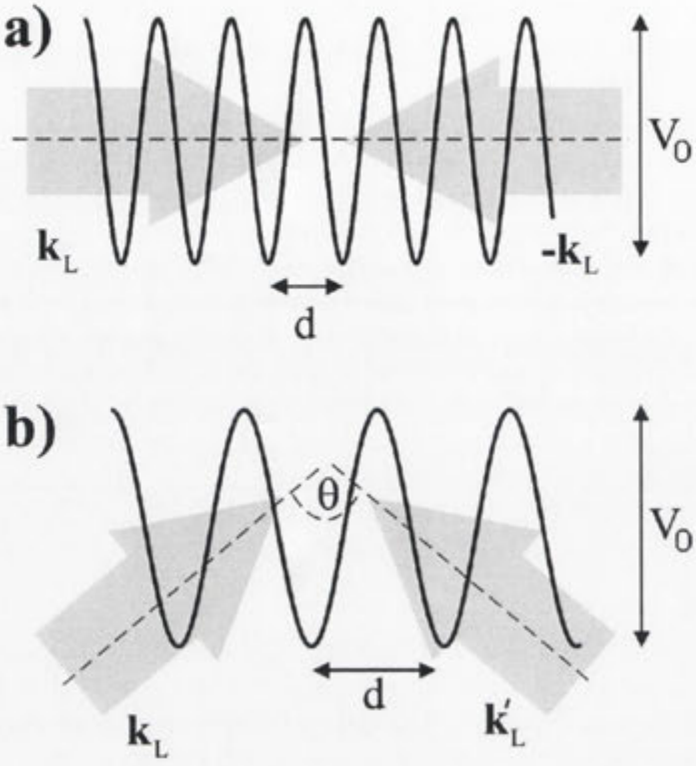

Figure 1.3: (a) A one-dimensional optical lattice created with counter-propagating laser beams, and (b) with beams enclosing an angle θ. The parameters V_0 (lattice height), d (lattice periodicity), and k_L (the wave number of laser beams) are defined in the text [45].

relatively easy to control. Depth of optical traps are directly proportional to the light field intensity. Hence, the optical trap properties, such as trapping strength, and shape of the trapping potential can be controlled by manipulating the light field [44]. Optical lattices are good examples of such flexibility.

1.3.3 Optical lattices

Optical lattices (OL) are standing light waves created by a pair, or pairs, of counter-propagating laser beams. Ultra-cold atoms can be trapped in the nodes or antinodes of the lattice due to the effective potential described in previous section. As an illustrative example, let us consider $E_1(x,t)$ and $E_2(x,t)$ as laser fields with the same polarization, wavelength λ, and amplitude E_0, counterpropagating in x direction. The superposition of these two fields produces the standing wave:

$$E(x,t) = E_0 e^{-i(\omega t - k_L x)} + E_0 e^{-i(\omega t + k_L x)} = 2E_0 \cos(k_L x) e^{-i\omega t}, \tag{1.11}$$

where $k_L = 2\pi/\lambda$ is the wave number of laser beams. Then, substituting this electric field into Equation (1.8), the effective potential $V_{\rm dip}$ along x is,

$$V_{\rm dip} = V_{\rm OL} = V_0 \cos^2(k_L x). \tag{1.12}$$

This is a 1D single periodic cosinusoidal potential with periodicity $d = \lambda/2$ and lattice height, $V_0 \propto V_{\rm dip} \propto I_{max}/\delta$ where I_{max} $|E|^2$ is the maximum intensity of laser field. We can trivially replace $\cos^2(k_L x)$ with $\sin^2(k_L x)$. If the two beams are slightly tilted, the periodic potential along x direction is given by $V_{OL} = V_0 \sin^2(Kx)$, where $K = k_L \sin(\theta/2)$. Hence, the periodicity is $d = \lambda/[2\sin(\theta/2)]$ [45, 46].

When lasers are blue-detuned ($\delta > 0$), created potensials are repulsive and atoms are trapped in the nodes of the standing wave. When lasers are red-detuned ($\delta < 0$), created potensials are attractive and atoms are trapped in the anti-nodes of the standing wave.

2D periodic potentials can be created with similar approach involving two pairs of counterpropagating laser beams. Analytical form of 2D OL potential can be approximated as:

$$V_{\rm OL} = V_x \cos^2(k_y x) + V_y \cos^2(k_y y), \tag{1.13}$$

where V_x, V_y are the lattice heights, and k_x, k_y are the wave numbers in x and y dimensions respectively [44–46].

As described above, the main properties of optical lattices are determined by the trapping lasers. Two- or three-dimensional lattices of more sophisticated shape can be created by adding more laser pairs. The lattice periodicity, d, can be tuned by changing laser wavelength, λ, and/or the angle between lasers, θ. The height of the lattice can be controlled by changing the maximum intensity. Furthermore, introducing a small frequency difference between trapping lasers and changing it in time produces velocity and acceleration of the optical lattice. Besides their flexibility, these light induced periodic potentials are largely defect-free systems. In this thesis, we consider *two-dimensional driven optical lattices* to describe controlled 'manipulation of Bose-Einstein condensates (Chapter 2).

1.3.4 Interatomic interaction

BECs are not ideal gases due to interactions between atoms. The theory of weakly interacting Bose gas was developed from late 1940s to early 1960s (see [1] and references therein). In a dilute and cold gas, collisions in the system can be characterized by *s-wave scattering length*, which represents the key interaction parameter [41, 43].

Binary collisions and s-wave scattering length

One of the important criteria for metastability of the BEC phase is the prevailing role of binary (elastic) collisions in comparison to the three-body (inelastic) collisions. Suppression of inelastic collisions, in particular three-body recombination, by the diluteness of the gas allows the system to be in kinetic equilibrium with respect to binary collisions [41, 43].

Binary collisions can be described by elastic scattering theory. Let us consider collision of two particles of mass m_1 and m_2. The task is to calculate scattering amplitude. To simplify the problem, we transform to the centre-of-mass reference frame and relative coordinates. The wave function of the center-of-mass is a plane wave and satisfies Schrödinger equation for the relative motion with reduced mass $m_r = m_1 m_2/(m_1 + m_2)$. The wave function of relative motion can be described as the sum of incoming plane wave and outgoing scattered wave,

$$\psi = e^{ikx} + f(\theta)\frac{e^{ikr}}{r}, \tag{1.14}$$

where $f(\theta)$ is the scattering amplitude, and k is the wave number. The wave function is written with assumption that interatomic distance is large and interaction between atoms is spherically symmetric. Hence, scattering wave is spherical and the amplitude depends only on the scattering angle θ between direction of r and the x axis. The energy of the state is given by

$$E = \frac{\hbar^2 k^2}{2m_r}. \tag{1.15}$$

At very low energies the scattering amplitude $f(\theta)$ tends to a constant, which we denote by a_s, and the wave function ψ becomes

$$\psi = 1 - \frac{a_s}{r}. \tag{1.16}$$

The constant value, a_s, is called the *s-wave scattering length* [41, 43]. This constant is determined by the potential of interaction between atoms. Since the interatomic potential is spherically symmetric, the solution of the Schrödinger equation has an axial symmetry with respect to the direction of the incoming atom. It allows us to write the scattering amplitude in terms of a partial wave expansion,

$$f(\theta) = \frac{1}{2ik}\sum_l^{\infty}(2l+1)(e^{2i\delta_l}-1)P_l(\cos\theta), \tag{1.17}$$

where $P_l(\cos\theta)$ is Legendre polynomials, l is orbital angular momentum and δ_l is constant value. The low temperature and the diluteness of BEC atoms allows us to retain only first term ($l=0$) in the expansion (1.17).

Taking into account scattering only with $l=0$ (s-wave), one can calculate total cross section for atom scattering defined as $\sigma = 8\pi a_s^2$. Assuming that a_s is much smaller than distance between atoms, interatomic interaction potential $V_{\text{int}}(\mathbf{r})$ can be replaced with a delta-function effective interaction,

$$V_{\text{int}}(\mathbf{r}) = g\delta(\mathbf{r}), \tag{1.18}$$

where coupling constant or *nonlinearity constant* g, depends on the a_s, as follows [6, 41, 43],

$$g = \frac{4\pi\hbar^2 a_s}{m}. \tag{1.19}$$

The effective interaction potential simplifies theoretical description of the BEC allowing the interatomic interaction to be characterised by single experimental parameter, a_s. The s-wave scattering length can be experimentally controlled and tuned using Feshbach resonances. If $a_s > 0$, interatomic interaction is repulsive, for $a_s < 0$ interatomic interaction is attractive. The stability of large condensates requires repulsive interactions. For attractive interactions, the condensate is unstable against *collapse* above a certain size, i.e. number of atoms (see Section 1.7).

1.4 The Gross-Pitaevskii equation

In the framework of the mean-field theory, dynamics of the condensate wavefunction can be well described by the Gross-Pitaevskii equation (GPE). In this section we will review a standard derivation of this equation.

In quantum theory, the system of N interacting bosons with mass m trapped in external potential V_{ext}, can be described by the Hamiltonian in the second quantized form [6]:

$$\hat{H} = \int d\mathbf{x}\hat{\Psi}^\dagger(\mathbf{x})\left[-\frac{\hbar^2}{2m}\nabla^2 + V_{\text{ext}}(\mathbf{r})\right]\hat{\Psi}(\mathbf{x}) + \frac{1}{2}\int d\mathbf{x}d\mathbf{x}'\hat{\Psi}^\dagger(\mathbf{x})\hat{\Psi}^\dagger(\mathbf{x}')V(\mathbf{x}\text{-}\mathbf{x}')\hat{\Psi}(\mathbf{x}')\hat{\Psi}(\mathbf{x}), \tag{1.20}$$

where $\hat{\Psi}(\mathbf{x})$ and $\hat{\Psi}^\dagger(\mathbf{x})$ are annihilation and creation operators of bosonic field and $V(\mathbf{x}\text{-}\mathbf{x}')$ is the interaction potential between atoms. The operator ∇^2 defined as $\nabla^2 \equiv \partial^2/\partial x^2 + \partial^2/\partial y^2 + \partial^2/\partial z^2$, $\mathbf{x}$ is four dimensional coordinate and defined as $\mathbf{x} = (\mathbf{r}, t)$. For large number of atoms N, Equation (1.20) is very time consuming to solve. Therefore, a *mean-field approach* is ofen used instead.

The main idea of the mean filed approach is decomposition of bosonic field operator into its mean value and fluctuations [6, 28, 47],

$$\hat{\Psi}(\mathbf{x}) = \psi(\mathbf{x}) + \hat{\Psi}'(\mathbf{x}) \tag{1.21}$$

where $\hat{\Psi}'(\mathbf{x})$ is fluctuation operator. This decomposition is called Bogoliubov approximation. The expectation value of the fluctuation operator, $\hat{\Psi}'(\mathbf{x})$, is zero and it is assumed to be very small. For pure condensate, it is assumed to be negligible. The mean value of bosonic operator, $\psi(\mathbf{x})$, is known as the "macroscopic" or "condensate" wavefunction. The macroscopic wavefunction is a classical field and acts as an order parameter for BEC transition.

By using the Heisenberg equation, we can derive the time evolution of the field operator [6], $\hat{\Psi}(\mathbf{x})$, namely

$$i\hbar\frac{\partial}{\partial t}\hat{\Psi}(\mathbf{x}) = [\hat{\Psi}(\mathbf{x}), \hat{H}] = \left[-\frac{\hbar^2}{2m}\nabla^2 + V_{\text{ext}}(\mathbf{r}) + \int d\mathbf{x}'\hat{\Psi}^\dagger(\mathbf{x}')V(\mathbf{x}\text{-}\mathbf{x}')\hat{\Psi}(\mathbf{x}')\right]\hat{\Psi}(\mathbf{x}). \tag{1.22}$$

To derive equation for the BEC wavefunction we use the effective interaction potential which we introduced in previous section and replace the field operator $\hat{\Psi}(\mathbf{x})$ with the condensate wavefunction, $\psi(\mathbf{x})$. Equation (1.22) then yields the closed equation for the condensate wavefunction [6, 28, 47],

$$i\hbar\frac{\partial}{\partial t}\psi(\mathbf{x}) = \left(-\frac{\hbar^2}{2m}\nabla^2 + V_{\text{ext}}(\mathbf{r}) + g|\psi(\mathbf{x})|^2\right)\psi(\mathbf{x}). \tag{1.23}$$

Equation (1.23) was independently derived by Gross and by Pitaevskii in early 1960s. Therefore, it was named after these two scientists, as the *Gross-Pitaevskii equation*.

The GPE describes the macroscopic coherent dynamics of BEC at absolute zero temperatures. However, one can state that absolute zero is unattainable in physics. From the description provided by thermodynamics, within a gas, all the particles behave in the same manner and in principle they can occupy certain quantum states. For a collection of bosons, and in the limit where the temperature goes to zero, all the particles are going to occupy the ground state of the system. Actually, before achieving this limit, an spectacular accumulation of particles in the ground state can be observed. Therefore, for a sufficiently low temperature, the majority of the particles are in the same quantum state, and have the same velocity. In this way, the collection of bosons behaves like a macroscopic fluid with new properties. In order to study these properties, it is only necessary to concentrate on the ground state. The state of the particles in a certain level is described by a normalised function, which is an eigenvector of the Hamiltonian associated to the physical situation under consideration, and whose eigenvalue corresponds to the energy of that level. Thus,we have to find the eigenvectors with minimum eigenvalue for the Hamiltonian that describes our system. This Hamiltonian includes all the interactions between every pair of particles. In other words, if there are N particles in the system, the Hamiltonian will have N^2 terms. If we consider the diluted gas, which is the case for the condensates obtained experimentally. In order to simplify the problem, we make use of the "mean-field" approach, which means that the action felt by a given particle due to the rest is substituted by the mean action of the fluid over the particle. This approximation is good if one can neglect the correlations in the gas, that is, if the gas is diluted, which is the case for the condensates obtained experimentally. In this way, one can changed a complex model for the interaction among bosons by a very simplified one that is valid for diluted gases.

In Chapter 2 and Chapter 3 we study properties of atomic BECs with a single macroscopically-occupied quantum state i.e., one-component BECs described by the GPE based on ideas which are given in this section. In one-component BECs spin degrees of freedom of the atoms are assumed to play no role. Therefore, dynamics of BEC can be described by single wavefunction.

1.4.1 The chemical potential and stationary solution

Bose-Einstein condensate appears when the ground state energy is equal to chemical potential, μ. Hence, μ is defined as the energy per particle for non-interacting BEC,

$$\mu = \frac{\langle H \rangle_N}{N}. \tag{1.24}$$

However, this definition of μ is no longer true for interacting BEC.

The Gross-Pitaevskii equation admits stationary solution in the form,

$$\psi(\mathbf{x}) = \Phi(\mathbf{r}) e^{-i\mu t/\hbar}. \tag{1.25}$$

Substituting solution (1.25) into the time-dependent Gross-Pitaevskii equation (GPE) (1.23), we derive the time-independent Gross-Pitaevskii equation,

$$\mu\Phi(\mathbf{r}) = \left(-\frac{\hbar^2}{2m}\nabla^2 + V_{\mathbf{ext}}(\mathbf{r}) + g|\Phi(\mathbf{r})|^2 \right) \Phi(\mathbf{r}). \tag{1.26}$$

From Equation (1.26) we find that [28],

$$\mu = \frac{\delta \langle H \rangle_N}{\delta N}, \tag{1.27}$$

which is the definition of a chemical potential for an interacting BEC.

1.4.2 Reduction of dimensionality

In this thesis, we use the GPE to model the nonlinear dynamics of BECs loaded into various two dimensional optical lattices and harmonic trap potentials. However, the true trapping potential is three dimensional. Under certain conditions, the dynamics of the 3D systems can be described using a model with reduced dimensionality. As an example, we will consider dimensionality reduction of 3D trapping geometry. The full 3D harmonic trapping potential can be written as,

$$V_{ext}(x, y, z) = \frac{1}{2}m(\omega_x^2 x^2 + \omega_y^2 y^2 + \omega_z^2 z^2), \tag{1.28}$$

where m is the atomic mass and $\omega_x, \omega_y, \omega_z$ are the characteristic trapping frequencies in x, y and z directions, respectfully. The characteristic harmonic oscillator lengths $a_i = (\hbar/m\omega_i)^{1/2}$ where $i\{x, y, z\}$, provide length scales for spatial size of the condensate. Let us assume that $\omega_r = \omega_x = \omega_y$ and $\omega_\perp = \omega_z$; then if $\Omega = \omega_r/\omega_\perp > 1$, the condensate is cigar-shaped, and if $\Omega < 1$ the condensate is disk-shaped [48].

The healing length is another important length scale which represents balance between the kinetic energy and interaction energy. If the BEC density grows from 0 to n over a distance ξ, then the two terms in the GPE representing the kinetic energy and the interaction energy are $\sim \hbar^2/(2m\xi^2)$ and $\sim 4\pi\hbar^2 a_s n/m$, respectfully. By equating these two energies, we get a value for the healing length [6],

$$\xi = (8\pi n a_s)^{-1/2}. \tag{1.29}$$

The dynamics of the BEC can be considered to be quasi-2D when the transverse confinement is tight enough, i.e. $a_z = (\hbar/m\omega_z)^{1/2}$ is smaller than ξ. This condition allows us to reduce 3D GPE (1.23) to a 2D GPE. Assuming a strong anisotropy of the trapping potential, the condensate wavefunction, $\psi(\mathbf{x})$ can be written in separable form $\psi(r, z; t) = \psi(r, t)\Phi(z)$, where $r^2 = x^2 + y^2$.

Before we proceed further with the dimensionality reduction, we convert 3D GPE (1.23) into a dimensionless form. This standard procedure allows us to study the system in a more general form. For this system we use characteristic units based on the trap parameters. These are the characteristic length $a_z = (\hbar/m\omega_z)^{1/2}$, energy $E = \hbar\omega_z$ and time $t = \omega_z^{-1}$. Then Equation (1.23) takes following form,

$$i\frac{\partial}{\partial t}\psi(r, z; t) = \left(-\frac{1}{2}\nabla^2 + V_{\text{ext}}(r, z) + g|\psi(r, z; t)|^2\right)\psi(r, z; t). \tag{1.30}$$

In these dimensionless units $g = 4/\sqrt{\pi}(a_s/a_z)(\omega_r/\omega_z)$. The dimensionless harmonic trap potential is given by,

$$V_{\text{ext}}(r, z) = \frac{1}{2}(\Omega^2 r^2 + z^2), \tag{1.31}$$

where $\Omega < 1$. We assume that all variable in Equation (1.30) and Equation (1.31) have been rescaled using characteristic units so that they are now dimensionless.

Because the system is quasi-two dimensional, we can assume that the transverse component of the BEC wavefunction, remains in the ground state, therefore we substitute the separable wavefunction, $\psi(r, z; t) = \psi(r, t)\Phi(z)$, into the dimensionless 3D GPE (1.30). The transverse wavefunction $\Phi(z)$ can be approximated by the ground state solution of a 1D harmonic oscillator with normalization, $\int_\infty^\infty |\Phi| dz = 1$. Then, by integrating Equation (1.31) over the transverse coordinate, we arrive at the dimensionless 2D GPE,

$$i\frac{\partial}{\partial t}\psi(r, t) = \left(-\frac{1}{2}\nabla^2 + V_{\text{ext}}(r) + g_{2D}|\psi(r, t)|^2\right)\psi(r, t), \tag{1.32}$$

where $g_{2D} = 1/\sqrt{2\pi}(a_s/a_z)(\omega_r/\omega_z)$ is rescaled for 2D and $\int |\psi(r, t)|^2 dxdy = N$, where N

is the norm and related to the number of atoms in the condensate, $\mathcal{N}$, as

$$\mathcal{N} = (1/\sqrt{2}\pi)(a_s\omega_r)/(a_z\omega_z)N. \tag{1.33}$$

1.5 Solitons

In this section we will consider special solutions of the nonlinear equations called solitons, as our works in this thesis are concentrated on studying these nonlinear modes. A soliton is a solitary wave that preserves its shape while it travels at a constant speed. This is possible because the effects of dispersion are compensated by the effects of nonlinearity.

The first recorded observation of the soliton phenomenon was made in 1834 by John Scott Russell who saw a solitary wave in Glasgow canal while riding his horse in the vicinity. Facinated by his observation, he studied this phenomenon both theoretically and experimentally, being able to recreate it in a wave tank. He named it the *wave of translation* [16]. However, the study of the "soliton" attracted the attention only in 1960s, starting fom the work by Zabusky and Kruskal [49]. While numerically studying the nonlinear disperseve Korteweg-de Vries (KdV) equation, derived from a continious approximation of the Fermi-Pasta-Ulam model, they came to the following conclusions: an initial profile representing a long-wavelength excitation would break up into a number of solitary waves, which would interact and pass through each other without losing their identity. In order to emphasize the particle-like behaviour of these waves, they named these states "solitons" [49]. The work on the KdV equation led to te examination of solitons in other integrable nonlinear dispersive equations, such as the sine-Gordon equation, which is a continuous version of the Frenkel-Kontorova model, and the nonlinear Schrödinger equation which describes the propagation of the light in nonlinear media [50–52]. This is particularly applicable to our work, as the Gross-Pitaevskii equation takes the form of a nonlinear Schrödinger equation.

It is important to note that the term "soliton" is commonly interchangeable with "solitary waves" to describe any localized nonlinear mode in a dispersive system. However, solitons have a precise mathematical description as exact solutions of integrable systems. Solitons in trapped BECs (such as a BEC loaded into an optical lattice considered in Chapter 2 of this thesis) are actually solitary waves, as a trapped condensate generally connot be modelled by an integrable system. Nevertheless, they still have many properties which are recognised as approximately those of true solitons.

Generaly, solitons are divided into two types-bright solitons, which are localized wavepackets and dark solitons which are density notches in a non-zero background with a characteristic phase gradient. An attractive interaction due to atomic scattering with negative scattering length in the condensate supports the formation of bright matter-wave solitons. A repulsive interaction in the condensate cause the formation of dark matter-wave solitons. The first bright BEC solitons were experimentally created by Khaykovich *et al.* [10] and Strecker *et.al* [11] with ^{7}Li atoms trapped in one-dimensional optical waveguides. A Feshbach resonance technique was used in order to tune the interactions between atoms from extremely repulsive (to create the condensate) to slightly attractive (to form the soliton). Another experiment by Cornish *et. al.* [53] demonstrated formation of bright solitons as a result of a BEC collapse [54].

In contrast to ^{7}Li, the most common atomic species used for BEC experiments, ^{87}Rb has repulsive interactions. This type of interaction usually only allows dark soliton states.

However, if the condensate is trapped in an optical lattice, the periodicity of the potential changes the dispersion properties of the condensate wavefunction, and enables formation of bright solitons [12].

1.6 Vortices

Solutions of two and three dimensional wave equations often have singularities. Mathematical quantities which describe physical properties of waves become infinite or change abruptly at the points of singularity [55]. For instance, if the phase of the wave possesses singularity, it is undefined at that point and wave intensity vanishes. Phase singularities are accepted as significant features to all waves. The earliest scientific description of phase singularity dates back to 1830s [55]. An English scientist, William Whewell studying the ocean tides, came to the striking conclusion. According to his studies, rotating tidal waves possess a singular point at which all cotidal lines meet and tide height disappears. Waves with a phase singularity and a rotational flow around singular point are called *vortices*. They can be observed in different physical systems, ranging from water whirlpools and tornadoes to quantized vortices in superfluids [56].

The Bose-Einstein condensate constitutes a well-researched example of a superfluid. Quantum vortices in BEC were first observed in 1999 [13], using two-component condensates. To form a vortex, a phase gradient was imprinted in one of the BEC components, which caused it to rotate. The system was stabilized at a configuration in which the non-rotating component was localized at the center of the trap acting as an effective potential on the rotating component, which resided in outer region. The extensive study of vortices in a BEC [13, 57–59] promises a better understanding of links between the physics of superfluidity and condensation.

In BEC theory, a vortex formation in the condensate can be described by the Gross-Pitaevskii equation (1.23). The GPE can generally be rewritten using *Madelung transformation*, $\Psi(\mathbf{r}) = |\Psi(\mathbf{r})|e^{iS(\mathbf{r})}$. Then the superfluid current can be defined as,

$$j(\mathbf{r}) = \frac{\hbar}{2im}[\Psi^*(\mathbf{r})\nabla\Psi(\mathbf{r}) - \Psi(\mathbf{r})\nabla\Psi^*(\mathbf{r})] = |\Psi(\mathbf{r})|^2\frac{\hbar}{m}\nabla S(\mathbf{r}) = \rho(\mathbf{r})\frac{\hbar}{m}\nabla S(\mathbf{r}). \quad (1.34)$$

The condensate velocity, $v(\mathbf{r}) = j(\mathbf{r})/\rho(\mathbf{r})$, is proportional to the gradient of a scalar function. Hence, the flow of the condensate is irrotational except at the points where the phase is singular, namely

$$\nabla \times v(\mathbf{r}) = \frac{\hbar}{m}\nabla \times \nabla S(\mathbf{r}). \quad (1.35)$$

This implies that the condensate can be rotated only through the formation of vortices such that the condensate density vanishes at the vortex core [60].

1.7 Collapse of BEC with attractive interaction

After the discovery of Bose-Einstein condensation of ultra cold atoms, the influence of interatomic interaction on the BEC properties has become one of the central questions. In this respect BEC experiments in ^{7}Li generate a special interest, since a weakly interacting gas ($\bar{n}|a_s|^3 \ll 1$) of ^{7}Li is characterized by attractive interaction ($a_s < 0$) between atoms [4, 6, 47]. Attractive interactions cause the BEC to increase its density in the centre of the trap in order to lower the interaction energy. The kinetic energy of the conden-

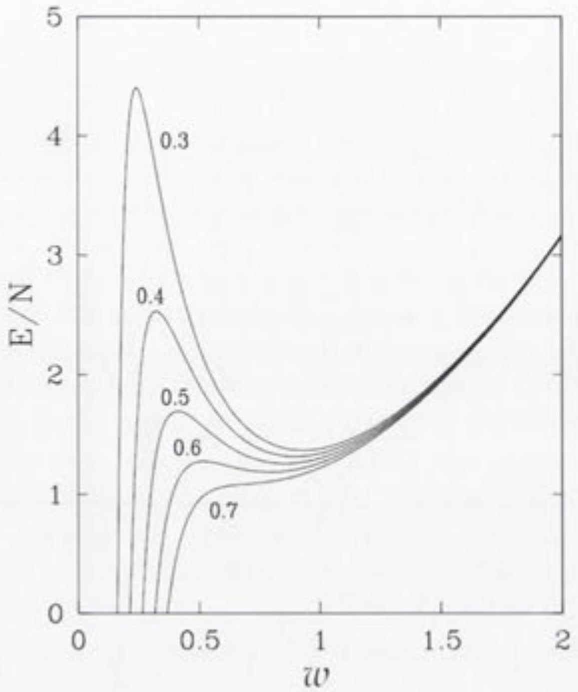

Figure 1.4: Energy per particle, in units of $\hbar\omega_{ho}$, for atoms with an attractive interaction in a spherical trap, as a function of the effective width w. Curves are plotted for several values of the parameter $N|a_s|/a_{ho}$. The local minimum disappears at $N = N_{cr}$. Figure is taken from [6].

sate counteracts the attraction and stabilizes the condensate for small enough attractive interactions. However, if the magnitude of the attractive interaction energy is increased, either by increasing the interaction strength or the density, the attractive interaction will eventually overwhelm the kinetic energy and make the condensate unstable against collapse. The collapse is expected to occur when the number of atoms in the BEC exceeds a critical value N_{cr}. The existence of stable state with attractive interactions is a remarkable feature produced by the trapping potential. We mention that in a uniform atomic gas, where quantum pressure is absent, the condensate is always unstable [6, 47].

A direct insight into the collapse behaviour of the BEC with attractive interaction can be obtained by means of the Gross-Pitaevskii equation (1.23) with harmonic trap potential (1.28). The critical number of atoms N_{cr} can be calculated by means of the GPE. The solutions of the GPE for $a_s < 0$ correspond to local minima of the energy functional [6],

$$E[\psi] = \int d\mathbf{x} \left[-\frac{\hbar^2}{2m} |\nabla\psi|^2 + V_{\text{ext}}(\mathbf{r})|\psi|^2 + \frac{g}{2}|\psi(\mathbf{x})|^4 \right]. \tag{1.36}$$

The first term in the integral (1.36) is the kinetic energy of the condensate E_{kin}, the second is the harmonic oscillator energy E_{ho}, while the last one is the mean-field interaction energy E_{int}. A first estimate can be obtained by calculating the interaction energy, $E_{int} = gN\bar{n}$, of the ground state of the harmonic oscillator, where the average density $\bar{n}$ is of the order N/a_{ho}^3, a_{ho} is the characteristic harmonic oscillator length given by $a_{ho} = (\hbar/m\omega_{ho})^{1/2}$, where ω_{ho} is the geometric average of the harmonic oscillator frequencies ω_x, ω_y and ω_z. Thus, $E_{int} \propto N^2|a_s|/a_{ho}^3$. The kinetic energy, E_{kin}, is proportional to Na_{ho}^{-2} [6]. Therefore,

$$\frac{E_{int}}{E_{kin}} \propto \frac{N|a_s|}{a_{ho}}. \tag{1.37}$$

When N increases, the depth of the local minima of the energy functional decreases. Above N_{cr} the minimum no longer exists and the GPE has no solution. For a spherical trap this happens at [61]

$$\frac{N_{cr}|a_s|}{a_{ho}} = 0.575. \tag{1.38}$$

This value is obtained by direct numerical solution of GPE in [61].

A physical insight into the condensate behaviour with attractive interactions can be obtained using variational approach based on Gaussian functions. The energy (1.36) in the spherical trap can be minimized using the following trial solution [6],

$$\psi(r) = \left(\frac{N}{w^3 a_{ho}^3 \pi^{3/2}}\right)^{1/2} \exp(-\frac{r^2}{2w^2 a_{ho}^2}), \tag{1.39}$$

where w is a dimensionless variational parameter which fixes the width of the condensate. Substituting (1.39) into (1.36), we can derive

$$\frac{E(w)}{N\hbar\omega_{ho}} = \frac{3}{4}(w^{-2} + w^2) - (2\pi)^{-1/2}\frac{N|a_s|}{a_{ho}} w^{-3}. \tag{1.40}$$

We see that the local minimum disappears when variational parameter, w exceeds a critical value in Figure 1.4. It can be calculated by requiring that the first and second derivatives of $E(w)$ vanish at the critical point ($w = w_{cr}$ and $N = N_{cr}$). Calculating critical values we find that $w_{cr} \approx 0.669$ and $N_{cr}|a_s|/a_{ho} \approx 0.671$ [6]. An estimate of critical number of atoms based on variational approach, reasonably close to the value given by (1.38).

The experimental measurements of trapped ^{7}Li BECs with attractive interaction [47, 62] are consistent with the theoretical predictions [63–67] for the maximum number of atoms that can be hosted in the condensate. Experiments on another BEC candidate with attractive interaction, ^{85}Rb [68], were carried out, where the value of the a_s was tuned by applying an additional magnetic field. These experiments have allowed the exploration of the dependence of the critical atom number on the value of the scattering length. The obtained results suggest that condensate collape occurs at a slightly lower value of the interaction strength than predicted by mean field theory.

One of the topics considered in this thesis is a mechanism of arresting collapse in BEC clouds with attractive interactions. In Chapter 3, we propose and analyze how to suppress collapse for 2D anisotropic BEC with orbital angular momentum using the mean filed theory.

1.8 Bose-Einstein condensate of exciton-polaritons

In 1962 excitons in semiconductors were proposed as a promising candidate for BEC in solid state systems [69], however subsequent research effort for 30 years did not show convincing evidence of exciton BEC. In 1992, control of semiconductor epitaxy allowed to create high-quality Fabry-Perot microcavities. Two-dimensional (2D) quantum well (QW) excitons in semiconductor planar Fabry-Perot microcavities showed the inhibited and enhanced spontaneous emissions [70, 71]. These emissions occur due to strong

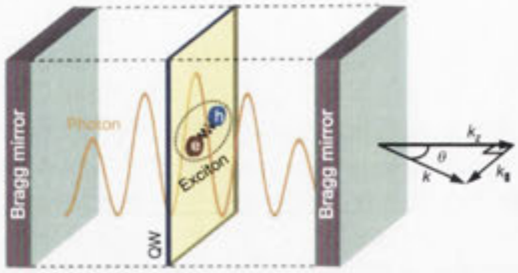

Figure 1.5: A microcavity is a planar Fabry - Perot resonator with two Bragg mirrors at resonance with excitons in quantum wells (QW). The exciton is an optically active dipole that results from the Coulomb interaction between an electron in the conduction band and a hole in the valence band. In microcavities operating in the strong coupling regime of the lightmatter interaction, 2D excitons and 2D optical modes give rise to new eigenmodes, called microcavity polaritons. [5]

dipole interactions or, in other words, coupling between QW excitons and cavity photon field resulting in new metastable eigenstates called microcavity polaritons (see Figure 1.5). Microcavity polaritons are neither exciton nor photon modes but mixture of both. Spontaneous emission results to split polariton mode dispersion into high energy and low energy branches.

In 1996 lower polaritons state at zero in plane momentum was suggested as new candidate for creating BEC in solids [72]. In 2006 exciton-polariton BEC in solid state system was announced [5]. Unlike bosonic atoms, exciton polaritons are bosonic quasiparticles and do not require temperatures close to absolute zero to realize the condensate due to their light mass. But polaritons in semiconductor microcavities are dissipative driven system. Dissipation of polaritons directly affects to superfluidity of exciton-polariton condensate [7, 73, 74].

1.8.1 Quantum-well exciton

One of the common approaches to describe atoms and their components in a solid, is to treat the stable ground state of an isolated system as a quasivacuum and to introduce quasiparticles as units of elementary excitations. The classic example of such a elementary excitation is an exciton in a semiconductor [75–78]. An exciton is a quasiparticle, consisting of an electron and a hole bound by the Coulomb interaction. A semiconductor can be considered as the quasivacuum, which is the state with valence band filled by electrons, and empty conduction band. It is possible for such a semiconductor to absorb a photon by transferring an electron, $-e$, from the valence band to the conduction band. The vacancy it leaves in the valence band can be described as a quasiparticle called a "hole." A hole in the valence band has opposite charge of electron, $+e$, and its effective mass defined by $(-\partial^2 E/\partial p^2)^{-1}$, where E and p denote the energy and momentum of the hole. A hole and an electron form a bound pair analogous to a hydrogen atom where an electron is bound to a proton. Nevertheless, due to a small effective-mass of the hole comparing to a mass of the electron and the strong dielectric screening in semiconductors, the binding energy of an exciton is on the order of $10 - 100$ meV and its Bohr radius, a_B, is about $10 - 100$ Å, extending over many atomic lattice spacings [75–78].

The exciton creation operator can be defined by creation operator of a conduction-band electron of momentum $\mathbf{k}$ as $\hat{a}^\dagger_{\mathbf{k}}$ and a valence-band hole as $\hat{b}^\dagger_{\mathbf{k}}$:

$$\hat{e}^\dagger_{\mathbf{K},n} = \sum_{\mathbf{k},\mathbf{k}'} \delta_{\mathbf{K},\mathbf{k}+\mathbf{k}'} \phi_n \left(\frac{m_h \mathbf{k} - m_e \mathbf{k}'}{m_e - m_h} \right) \hat{a}^\dagger_{\mathbf{k}} \hat{b}^\dagger_{\mathbf{k}'}, \tag{1.41}$$

where m_e and m_h are the electron and hole mass, respectively; $\mathbf{K}$ is the center-of-mass momentum of the exciton; $\phi_n(\mathbf{k})$ is the wave function of the relative motion of an electron and a hole; and n is the quantum number of the relative motion. The commutation relations for the exciton operators take the form [77, 78],

$$\begin{aligned} &[\hat{e}_{\mathbf{K},n}, \hat{e}_{\mathbf{K},n}] = 0, \\ &[\hat{e}^\dagger_{\mathbf{K},n}, \hat{e}^\dagger_{\mathbf{K},n}] = 0, \\ &[\hat{e}_{\mathbf{K},n}, \hat{e}^\dagger_{\mathbf{K},n}] = \delta_{\mathbf{K},\mathbf{K}'} \delta_{n,n'} - O(n_{exc} a_B^3). \end{aligned} \tag{1.42}$$

Excitons can be considered as bosons when the exciton interparticle spacing is much larger than its Bohr radius: $n_{exc}^{-1/3} \gg a_B$.

The electron and hole bound state form a dipole that interacts with electromagnetic fields of photon. The interaction strength between photon with angular frequency ω and an exciton can be conditionally described in terms of the exciton oscillator strength f,

$$f = \frac{2m^*\omega}{\hbar} |\langle u_h | \mathbf{r} \cdot \mathbf{e} | u_e \rangle|^2 \frac{V}{\pi a_B^3}, \tag{1.43}$$

where $m^* = m_e m_h / (m_e + m_h)$ is the effective mass of the exciton, $|u_e\rangle$ and $|u_h\rangle$ are Bloch functions of the electron and hole respectively, V is the exciton quantization volume. $V/\pi a_B^3$ denotes the interaction enhancement due to enhanced electron-hole overlap in an exciton compared to a pair of unbound electron and hole [77, 78].

Nowadays the advances of the crystal growth create possibility to realize low-dimensional semiconductor structures, where an exciton is confined in one or two dimensions. Hence, it is interesting to understand the exciton bound state in reduced dimensions, and to explore how the exciton properties change due to the quantum confinement. In this section we address to the two-dimensional case, i.e. the case of quantum well excitons.

A semiconductor quantum well can be modeled as a thin layer of semiconductor with a thickness comparable to the exciton Bohr radius, sandwiched in a large gap semiconductor. In such a geometry, the center-of-mass motion of an exciton in a QW is quantized along the confinement direction. In this case if only one quantized level is concerned, in most cases the lowest-energy level, QW excitons are treated as two-dimensional quasi-particles [78].

Due to the quantum confinement, the valence-band structure and the optical transition strength are also modified. Most significantly, the total wave vector k is no more conserved in these structures, while the only conserved quantity is the in-plane component of the wave vector $k_\parallel$. Thus, excitons in a QW couple to light with the same in-plane wave number $k_\parallel$.

Moreover, the quantum confinement leads to a smaller Bohr radius and larger binding energy of a QW exciton, modifying the oscillator strength enhancement as $(a_B^{3D}/a_B^{2D})^3$. Therefore, the transverse coherence length of the photon field becomes much longer than

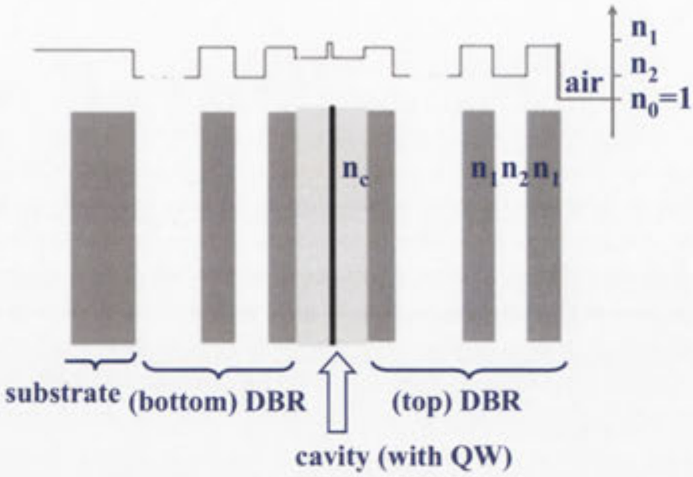

Figure 1.6: Model of a semiconductor $\lambda/2$ microcavity. [78]

the QW thickness and the overlap between photon field and an exciton will be reduced. In order to achieve stronger exciton-photon coupling, the photon field should also be confined by introducing a microcavity [77, 78].

1.8.2 Quantum-well microcavity polariton

A typical structure of a semiconductor microcavity consists of a $\lambda_c/2$ cavity layer sandwiched between two distributed Bragg reflectors (DBRs), see Figure 1.6. Semiconductor layers in DBRs are located with alternating high and low refraction indices. The optical thickness of a single semiconductor layer is equal to $\lambda/4$. The reflected light from each interface destructively interfere and create a stop-band for transmission. Therefore, DBRs can be considered as mirrors with high-reflectance, when the incident light wavelength is within the stop band [78–80].

The light field penetration depth into the DBRs is much larger in comparision with a metallic cavity. The effective cavity length is extended in a semiconductor microcavity as,

$$L_{\text{eff}} = L_c + L_{DBR} \tag{1.44}$$

$$L_{DBR} \approx \frac{\lambda_c}{2n_c}\frac{n_1 n_2}{|n_1 - n_2|}. \tag{1.45}$$

Here n_1 and n_2 are refraction indices of the DBR layers [78, 79].

In the planar DBR cavity the photon field will be confined only in the z direction. The incident light from a tilt angle θ relative to the z axis has a resonance at $\lambda_c/\cos\theta$. Thus, an energy dispersion versus the in-plane wave number $k_\parallel$ in the the cavity takes the form,

$$E_{cav} = \frac{\hbar c}{n_c}\sqrt{k_\perp^2 + k_\parallel^2}, \tag{1.46}$$

where $k_\perp = n_c(2\pi/\lambda_c)$. And there is a one-to-one correspondence between the incidence angle θ and each resonance mode with in-plane wave number $k_\parallel$

$$k_\parallel = \frac{2\pi}{\lambda_c}\theta \quad \text{when} \quad \mathrm{k}_\parallel \ll \mathrm{k}_\perp. \tag{1.47}$$

In the region $k_\parallel \ll k_\perp$, tne energy dispersion can be derived as,

$$E_{cav} \approx \frac{\hbar c}{k_\perp}\left(1+\frac{k_\parallel^2}{2k_\perp^2}\right) = E_{cav}(k_\parallel = 0) + \frac{\hbar^2 k_\parallel^2}{2m_{cav}}. \tag{1.48}$$

Here the cavity photon effective mass is

$$m_{cav} = \frac{E_{cav}(k_\parallel = 0)}{c^2/n_c^2}, \tag{1.49}$$

and has the order of $10^{-5}m_e$ [79, 80].

When the QWs are placed at the antinodes of the resonant field of a semiconductor microcavity, the QWs exciton strongly interacts with the confined optical field of the cavity. If the energy exchange rate between the cavity photons and excitons becomes much faster than the decay and decoherence rates of both the cavity photons and the excitons, an excitation in the system is no longer excitons or photons but a new type of quasiparticles called the polaritons [5, 78, 79].

The linear Hamiltonian of the system can be written in the second quantization form as,

$$\begin{aligned}\hat{H}_{pol} &= \hat{H}_{cav} + \hat{H}_{ext} + \hat{H}_{int} \\ &= \sum E_{cav}(k_\parallel, k_c)\hat{a}^\dagger_{\mathbf{k}_\parallel}\hat{a}_{\mathbf{k}_\parallel} + \sum E_{ext}(k_\parallel)\hat{b}^\dagger_{\mathbf{k}_\parallel}\hat{b}_{\mathbf{k}_\parallel} + \sum g_0(\hat{a}^\dagger_{\mathbf{k}_\parallel}\hat{b}_{\mathbf{k}_\parallel} + \hat{b}^\dagger_{\mathbf{k}_\parallel}\hat{a}_{\mathbf{k}_\parallel})\end{aligned} \tag{1.50}$$

Here $\hat{a}^\dagger_{\mathbf{k}_\parallel}$ is the photon creation operator with an inplane wave number $k_\parallel$ and longitudinal wave number $k_c = \mathbf{k}\hat{z}$ determined by the cavity resonance. $\hat{b}_{\mathbf{k}_\parallel}$ is the exciton creation operators with an in-plane wave number $k_\parallel$. g_0 is the exciton-photon interaction strength; it is nonzero only between modes with the same $k_\parallel$. The above Hamiltonian can be diagonalized by the transformations [78, 79],

$$\begin{aligned}\hat{P}_{\mathbf{k}_\parallel} &= X_{k_\parallel}\hat{b}_{\mathbf{k}_\parallel} + C_{k_\parallel}\hat{a}_{\mathbf{k}_\parallel}, \\ \hat{Q}_{\mathbf{k}_\parallel} &= -C_{k_\parallel}\hat{b}_{\mathbf{k}_\parallel} + X_{k_\parallel}\hat{a}_{\mathbf{k}_\parallel},\end{aligned} \tag{1.51}$$

Then $\hat{H}_{pol}$ becomes

$$\hat{H}_{pol} = \sum E_{LP}(k_\parallel)\hat{P}^\dagger_{\mathbf{k}_\parallel}\hat{P}_{\mathbf{k}_\parallel} + \sum E_{UP}(k_\parallel)\hat{Q}^\dagger_{\mathbf{k}_\parallel}\hat{Q}_{\mathbf{k}_\parallel}, \tag{1.52}$$

where $(\hat{P}^\dagger_{\mathbf{k}_\parallel}, \hat{P}_{\mathbf{k}_\parallel})$ and $(\hat{Q}^\dagger_{\mathbf{k}_\parallel}, \hat{Q}_{\mathbf{k}_\parallel})$ are the creation and annihilation operators of the new quasiparticles or eigenmodes of the system. They are called the lower polariton (LP) and upper polariton (UP), corresponding to the two branches of lower and higher eigenenergies, respectively. Thus a polariton is a linear superposition of an exciton and a photon with the same in-plane wave number $k_\parallel$. Since both excitons and photons are bosons, so are the polaritons. The exciton and photon fractions in each LP and UP are given by the amplitude squared of $X_{k_\parallel}$ and $C_{k_\parallel}$ which are referred to as the Hopfield coeffi-

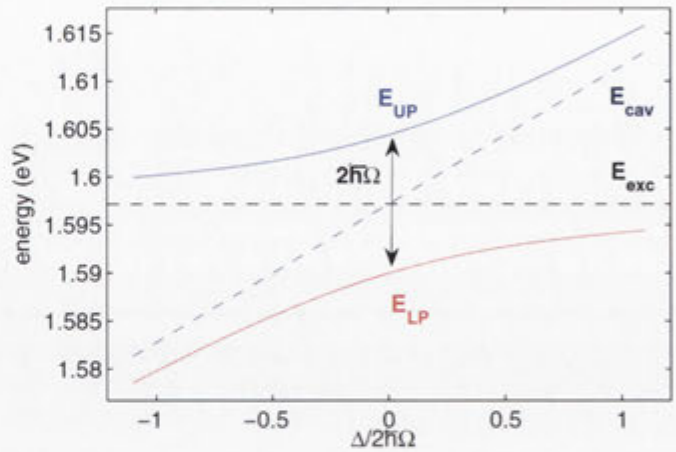

Figure 1.7: Anticrossing of LP and UP energy levels when tuning the cavity energy across the exciton energy [78].

cients [78, 79, 81]. They satisfy,

$$|X_{k_\parallel}|^2 + |C_{k_\parallel}|^2 = 1. \tag{1.53}$$

If we define $\Delta E(k_\parallel) = E_{ext}(k_\parallel) - E_{cav}(k_\parallel, k_c)$; $X_{k_\parallel}$ and $C_{k_\parallel}$ are given by,

$$\begin{aligned} |X_{k_\parallel}|^2 &= \frac{1}{2}\left(1 + \frac{\Delta E(k_\parallel)}{\sqrt{\Delta E^2(k_\parallel) + 4g_0^2}}\right), \\ |C_{k_\parallel}|^2 &= \frac{1}{2}\left(1 - \frac{\Delta E(k_\parallel)}{\sqrt{\Delta E^2(k_\parallel) + 4g_0^2}}\right) \end{aligned} \tag{1.54}$$

At $\Delta E = 0$, $|X|^2 = |C|^2 = \frac{1}{2}$, LP and UP are exactly half photon half exciton [78, 81]. The polariton energies, which are the eigenenergies of the Hamiltonian, can be deduced from the diagonalization procedure as

$$E_{\mathrm{LP,UP}}(k_\parallel) = \frac{1}{2}[E_{exc} - E_{cav} \pm \sqrt{4g_0^2 + (E_{ext} - E_{cav})^2}] \tag{1.55}$$

When the uncoupled exciton and photon are at resonance, $E_{exc} = E_{cav}$, LP and UP energies have the minimum separation, $E_{UP} - E_{LP} = 2g_0$, which is often called the normal-mode splitting in analogy to the Rabi splitting of a single-atom cavity system. Due to the coupling between the exciton and photon modes, the new polariton energies anticross when the cavity energy is tuned across the exciton energy. This is one of the signatures of "strong coupling". When $E_{cav} - E_{exc} \gg g_0$, polaritons quickly become indistinguishable from a photon or exciton. Unless otherwise specified, the detuning is assumed to be comparable to or less than the coupling strength [78].

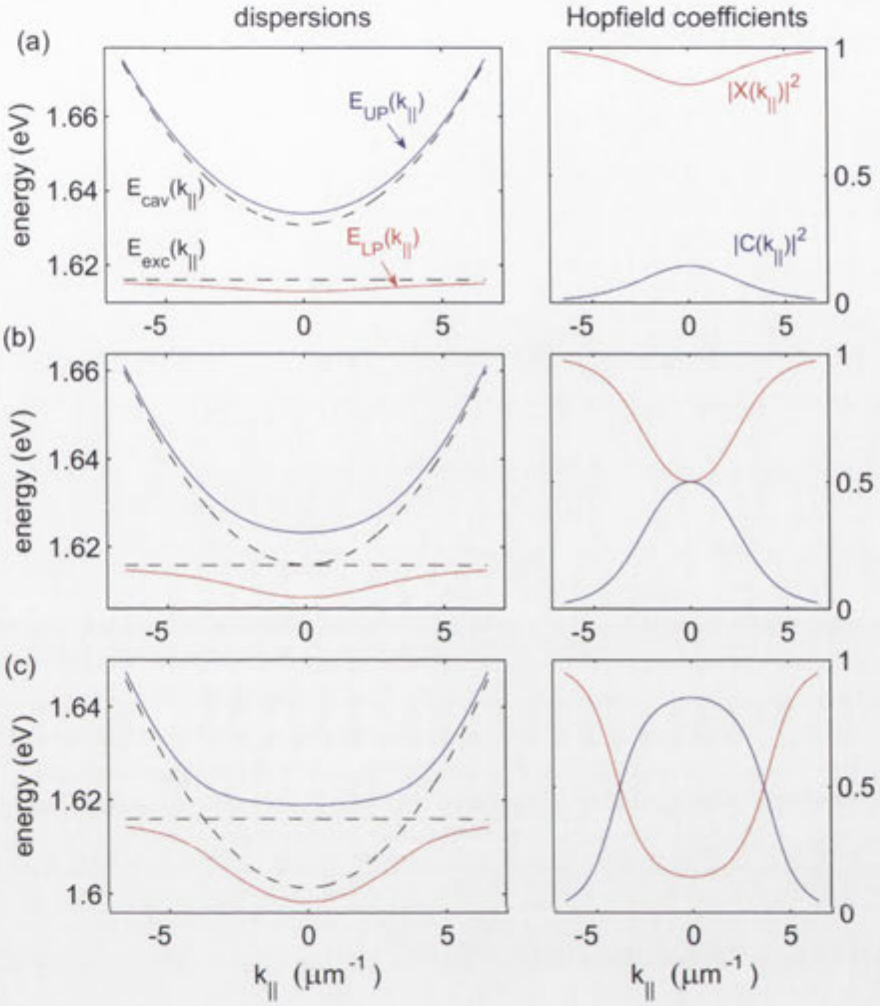

Figure 1.8: Polariton dispersions and corresponding Hopfield coefficients at (a) $\Delta = 2g_0$, (b) $\Delta = 0$, and (c) $\Delta = -2g_0$ [78].

1.8.3 Polariton dispersion and effective mass

If we definene Δ_0 as difference between the exciton and photon energy at $k_{\|} = 0$,

$$\Delta_0 = E_{ext}(k_{\|} = 0) - E_{cav}(k_{\|} = 0), \tag{1.56}$$

for given Δ_0, we will have the polariton energy momentum dispersions. In the region $\hbar^2 k_{\|}^2/2m_{cav} \ll 2g_0$, the dispersions have parabolic shape,

$$E_{\mathrm{LP,UP}}(k_{\|}) \simeq E_{\mathrm{LP,UP}}(0) + \frac{\hbar^2 k_{\|}^2}{m_{\mathrm{LP,UP}}}. \tag{1.57}$$

The polariton effective mass is the defined by harmonic mean of the exciton and photon component masses,

$$\frac{1}{m_{LP}} = \frac{|X|^2}{m_{exc}} + \frac{|C|^2}{m_{cav}},$$
$$\frac{1}{m_{UP}} = \frac{|C|^2}{m_{exc}} + \frac{|X|^2}{m_{cav}}, \tag{1.58}$$

where m_{exc} is the effective exciton mass of its centerof-mass motion and m_{cav} is the effective cavity-photon mass [78]. Since $m_{cav} \ll m_{exc}$, we will have

$$m_{LP}(k_{\parallel} \sim 0) \simeq m_{cav}/|C|^2 \sim 10^{-4} m_{exc},$$
$$m_{UP}(k_{\parallel} \sim 0) \simeq m_{exc}/|X|^2. \tag{1.59}$$

The very small effective mass of LPs at $k_{\parallel} \sim 0$ makes possible the phase transitions at the very high critical temperature. At large $k_{\parallel}$ where $E_{cav}(k_{\parallel}) - E_{ext}(k_{\parallel}) \ll g_0$, dispersions of the LP and UP converge to the exciton and photon dispersions. Then LP has an effective mass $m_{LP} \sim m_{exc}$. Hence, the effective mass of LPs changes by four orders of magnitude from $k_{\parallel} \sim 0$ to large $k_{\parallel}$. The shape of dispersions has important implications in the energy relaxation dynamics of polaritons. Figure 1.8 shows a few examples of the polariton dispersion with different Δ_0.

1.9 Schemes of excitations

With the improvement of fabrication techniques and optimization of the experimental conditions, quantum degeneracy and lasing at the $k_{\parallel} = 0$ LP ground state have been observed first with GaAs-based devices [82] and later with CdTe-based devices [5] and GaN-based devices [83].

In its ground state, the semiconductor microcavity is empty. Polaritons can be injected by means of optical or electrical injection. The polariton life time is mainly limited by the finite photon life time. In state of the art microcavities, it is around 10 ps, which is of the order of the other time scales of their dynamics and thus presents a severe limitation [5]. Therefore, polaritons are often continuously injected in order to compensate for these losses. Two different optical injection schemes should be distinguished. The first excitation scheme is $resonant$ excitation (see Figure 1.9 (a)): A laser is tuned to the polariton frequency at a given wave vector. The second scheme is $non-resonant$ excitation (see Figure 1.9 (c)). In this latter case, the laser is tuned to an energy above the polariton energy. High energy excitons or free electron-hole pairs are formed, that subsequently relax to the bottom of the lower polariton branch. Electrical excitation has a similar effect [84].

An important difference between the resonant and non-resonant excitation schemes concerns the phase symmetry of the polariton field. In the case of resonant excitation, the coupling of the external laser amplitude to the microcavity explicitly breaks the phase symmetry. The phase of the polariton field is determined by the phase of the laser and in particular its spatial and temporal coherence is determined by the coherence properties of the laser light. Under non-resonant excitation on the other hand, the phase symmetry

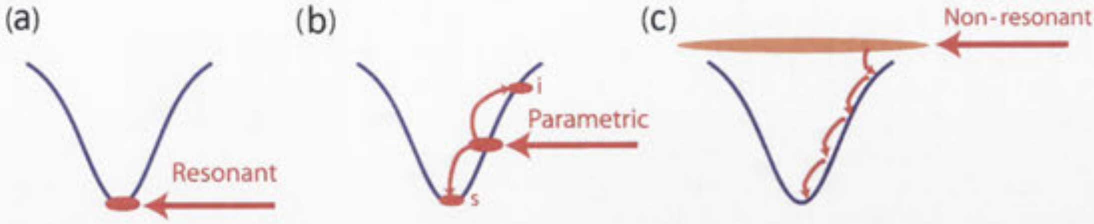

Figure 1.9: Comparison of the different excitation schemes: (a) resonant, (b) parametric and (c) non-resonant [84].

is not explicitly broken and polariton coherence can spontaneously form [84].

An excitation scheme that is intermediate between resonant and non-resonant excitation is the so-called parametric excitation [85, 86]. The lower polariton branch is excited resonantly at an energy above the ground state carefully chosen so that polaritons can scatter into the ground state (signal) and an excited state (idler) through a single collision. The parametric scheme is illustrated in Figure 1.9 (b). Where under parametric excitation, the phase of the pumped mode is fixed by the laser, the signal phase is chosen spontaneously, because only the sum of signal and idler phases is fixed $\phi_s + \phi_i = 2\phi_p$. Therefore, the spontaneous formation of coherence is observed when the density of polaritons in the signal mode is increased [84].

Finally, under pulsed resonant excitation, the polariton phase is only fixed as long as the laser pulse excites the microcavity and is free to evolve afterwards. The main limitation of this scheme is, as we mentioned earlier, the finite polariton life time that makes the density drop on the same time scale as the other time scales that are involved in the dynamics [84].

When the laser pulse duration is sufficiently long in comparison with the characteristic time such as polariton life time, the system is considered under continuous-wave pumping which guarantees a steady-state of the condensate. The excitation energy well above the polariton ground state, ensures that polaritons initially injected in the system are incoherent, which is a necessary condition for demonstrating BEC. In Chapter 3 and 4, we study formation and properties of a steady-state polariton condensate based on continuous-wave non-resonant excitation scheme.

1.10 Trapping techniques of exciton polariton condensates

Most of the experiments performed with exciton polariton BEC used planar microcavities without an intentional in-plane trapping potential. The size of the system is largely determined by the spot size of the pump laser [5, 80]. In comparison, a trapped polariton system may offer several advantages [82, 87–89]. With a trapping potential, genuine BEC becomes possible in two dimensions, and spatial condensation accompanies the configuration-space condensation. A strong trapping potential may lead to discrete polariton modes, hence single-mode BEC. Signatures of BEC should be more pronounced in all these cases. The trap can also serve as a tuning knob for the system. With a lattice potential, coherence and interactions among multiple condensates can be studied [78]. In this section, we shortly review the efforts to implement single and lattice potentials for polaritons.

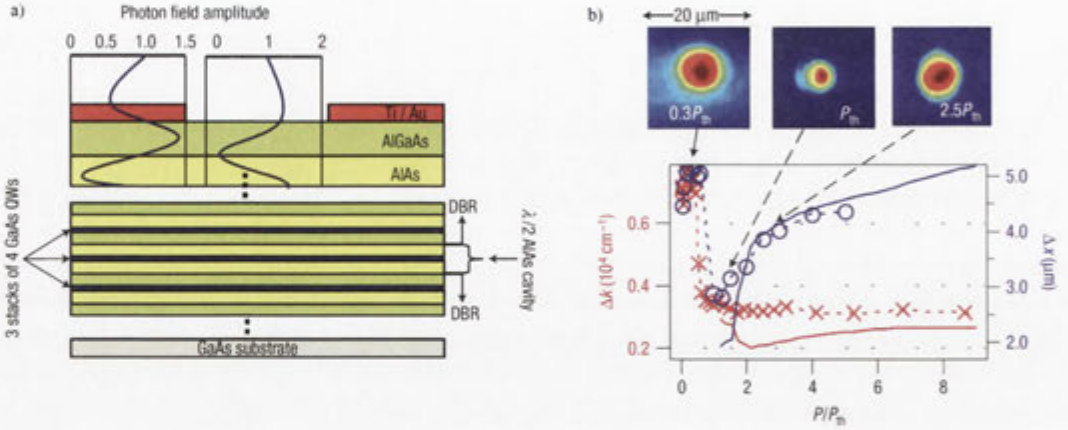

Figure 1.10: Polariton condensation in an optical trap by metal masks. (a) A schematic of a polariton trap. (b) The measured standard deviations of LP distribution in coordinate Δx (circles) and in wave number Δk (crosses) are plotted as a function of P/P_{th}. Theoretical values for Δx and Δk obtained by the GPE are shown by the solid lines [88].

1.10.1 Single potentials for polaritons

A single isolated trap for polaritons is implemented by modifying either the cavity photon or the QW exciton energies.

Optical traps by metal mask.
A rather versatile type of polariton trap is based on modulating the cavity layer thickness and transmission with a thin metal mask deposited on the surface of the microcavity. As shown in Figure 1.10 (a), a trap potential of $\sim 200\ \mu$eV is provided by a hole surrounded by a thin metal Ti/Au film [87, 88]. The cavity resonant field has normally an antinode at the AlGaAs-air interface. However, the antinode position is shifted inside the AlGaAs layer with the metal film as shown in Figure 1.10 (a), which results in the blueshift of the cavity photon and subsequently LP resonances. The LPs were confined in circular holes of varying diameters from 5 to 100 μm. In a trap with 5-10 μm diameter, a single fundamental transverse mode dominates the condensation dynamics over higher-order transverse modes due to the relatively weak confining potential. A weak confining potential helps to cool polaritons efficiently because high-energy polaritons created by two-body scattering are quickly expelled from the trap region [78, 88].

The top panels in Figure 1.10 (b) show the near-field emission patterns from a trap with 8 μm diameter at pump rates below, just above, and well above condensation threshold. The measured standard deviations for the LP position Δx and wave number Δk are plotted as a function of P/P_{th} in Figure 1.10 (b). The sudden decreases in Δx and Δk were clearly observed at threshold P/P_{th}. Just above threshold, the measured uncertainty product $\Delta x \Delta k$ is ~ 0.98, which is compared to the Heisenberg limit $\Delta x \Delta k \sim 0.5$ for a minimum uncertainty wave packet. Here 10^{-3} LPs condense into a nearly minimum uncertainty wave packet at threshold. The monotonic increase in Δx and $\Delta x \Delta k$ at higher pump rates stems from the repulsive interaction among LPs in a condensate and is well reproduced by the numerical analysis using the spatially inhomogeneous GP equation as shown by solid lines in Figure 1.10 (b) [88].

Optical traps by fabrication.

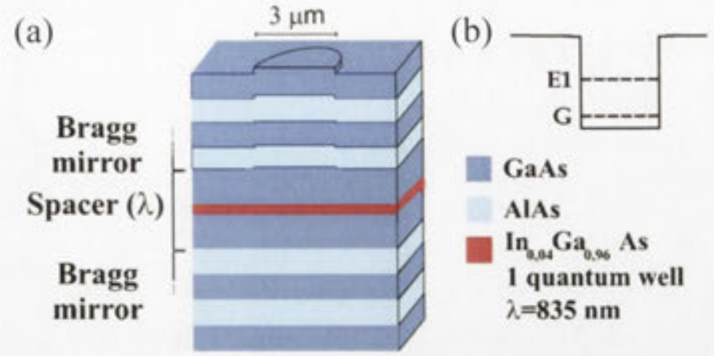

Figure 1.11: (a) Scheme of a fabricated microcavitiy with circular mesas etched on the spacer layer. Only the first four layers of the Bragg mirrors are represented. (b) Scheme of a potential trap with two confined levels: the ground level (G) and one excited state (E1) [90].

Strong optical confinement, hence discrete polariton modes, has been realized by modifying the microcavity structure. Earlier efforts focused on etching small pillar structures out of a planar microcavity to achieve strong transverse confinement of the photon modes. In pillars of a few microns across, discrete polariton modes and polariton parametric scattering were observed. In very small pillars, leakage of the cavity-photon fields and loss of excitons at the side walls prevent strong coupling.

Alternatively, in a similar spirit as the metal masks, it was devised a way to grow small regions with thicker cavity layers and lower photon (and thus polariton) energies, as shown Figure 1.11 [90]. Compared to using metal masks, the energy difference between inside and outside the trap region is large enough to discretize the polariton modes. Compared to the etching method, the QW excitons are untouched and will not suffer surface recombination; transport and interactions are possible between untrapped and trapped polaritons. Discrete polariton spectra were observed in such a structure, in agreement with calculations [78].

Exciton traps by mechanical stress.
A polariton trap with a relatively larger area has been formed by mechanically pressing a planar microcavity wafer [82]. A force is applied on the backside of the 150-μm-thick substrate with a rounded-tip pin, with approximately 50 μm tip radius, as shown in Figure 1.12. This pushes the exciton energy down toward the cavity mode, at the same time creating a harmonic potential. The harmonic potential is centered in the plane at the point of pin-sample contact [82].

1.10.2 Lattice potentials for polaritons

Extending a single trap potential to a lattice potential, the long-range spatial coherence leads to the existence of phase-locked multiple condensates, such as in an array of superfluid helium, superconducting Josephson junctions and atomic BECs. Under certain circumstances, a quantum phase difference of π is predicted to develop among weakly coupled Josephson junctions. Such a metastable π state was discovered in a weak link of superfluid ^3He, which is characterized by a p-wave order parameter. Possible existence of such a π state in weakly coupled atomic BECs has also been proposed but remains

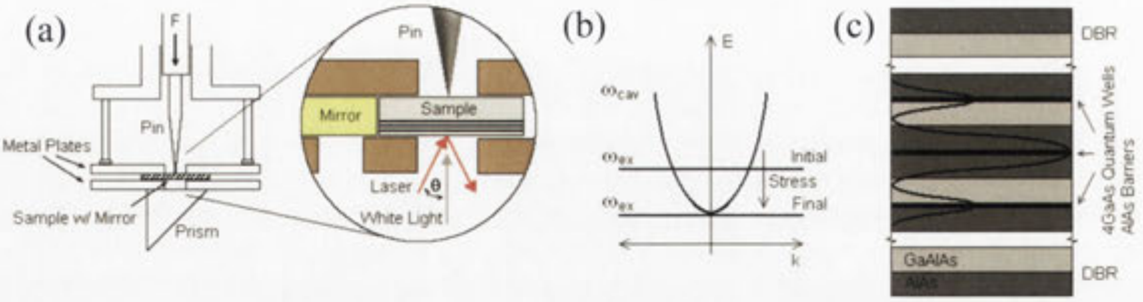

Figure 1.12: (a) Geometry of the experiment. (b) The effect of stress tuning. (c) The structure of the microcavity [82].

undiscovered in atomic systems. Recently it is observed spontaneous buildup of in-phase (zero-state) and antiphase (π-state) coherent states in a polariton condensate array connected by weak periodic potential barriers. These states reflect the band structure of the one-dimensional periodic potential for polaritons and feature the dynamical competition between metastable and stable polariton condensates [78].

One-dimensional periodic array of polaritons.
Employing the same metal deposition technique, an array of one-dimensional cigar-shaped polaritons is created by the deposition of periodic strips of a metallic thin film on the top surface of a microcavity structure, as shown in Figure 1.13 (a). Under the metallic layer, the cavity resonance energy is expected to increase. When the cavity photon (E_{cav}) is near resonance with the QW exciton (E_{exc}) at $k_{\parallel} = 0$, the shift of the LP energy induced by the metallic layer is $\sim 200\mu$eV, approximately one half of the cavity-photon resonance shift (see Figure 1.13 (b)). Therefore, the LPs are expected to be trapped in the gap region where the LP energy is lower. The measured spatial modulation of LP energy is $\sim 100\mu$eV, which is less than the theoretical prediction due to the diffraction limited spatial resolution ($\sim 2\mu$m) of the optical detection system, as shown in Figure 1.13 (c) [78, 87].

The microcavity is excited by a mode-locked Ti:sapphire laser with an $\sim 2.5\ ps$ pulse near the QW exciton resonance at an incident angle of 60°, corresponding to an in-plane wave number $k_{\parallel} \approx 7\times10^4\ cm^{-1}$ in air. The large $k_{\parallel}$ of the pump assures that the coherence of the pump laser is lost by multiple phonon emissions before the LPs scatter into $k_{\parallel} \approx 0$ states.

Considering a periodic and coherent array of condensates aligned along the x axis, the order parameter can be approximated in momentum space as [78, 87]

$$\psi(k_x) = \psi_0(k_x) \sum_{n=0,\pm1,\dots,\pm n_M} e^{in(k_x a+\phi)} = \psi_0(k_x)\frac{\sin[Nk_x a/2]}{\sin[k_x a/2]} \quad (\text{if} \quad \phi = 0), \tag{1.60}$$

where n labels the condensate array element, $N = 2n_M + 1$ is the total number of periodic array elements, a is the pitch distance between two neighboring elements, and $\psi_0(k_x)$ is the momentum-space wave function of an individual element. The overall momentum distribution $\rho(k_x) = |\psi(k_x)|^2$ reflects the coherence properties and nature of the condensate arrays through distinctive interference patterns. In the presence of the periodic lattice, the momentum distribution displays narrow peaks at $k_x = m \times 2\pi/a$ ($m \in$ integer) with an envelope function given by $|\psi(k_x)|^2$. If all the elements are locked in phase ($\phi = 0$), at a LP wavelength $\lambda = 780\ nm$ and a grating pitch distance $a = 2.8$

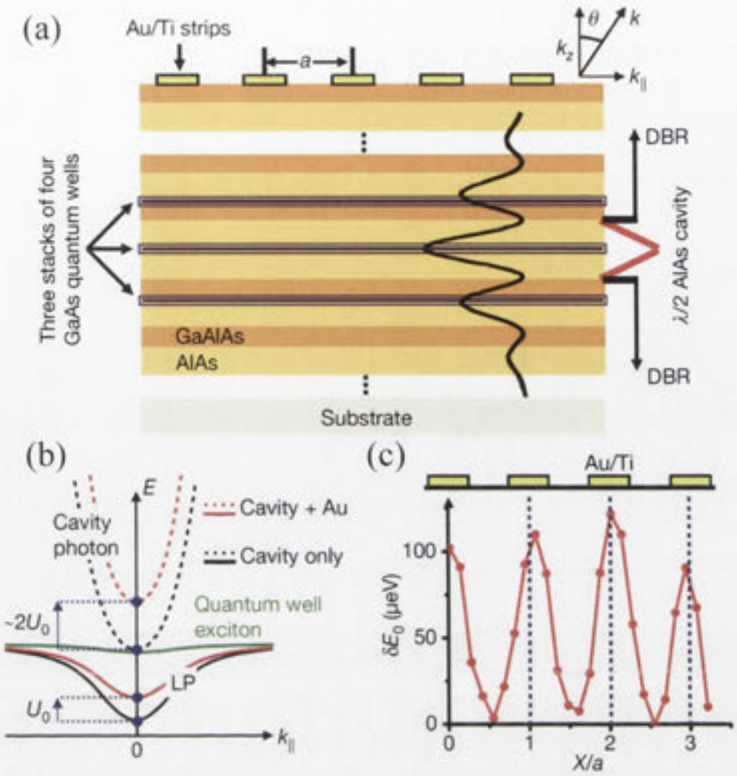

Figure 1.13: Formation of a polariton array. (a) A schematic of a polariton array formed by depositing periodic thin metallic strips (Au/Ti) on top of a microcavity structure. (b) Dispersion curves of the cavity-photon mode and LP. (c) Spatial LP energy modulation is detected from the position dependent central energy of LP emissions [87].

μm, a Fraunhofer diffraction pattern has a central peak at $\theta = 0°$ and two side lobes at $\theta = \sin^{-1} \lambda/a \approx \pm 16°$ ($k_\parallel = 2\pi/a$, $m = \pm 1$ first-order diffraction) [87]. The LP emissions from a polariton condensate array are expected to display such an interference pattern in momentum space, just like in an atomic BEC experiment [23, 91].

1.11 Open dissipative Gross-Pitaevskii equation

In a Bose-Einstein condensation experiment, bosons are usually trapped in a confining potential in order to maintain a required critical density and some sort of cooling mechanism is implemented in order to realize a required critical temperature. A particle trap has a finite lifetime of the order of a second for atomic BEC and a picosecond to nanosecond for exciton-polariton BEC. A cooling mechanism also accompanies a particle loss process, such as evaporation of atoms or photon emission of exciton-polaritons. Thus a phenomenon of BEC must be experimentally probed during a time window between the condensate formation and the condensate decay. If this time window is very wide, the BEC is indistinguishable from a thermal equilibrium phenomenon of a closed system. On the other hand, if this time window is very short, the condensation phenomenon is necessarily dynamical and should be considered as the property of an open dissipative system. The former is true for most atomic BEC experiments and the latter applies to exciton-polariton BEC experiments.

A standard Gross-Pitaevskii equation is not adequate for describing the second case. Instead, such a system is treated by an open dissipative Gross-Pitaevskii equation, which is a coupled equation for the condensate wavefunction $\Psi(\vec{r},t)$ and the reservoir population $n_R(\vec{r},t)$ [7, 78]:

$$i\hbar\frac{\partial\Psi(\vec{r},t)}{\partial t} = \left[-\frac{\hbar^2}{2m}\nabla_\perp^2 + V_{ext}(\vec{r},t) - i\frac{\hbar}{2}(\gamma_c - Rn_R(\vec{r},t))\right]\Psi(\vec{r},t)$$

$$+ \left[g_c|\Psi(\vec{r},t)|^2 + g_R n_R(\vec{r},t)\right]\Psi(\vec{r},t), \tag{1.61}$$

$$\frac{\partial n_R(\vec{r},t)}{\partial t} = -(\gamma_R + R|\Psi|^2)n_R(\vec{r},t) + P(\vec{r},t)$$

In Equation (1.61), $V_{ext}(\vec{r},t)$ is an external trap potential, γ_c is the condensate particle loss rate, $Rn_R(\vec{r},t)$ is the gain rate for the condensate due to bosonic final state stimulation, and g_c and g_R are the condensate-condensate and condensate-reservoir repulsive interactions ($g_c; g_R > 0$). We mention that, $g_R = 2g_c$ due to the additional exchange interaction term which exists only in the condensate-reservoir interaction. The reservoir density $n_R(\vec{r},t)$ is controlled by the external pump rate (particle injection rate) $P(\vec{r},t)$, the spontaneous decay rate γ_R and the stimulated decay rate $R|\Psi(\vec{r},t)|^2$. Depletion of reservoir density due to stimulated emission into the condensate mode is taken into account by the $R|\Psi(\vec{r},t)|^2 n_R(\vec{r},t)$ term. Polaritons relax at an effective rate $\gamma_R \gg \gamma_c$. Although the loss rate of bottleneck polaritons is generally of the same order of magnitude as the condensate one, the effective relaxation rate γ_R is much faster thanks to thermalization of bottleneck polaritons with the much larger bath of high energy excitations created by the pump laser [92]. There is no phase coherence in the reservoir mode, so that the simple rate equation for the density $n_R(\vec{r},t)$ is enough for describing such a dynamical system. The order parameter i.e. condensate wavefunction $\Psi(\vec{r},t)$ does not include the excitations which introduce the amplitude and phase fluctuations for the condensate. If the pump rate $P(\vec{r},t)$ is independent of time, both condensate and reservoir are expected to establish steady state solutions [7].

When the ground state has a large population, the simulated decay rate $R|\Psi(\vec{r},t)|^2$ in is maximum at the condensate center and lower at the condensate peripheral. Consequently, the reservoir density $n_R(\vec{r})$ has a population dip at the center. The unusual spatial distribution of $n_R(\vec{r})$ gives a considerately higher gain $Rn_R(\vec{r})$ for higher energy states, so that they capture a macroscopic population and creates condensate fragmentation. Before they cool down to the ground state, they decay as photons and captured by detectors. If there is no reservoir density, $n_R(\vec{r}) = 0$, and a condensate lifetime is infinitely long, such condensate fragmentation is not formed.

Another remarkable feature is a gain-induced trapping mechanism. In the numerical model, it is assumed that an external trap potential is negligible, $V_{ext}(\vec{r}) \sim 0$. Nevertheless, clear trapped mode structures appear. This is because the pump profile $P(\vec{r})$ has a spatial dependence and condensate particles can be trapped by the imaginary part, $iRn_R(\vec{r})$, of the trap potential energy rather than the real part, $V_{ext}(\vec{r})$, in this case. The above example suggests that the properties of a dynamical condensate described by the open dissipative Gross-Pitaevskii equation and are different from those of an equilibrium BEC. Probably the most subtle issue among them is the quantum fluctuations of the amplitude and phase of the condensate order parameter [7, 78].

1.12 Similarities and differences between atomic BEC and exciton-polariton BEC

Since the realization of Bose-Einstein condensation, the field of ultracold atoms has witnessed an explosive growth. Nowadays, many experiments are performed on atoms of bosonic and fermionic statistics, that can be combined with ions and strongly coupled to light. Quantum degeneracy is reached when the de Broglie wavelength reaches the value of around 1 micron and the maximum density of the atoms is around $n = 10^{14}\ cm^{-3}$ [84]. Due to the much heavier atomic mass, the temperature requirement for the atoms is much more severe and of the order of $100\ nK$, eight orders of magnitude smaller than in the polariton case. Thanks to the excellent isolation of the atomic clouds from any environment, these ultralow temperatures can however be routinely achieved. Being a unique system of fundamental interest, exciton-polaritons possess many experimental advantages over ultra coldatoms for BEC research. Most notable is the light effective mass of polaritons in the region $k_\parallel \ll k_c$. Taking into account excitonlike dispersion at higher $k_\parallel$, the critical temperatures of exciton-polariton BEC range from criogenic temperature of a few kelvin up to room temperature and higher. This simplifies enormously the experimental setups for polariton research. Beside this it makes polaritons a natural and practical candidate for quantum device applications [5, 82–84].

In contrast to conventional condensed matter systems such as the electron gas or superfluid Helium, both the ultracold atoms and polariton gases are strongly inhomogeneous. The overall trapping potential acting on cold atoms is usually well approximated by a quadratic potential. In the polariton case, not only trapping potentials can be present, but also the excitation that injects particles is inhomogeneous. The physical consequences of the inhomogeneity are very different for systems at thermodynamic equilibrium and for nonequilibrium gases [84].

In the case of cold atoms in equilibrium, the effect of a shallow quadratic trapping potential can in good approximation be described in the local density approximation. This means that the gas can be treated locally as homogeneous at a given chemical potential $\mu(\vec{r})$. This chemical potential varies in space as $\mu(\vec{r}) = \mu_0 - V_{ext}(\vec{r})$, where V_{ext} is the trapping potential. What at first sight could seem to be a complication, actually turns out to be a convenience: one has access to a range of chemical potentials in a single experiment. Measuring the local density, it is possible to extract the equation of state $\mu(n)$, from which thermodynamic quantities such as the pressure and phase space density can be extracted [41, 84].

In the polariton case on the other hand, the inhomogeneity induces more complicated phenomena. Due to the nonequilibrium situation, that breaks time reversal symmetry, the steady state can sustain flows of polaritons. In other terms, the superfluid phase is not guaranteed to be homogeneous in the steady state. For a general inhomogeneous potential $V_{ext}(\vec{r})$ and inhomogeneous injection of particles $P(\vec{r})$, it is not possible to find a steady state with a uniform superfluid phase. Because of these flows, it is a much harder problem to find the steady state [84].

An advantage of both the atom and polariton systems is that the time scales of their dynamics are slower than the temporal resolution of the measurements. This allows to study the temporal dynamics of the observables. Moreover, the external forces acting on the systems can be varied fast with respect to the dynamics [41, 84].

For cold atoms, the collective excitations that are excited when the clouds are shaken have revealed a wealth of information on their properties. For example, the frequency of the breathing mode gives information on the equation of state, where the scissor mode is very sensitive to the superfluidity of the gas. Typically, the oscillation amplitude is moderate and the oscillation frequencies can be computed in linear response theory [41].

With respect to dynamics, the polariton system is intrinsically in a non-equilibrium situation when the driving compensates for the losses. One has to resort do descriptions of the dynamics to assess the properties of the stationary state. In most cases, the steady state of the ultracold atomic gases corresponds to a thermal state that can be described with statistical methods. The flexibility of ultracold atoms has however also generated proposals to study driven-dissipative dynamics with ultracold atoms, where an environment is engineered so to introduce nonequilibrium phase transitions and topological states of matter [84].

1.13 Thesis outline

In the following chapters I present the original work in this thesis:

- In Chapter 2, I study stability and mobility properties of matter-wave solitons created in attractive Bose-Einsten condensates in two-dimensional optical lattices. Then, I analyze the mechanism for controlled transport of matter-wave solitons based on the mean field theory. I show that the rocking optical lattices enable both the efficient stabilization and dynamical routing of solitons.

- In Chapter 3, I investigate the fundamental role of orbital angular momentum in the collapse dynamics of vortex-free elliptic BEC with attractive interaction. I analyse BEC clouds carrying orbital angular momentum in a quasi-two-dimensional radially-symmetric harmonic trap and a quasi-two-dimensional rotating elliptic trap. I show, both analytically and numerically, that for such rotating BEC clouds the collapse can be drastically suppressed well above the typical threshold numbers of trapped atoms.

- Chapter 4 and 5 focus on localization of the steady state polariton BEC with repulsive interations in untrapped and trapped regime. In chapter 4, I find that, even in the absence of external potentials, localization of the steady state polariton BEC can occur due to the effective self-trapping created by the polariton flows. In Chapter 5, I analyze the mechanism for localization of a dissipative polariton condensate with an external periodic potential. I show that dissipative nature of the polariton condensate gives rise to additional effective potentials local to the condensate. These additional effective potentials are responsible for the polariton condensate spatial localization.

Chapter 2

Controlled transport of ultra cold atom BECs in 2D optical lattices

2.1 Introduction

Scientific advances in atomic physics and optics that lead to coherent manipulation of translational motion of atoms have provided valuable tools for studying fundamental quantum mechanical phenomena, probing atomic and material properties. The *motion* here refers to center of mass displacements and *coherently* means with respect to the phase of the atomic de Broglie wave. Coherent manipulation of atomic motion which requires the atoms be treated as waves created new field in physics named *"atomic optics"*. Consequently, many techniques to control atom waves (matter waves) borrow seminal ideas from light optics. Applying these ideas to translational motion requires the development of techniques to localize atoms and transfer atoms coherently between two localities.

Controlled manipulation of stable, spatially localized matter waves is similar to routing of optical pulses in photonic devices [93, 94]. This is a very attractive goal from the viewpoint of emerging integrated technologies based on the use of ultracold atomic gases – Bose-Einstein condensates. Transport of cold atoms has already been explored in various approaches using magnetic and optical fields [45, 46, 95–105]. For instance, magnetic fields have been used to shift atoms on atom chips [95] and to move laser-cooled atomic clouds over macroscopic distances compared to their size [96, 97]. Another approach consisted of mechanically relocating the focusing lens of the optical dipole trap with a large translation stage [98]. This position change of the optical dipole enabled to transfer a BEC over tens of centimetres distances in several seconds.

In recent years optical lattices have been suggested as an instrument for controled transport of ultracold atoms over a long distance. It was demonstrated experimentally that the use of a special 1D optical lattice, which is formed by a Bessel laser beam and a counterpropagating Gaussian beam is allowed to realize transport of ultracold atoms [104]. The lattice part of the optical trap moved the atoms axially, whereas the Bessel beam led to radial confinement holding the atoms against gravity. Direct transport of matter-wave solitons loaded into a rapidly driven asymmetric 1D optical lattice –*"optical ratchet"* has been suggested theoretically [105] and demonstrated experimentally [106]. A useful insight into the transport properties in the optical ratchet potential was provided by *effective particle approach* for the mean field theory [107], which treats the extended matter-wave soliton as an *effective classical particle*.

Transport of matter waves in a 2D or 3D trapping geometry is a more complex and challenging task, especially considering the intrinsic instability – *"collapse"* of the selflocalizing condensate with the negative scattering length. Several methods of stabilization for nonlinearly localized atomic wave packets – matter-wave solitons, created in a 2D or 3D trapping geometry, have been extensively studied. Some methods rely on the time-periodic management [108, 109] of the condensate or nonlocal interaction between atoms [110]. Static optical lattices are also predicted to stabilize matter-wave solitons in 2D or 3D trapping geometry [111].

The problem of transport of localized nonlinear excitations in periodic potentials is acutely posed in several cross-disciplinary areas of physics [112] because periodic systems greatly inhibit the mobility of localized states. In particular, mobility of discrete solitons is an important problem in nonlinear photonics and lattice dynamics [113, 114]. In periodic structures and waveguide arrays, the motion of spatially localized optical beams is affected by the lattice periodicity, so that the effective Peierls-Nabarro potential [113] induced by the lattice prevents their free motion. It was shown that moving solitary waves in discrete lattices require a special type of saturable nonlinearity [115] and can move only at some limited velocities [116]. Mobility of discrete optical solitons in two-dimensional photonic lattices, after an initial kick, was also found for the case of quadratic nonlinear response that leads to parametric coupling of the fundamental and second-harmonic fields [117].

In this chapter, we propose and analyze the mechanism for controlled transport of two-dimensional matter-wave solitons, created in a Bose-Einstein condensate of atoms with a negative scattering length. The transport is realized by means of a rocking two-dimensional optical lattice [118], where the term "rocking" refers to time-periodic shaking of the lattice [119]. Our analysis, based on the mean-field model, demonstrates that the fast rocking of the lattice enables dynamical creation of reconfigurable mobility channels for matter waves. Similar channels were previously studied in the context of lattices that do not coincide in dimensionality with the wave packet and guide it along a fixed free spatial direction [120]. Here we show that the rocking optical lattices enable both the effcient stabilization and dynamical "routing" of solitons.

2.2 Model

The modelling of both nonlinear optical and nonlinear matter-wave dynamics is often based on the nonlinear Schrodinger equation (or GPE), which is used to describe both the electromagnetic field envelope and the BEC macroscopic wavefunction (mean-field). This model reflects similarities between the physics of coherent light and matter waves, which aid in understanding and predicting the nonlinear behavior of BEC in an optical lattice.

To describe the dynamics of bright solitons in a BEC loaded into a two-dimensional lattice, we consider a mean-field model of the system comprising a pancake trapping geometry for a cloud of ultracold atoms with an optical lattice potential aligned with the weak trapping directions. As long as the energy of the longitudinal excitations is not sufficient to excite the transverse modes of the condensate in the direction perpendicular to the optical lattice [45, 121], the system can be treated as two-dimensional and described by the Gross-Pitaevskii equation:

$$i\partial_t\psi + \Delta\psi + V_{\mathrm{OL}}(\mathbf{r},t)\psi + |\psi|^2\psi = 0, \tag{2.1}$$

where $\Delta = \partial_x^2 + \partial_y^2$, and $\mathbf{r} = (x, y)$. The dimensionless form is derived by using

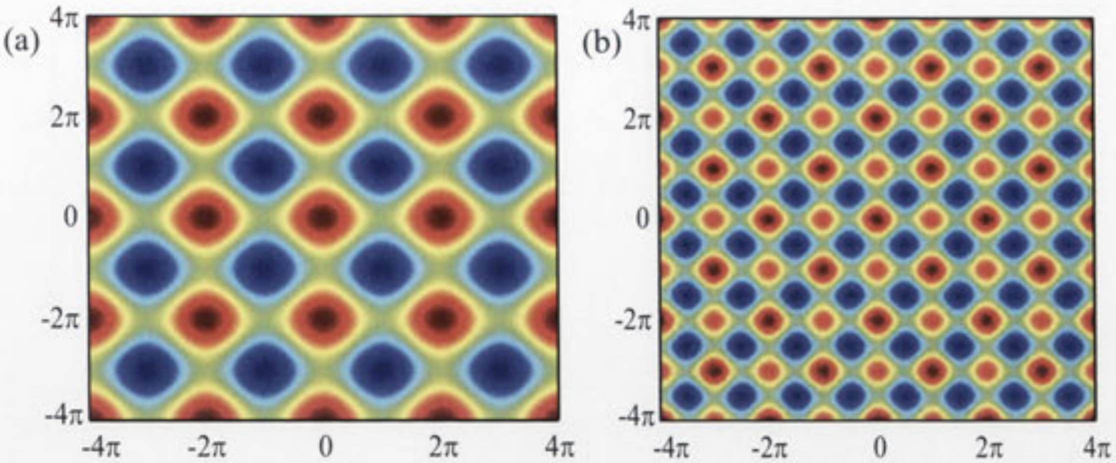

Figure 2.1: Optical lattice potentials of Equation (2.2) (a) and Equation (2.3) (b) at $t = 0$. Parameters are: (a) V_x=V_y=0.5; (b) V_0=0.16, and V_x=V_y=0.5.

the natural lattice units of energy $E_L = \hbar^2 k_L^2/(2m)$, length $a_L = 1/k_L$, and frequency $\omega_L = E_L/\hbar$, where k_L is the wavevector of the optical lattice, and m is the mass of the atoms. The three-dimensional mean-field model is reduced to the two-dimensional GPE by assuming that the wavefunction is separable in the following manner: $\psi_{3D}(x, y, z) = \psi_{2D}(x, y)\phi_{1D}(z)$, where $\phi_{1D}(z)$ is the ground state wavefunction of the one-dimensional harmonic oscillator with the transverse trapping frequency ω_z. It has normalization condition as $\int |\phi_{1D}(z)|^2 dz = 1$. With these assumptions, the wavefunction ψ in Equation (2.1) relates to ψ_{2D} as follows: $\psi = \psi_{2D}\sqrt{g_{2D}}$, where $g_{2D} = 4\sqrt{\pi}(a_s/a_z)(\omega_z/\omega_L)^{1/2}$ is the renormalized interaction coefficient that characterizes s-wave scattering of the condensate atoms with the scattering length a_s. Number of atoms in the system is given by: $\mathcal{N} = N/g_{2D}$, where $N = \int |\psi|^2 dx$ is the norm of the dimensionless wavefunction.

For the ^7Li atoms with the scattering length $a_s = -0.21$ nm, trapped using using a CO_2 laser with $\lambda = 10.62$ μm [10], the physical values of the characteristic scales are: $a_z = 845$ nm, $\omega_z = 2\pi \times 2039$ Hz. For these parameters, the rescaled nonlinear coefficient is $g_{2D} = 1.03 \times 10^{-3}$, and the typical nonlinear localized state in our system has the norm $N \approx 10$, which corresponds to the number of atoms $\mathcal{N} \sim 10^4$. The actual maximum value of N, found numerically from Equation (2.1) with $V_{\text{OL}} = 0$ is $N_{max} = 11.7 \approx 0.93\tilde{N}_{max}$, where $\tilde{N}_{max} = 4\pi$ is the well-known *varational approximation* prediction. In the Equation (2.1) with $V_{\text{OL}} = 0$ localized configurations with $N > N_{max} = 11.7$ suffer collapse, while those with $N < N_{max}$ decay. The static optical lattice stabilizes 2D solitons against decay, but it cannot arrest the collapse of initial localized states with $N > N_{max}$ [108].

It has been shown that 2D optical lattices can be realized with $2+1$ independent laser beams or two pair of counter propagating laser beams [122]. We consider two rocking optical lattices with different forms in Equation (2.1) for achieving dynamically controllable transport. The potentials can be presented as follows:

$$V_{\text{OL}}(\mathbf{r}, t) = V_x \cos[x - X(t)] + V_y \cos[y - Y(t)], \tag{2.2}$$

$$V_{\text{OL}}(\mathbf{r}, t) = V_0 \cos[x - X(t)] \cos[y - Y(t)] + V_x \cos[2x - X(t)] + V_y \cos[2y - Y(t)]. \tag{2.3}$$

Here V_0, V_x and V_y are optical lattice heights. $X(t) = X_0 \sin(\omega t)$ and $Y(t) = Y_0 \sin(\omega t)$ correspond to time-periodic shaking of optical lattices in x and y directions respectively.

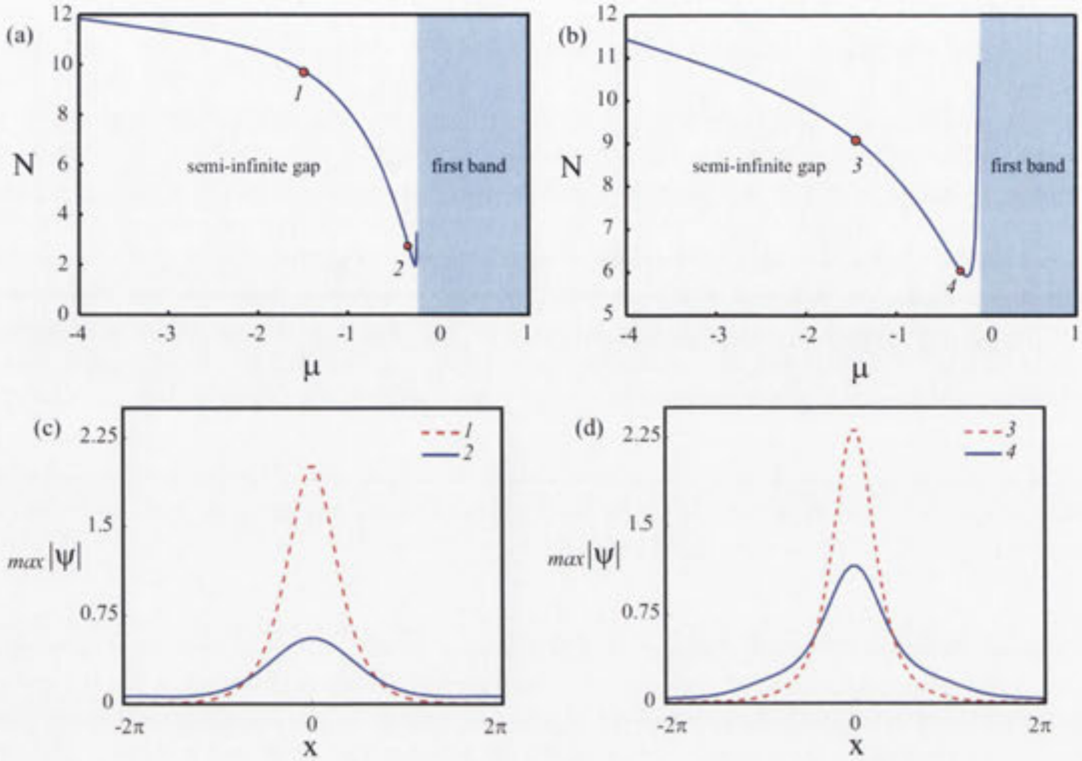

Figure 2.2: (a,b) Families of stationary state solitons as $N(\mu)$ curve corresponding to static optical lattice potentials in Figure 2.1. (c,d) Cross-sections along the x-dimension of matter wave solitons with $\mu = -1.5$ (dots 1,3) and $\mu = -0.3$ (dots 2,4).

The optical lattice potential of Equation (2.2) can be created by the interference of two pairs of laser beams with ortogonal polarizations. The other lattice potential of Equation (2.3) can be constructed from two 2D lattices with different spatial periods, resulting in a 2D lattice whose unit cell contains double sites. Within the pair, the barrier height and relative depths of the lattice sites are controllable [123]. Lattices are driven periodically, i.e. the phase detuning between the laser beams forming the lattice is modulated. By using a Fourier decomposition of the lattice potential, it is easy to see that the optical lattices have two components, a time-independent "backbone" lattice and a time-dependent component. This clearly distinguishes the transport in such a potential from the recently suggested and analyzed ratchet-type transport of matter-wave soliton [105]. In our system the time-average force acting upon a wave-packet at any given point in space is non-zero.

Stationary states and Vakhitov-Kolokolov stability criterion

The stationary states of a condensate in an infinite 2D static optical lattice ($\omega = 0$ or $t = 0$) are described by solutions of GPE of the form: $\psi(\mathbf{r}, t) = \Psi(\mathbf{r}) \exp(-i\mu t)$, where μ is the corresponding chemical potential. The resulting time independent GPE is then solved numerically using relaxation methods developed in [124]. Alternatively lattice solitons can be formed by modulational instability [125]. We find families of stationary state solitons corresponding to given potentials in Equations (2.2,2.3) that exist in the semi-infinite band gap below the first band. In Figure 2.2 these families are represented by dependencies of soliton norm $N = \int |\psi(x,y)|^2 dxdy$ on its chemical potential. When soliton's chemical potential is close to the lowest energy band, lattice soliton is broad. The width of soliton becomes narrow as chemical potential is lowered [see Figure 2.2(c,d)].

The existence $N(\mu)$ curves also give information on stability of the solitons. For BEC with attractive interatomic interactions the stability can be determined by analysing the slope of the norm curve [126]. More specifically, when $\partial N/\partial \mu < 0$, the solitons are stable, while close to band $\partial N/\partial \mu > 0$ and the lattice solitons become unstable. This remarkable connection between stability and and slope of the norm curve $N(\mu)$ was first discovered by Vakhitov and Kolokolov in 1973 and is now called *Vakhitov-Kolokolov stability criterion*.

2.3 Mobility and Peierls-Nabarro potential

In order to study the transport of localized matter-wave solitons, one has to generate mobile localized states. The mobility of the matter-wave solitons in the optical lattice is suppressed due to the energy difference between the nonlinear localized states with the same N but different symmetry that needs to be overcome in order to move the initially stationary state across the lattice. This is analogous to the Piers-Nabarro potential in the discrete systems. On the other hand, it is the strong coupling to the lattice that both stabilizes the solitons against the collapse threshold and enables to manipulate the localized states by changing parameters of the lattice. The typical norm of a two-dimensional soliton considered in our dynamical simulations below is near the collapse threshold for a free soliton, which for our normalization is $N_{max} = 11.7$ [108].

The Piers-Nabarro potential

The concept of the Piers-Nabarro potential barrier originates from the theory of dislocations and later studies of mobility of localised nonlinear excitations in discrete lattices. The Piers-Nabarro potential is introduced as the height of the effective periodic potential generated by the lattice discretness and it defines the minimum energy required to move the center of mass of the localised wavepacket. Extending this definition to continuous lattice model, one can define the Piers-Nabarro potential as the energy difference between solitons centered at local extrema of a periodic potential.

A soliton solution of 2D GPE can be characterised by its dynamical invariants: number of atoms and energy. The energy functional for 2D GPE with static optical lattices can be found in the following form:

$$E = \int_{-\infty}^{\infty} [|\nabla\psi|^2 + V_{\text{OL}}(\mathbf{r}, t=0)|\psi|^2 + \frac{1}{2}|\psi|^4] dxdy \tag{2.4}$$

One can find stationary soliton solutions with a fixed number of atoms sweeping their center of mass (either axial or diagonal) via solving Equation (2.1) numerically, and calculate the energy for each solutions. For defined diriection (axial or diagonal) in 2D optical lattice with a single periodicity,

$$V_0^{PN} = E_{\text{max}} - E_{\text{min}}, \tag{2.5}$$

where V_0^{PN} is the Piers-Nabarro potential and E_{max} and E_{min} are the energies of the stationary states centered at local extrema: E_{max} corresponds to the energy of soliton state centered at lattice maximum for mobility analysis in diagonal directions. In the case of axial mobility analysis, $E_{\max}$ is the energy of soliton state centered at lattice saddless point. $E_{\min}$ is the energy of soliton solution at local minimum of the periodic potential. Since these stationary states can represent a moving mode at different times, the Piers-Nabarro potential can be understood as the smallest amount of energy that a stationary soliton needs to gain in order to start moving along the lattice. Good mobility should be expected in directions where lattice potential surfaces are smooth and flat.

2.4 Variational approach

Variational methods are quite useful analytical tool for analyzing many problems of nonlinear optics and BEC. Approximate solutions for Equation (2.1) in the form of nonlinear localazed states can be derived using variational approach (VA). To apply the VA to the present model, we notice that Equation (2.1) can be derived from the Lagrangian $L = \int_{-\infty}^{+\infty} \mathcal{L} dx dy$, with the density

$$\mathcal{L} = \frac{\mathrm{i}}{2}\left(\psi^* \frac{\partial \psi}{\partial t} - \psi \frac{\partial \psi^*}{\partial t}\right) - |\nabla \psi|^2 + V_{\mathrm{OL}}(\mathbf{r}, t)|\psi|^2 + \frac{1}{2}|\psi|^4, \tag{2.6}$$

where the asterisk stands for the complex conjugation. We adopt the approximated solution of Equation (2.1) with optical lattice in the form of Gaussian function:

$$\psi(\mathbf{r}(t), \mathbf{r_0}(t)) = A(t) \exp\left[i\phi(t) + \frac{i}{2} b(\mathbf{r}(t) - \mathbf{r_0}(t))^2 + \frac{(\mathbf{r}(t) - \mathbf{r_0}(t))^2}{2a(t)^2}\right]. \tag{2.7}$$

Here $\mathbf{r_0(t)} = (x_0(t), y_0(t))$ is the initial position of the soliton's center of mass. The amplitude $A(t)$, phase $\phi(t)$, chirp $b(t)$ and the width of the soliton $a(t)$ in the ansatz are real. As we introduced two rocking optical lattices, we begin our analitical analysis with optical lattice given in Equation (2.2). The substitution of the ansatz into Equation (2.6) and calculation of the integrals yield the effective Lagrangian,

$$L_{\mathrm{eff}} = N_{\mathrm{va}}\left(-\frac{d\phi}{dt} - \frac{1}{a^2} + \frac{N_{\mathrm{va}}}{4\pi a^2} + \frac{V_{\mathrm{eff}}(\mathbf{r_0}, t)}{N_{\mathrm{va}}} - \frac{1}{2}\frac{db}{dt}a^2 - \frac{1}{2}b^2 a^2\right), \tag{2.8}$$

with the norm:

$$N_{\mathrm{va}} = \int |\psi(\mathbf{r}, \mathbf{r_0})|^2 d\mathbf{r} = \pi A^2 a^2, \tag{2.9}$$

and an effective lattice potential:

$$V_{\mathrm{eff}}(\mathbf{r_0}, t) = [V_x \cos(x_0 - X) + V_y \cos(y_0 - Y)] \exp\left(-\frac{a^2}{4}\right). \tag{2.10}$$

The norm in Equation (2.9) relates the soliton's amplitude to its width. Using the Euler-Lagrange equation for variational parameters we derive the following variational equations.

$$b = \frac{1}{a}\frac{da}{dt}, \tag{2.11}$$

$$\frac{d^2 a}{dt^2} = \frac{1 - N_{\mathrm{va}}/\tilde{N}_{max}}{a^3} - \frac{a}{4}[V_x \cos(x_0 - X) + V_y \cos(y_0 - Y)] \exp\left(-\frac{a^2}{4}\right). \tag{2.12}$$

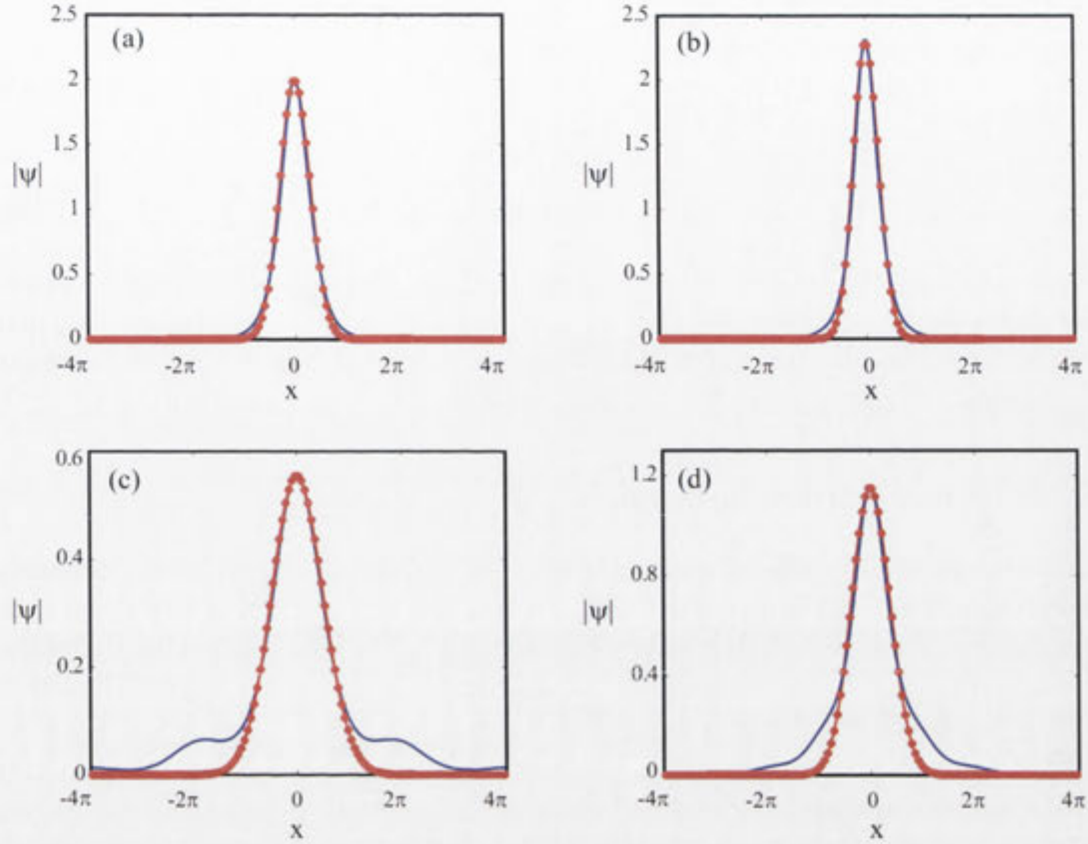

Figure 2.3: Cross-sections of the approximate solution (dotted) and the exact stationary solution profiles (solid) along x-dimension with μ=-1.5 (a,b) [dots (1,3) in Figure 2.2] and μ=-0.3 (c,d) [dots (2,4) in Figure 2.2].

It can be seen that the expression (2.11) for the chirp is defined in terms of the time derivative of the width. $\tilde{N}_{max} = 4\pi$ in Equation (2.12) is critical (maximum) norm in 2D space predicted by the variational theory. Maximum norm separates collapsing solutions $N_{\text{va}} > \tilde{N}_{max}$ from stable solutions $N_{\text{va}} < \tilde{N}_{max}$. Assuming that the soliton's width is constant, we can derive the norm of a lattice soliton from Equation (2.12) at the initial time ($t = 0$) and position, ($x_0 = 0, y_0 = 0$),

$$N_{\text{va}} = 2\pi \left[2 - Va^4 \exp\left(-\frac{a^2}{4} \right) \right], \tag{2.13}$$

where $V = V_x = V_y$. The norm in Equation (2.13) relates the soliton's width to the optical lattice height. The substitution of Equation (2.9) into Equation (2.13) implies the following expression for the soliton's amplitude,

$$A = \sqrt{\frac{4}{a^2} - 2Va^2 \exp\left(-\frac{a^2}{4} \right)}. \tag{2.14}$$

Similarly equations for the norm and the amplitude of a soliton loaded into double well optical lattice given by Equation (2.3) can be expressed in term of lattice heights and the soliton's width,

$$N_{\rm va} = 4\pi\left[1 - a^4\left(\frac{V_0}{2}\exp\left(-\frac{a^2}{2}\right) + 2V\exp(-a^2)\right)\right], \tag{2.15}$$

$$A = \sqrt{\frac{4}{a^2} - a^2\left(\frac{V_0}{2}\exp\left(-\frac{a^2}{2}\right) + 2V\exp(-a^2)\right)}. \tag{2.16}$$

The variational theory shows that the approximate solution profile is in good agreement with the exact stationary solution for values of μ far from the band edge, such that the soliton is well localized in space. However, the approximate solution no longer agrees with the exact stationary solution for values μ near the band edge [see Figure 2.3].

2.5 Effective particle approach

To understand mobility properties and the effect of the rocking optical lattice potentials on the dynamics of a collective excitation in the BEC, we consider a single localized state in the form of 2D bright soliton given by Equation (2.7). The Hamiltonian theory for the mean field allows us to write an effective energy integral $\mathcal{H}(x,t)$ assosiated with Equation (2.1),

$$\mathcal{H}(x,t) = \int_{-\infty}^{\infty}[|\nabla\psi|^2 + V_{\rm OL}(\mathbf{r},t)|\psi|^2 + \frac{1}{2}|\psi|^4]dxdy. \tag{2.17}$$

The calculation of integrals and normalization of Equation (2.17) yealds the following form ,

$$H = \frac{\mathcal{H}}{N} = \frac{1}{a^2} + \frac{N}{4\pi a^2} + V_{\rm eff}(\mathbf{r_0},t). \tag{2.18}$$

To find the conditions of enhanced mobility in lattices we assume that a mobile soliton does not significantly change its form and can be described solely by the dynamics of the center of mass. The Hamiltonian theory i.e., the effective particle approach (EPA) [107] allows us to make intuitive predictions about the transport properties of the soliton as an effective classical particle in the external effective potential,

$$V_{\rm eff}(\mathbf{r_0},t) = \frac{1}{N}\int_{-\infty}^{\infty}|\psi(\mathbf{r},\mathbf{r_0})|^2 V_{\rm OL}(\mathbf{r},t)d\mathbf{r}. \tag{2.19}$$

where $d\mathbf{r} \equiv dxdy$.

Our further analysis is done considering the rocking optical lattice in Equation (2.2). Subsequently it can be generalized for the rocking double-well optical lattice in Equation (2.3). Following the Hamiltonian theory for the effective particle, we can write classical equation of motion for the soliton center of mass,

$$\frac{d^2\mathbf{r_0}}{dt^2} = -\frac{dV_{\rm eff}(\mathbf{r_0})}{d\mathbf{r_0}},$$

as

$$\frac{d^2x_0}{dt^2} = V_x e^{-\frac{a^2}{4}}\sin(x_0 - X), \qquad \frac{d^2y_0}{dt^2} = V_y e^{-\frac{a^2}{4}}\sin(y_0 - Y).$$

Provided that the frequency of rocking, ω, is faster than any frequency of collective motion in the system, we can separate the motion of soliton's center of mass into the slow and fast components: $x_0(t) = X_s(t) + \xi(t)$, $y_0(t) = Y_s(t) + \eta(t)$, where the typical

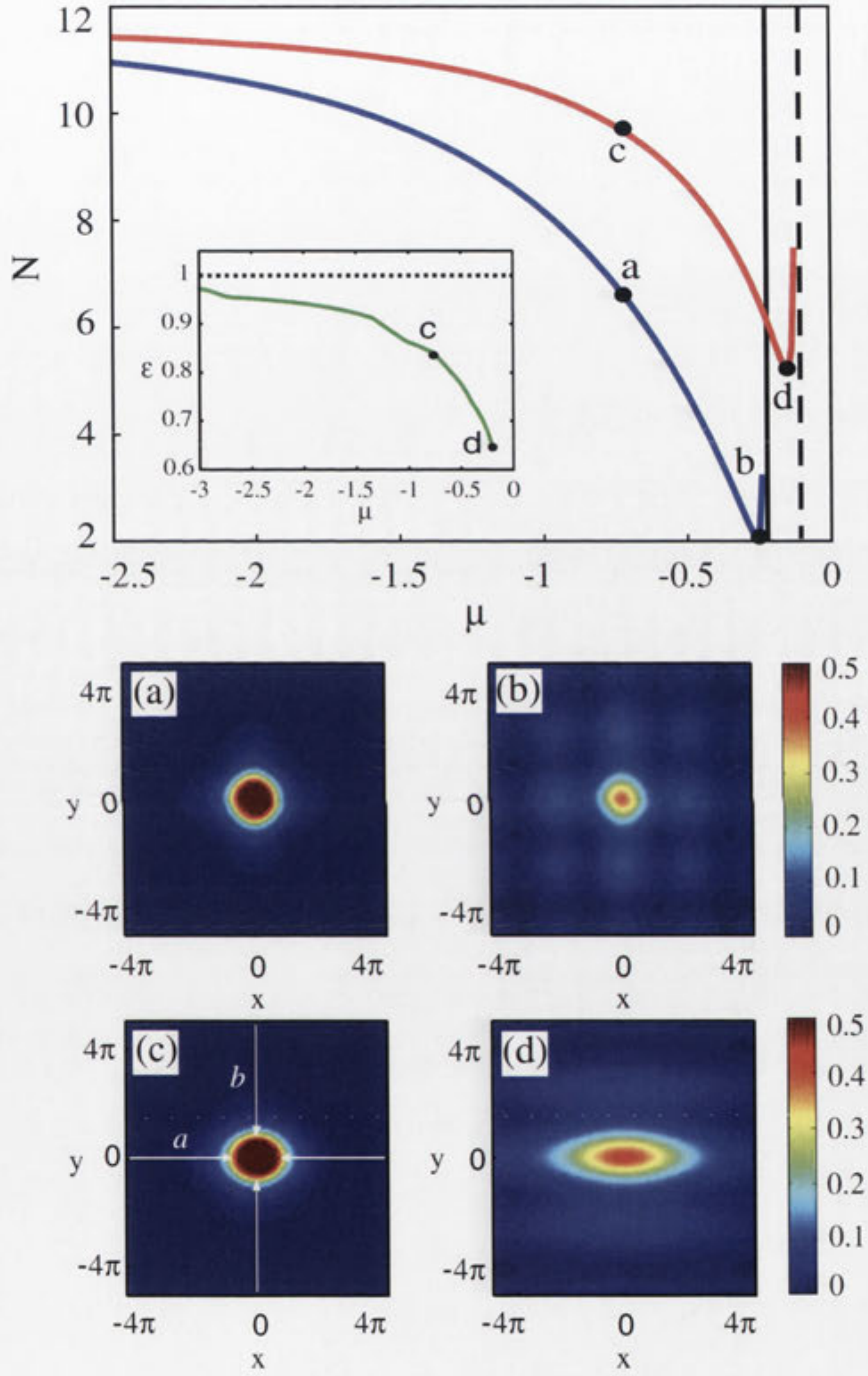

Figure 2.4: Norm of the wavefunction corresponding to a stationary soliton state in a rocking lattice potential $V(\mathbf{t}, \mathbf{t})$ at $t = 0$ (curve a-b) and in a time-averaged potential $V_s(\mathbf{R_s})$ (curve c-d) with $Y_0 = 0$, $X_0 = 2.4$.Bottom panels (a-d) show spatial structure (density $|\psi|^2$) of matter-wave solitons at the marked points on $N(\mu)$ curve. Inset: Aspect ration $\epsilon = b/a$ of the 2D stationary soliton in the time-averaged conservative potential.

evolution of the slow variables $\mathbf{R_s} = (X_s, Y_s)$ occurs on the time scale $\tau \gg \omega^{-1}$. We write equations of motion for the slow and fast components of soliton's center of mass,

$$\begin{aligned} \frac{\partial^2 \xi}{\partial t^2} &= V_x e^{-\frac{a^2}{4}} \sin(X_s - X(t)), \\ \frac{\partial^2 \eta}{\partial t^2} &= V_y e^{-\frac{a^2}{4}} \sin(Y_s - Y(t)), \end{aligned} \tag{2.20}$$

$$\begin{aligned} \frac{d^2 X_s}{dt^2} &= -\frac{d^2 V_{\text{eff}}}{dX_s^2}\xi = V_x e^{-\frac{a^2}{4}} \cos(X_s - X(t))\xi, \\ \frac{d^2 Y_s}{dt^2} &= -\frac{d^2 V_{\text{eff}}}{dY_s^2}\eta = V_y e^{-\frac{a^2}{4}} \cos(Y_s - Y(t))\eta. \end{aligned} \tag{2.21}$$

We expand Equation (2.20) and Equation (2.21) into harmonic function series. The constants of series have the form of Bessel functions of the fist kind: $J_n(X_0)$. We choose values of driving amplitudes, (X_0, Y_0) such as $J_0(X_0) = J_0(Y_0) = 0$. In this case solutions of Equations (2.20) i.e., fast components of the soliton center of mass: ξ and η are time dependant via harmonic functions. Substituting ξ and η into Equation (2.21) we can obtain equations of motion for slow part of the soliton center of mass in the following form,

$$\begin{aligned} \frac{d^2 X_s}{dt^2} &= V_x^2 e^{-\frac{a^2}{2}}(-2J_2(X_0)\cos(2\omega t)\cos(X_s) + 2J_1(X_0)\cos(\omega t)\sin(X_s)) \\ &\quad (\frac{1}{2\omega^2}J_2(X_0)\cos(2\omega t)\sin(X_s) + \frac{2}{\omega^2}J_1(X_0)\cos(X_s)\cos(\omega t)), \\ \frac{d^2 Y_s}{dt^2} &= V_y^2 e^{-\frac{a^2}{2}}(-2J_2(Y_0)\cos(2\omega t)\cos(Y_s) + 2J_1(Y_0)\cos(\omega t)\sin(Y_s)) \\ &\quad (\frac{1}{2\omega^2}J_2(Y_0)\cos(2\omega t)\sin(Y_s) + \frac{2}{\omega^2}J_1(Y_0)\cos(Y_s)\cos(\omega t)). \end{aligned} \tag{2.22}$$

The time averaging procedure over fast ocsillation, i.e. integration of Equation (2.21) over the period $T = 2\pi/\omega$ is then applied to derive equations of motion for the slow (compared to the driving frequency) dynamics of the soliton center of mass, $\mathbf{R_s} = (X_s, Y_s)$, in a driven lattice,

$$d^2\mathbf{R_s}/dt^2 = -dV_s(\mathbf{R_s})/d\mathbf{R_s},$$

as

$$\begin{aligned} \frac{d^2 X_s}{dt^2} &= \frac{V_x^2 e^{-\frac{a^2}{2}}}{4\omega^2}\sin(2X_s)\left\{4\left[J_1(X_0)\right]^2 - \left[J_2(X_0)\right]^2\right\}, \\ \frac{d^2 Y_s}{dt^2} &= \frac{V_y^2 e^{-\frac{a^2}{2}}}{4\omega^2}\sin(2Y_s)\left\{4\left[J_1(Y_0)\right]^2 - \left[J_2(Y_0)\right]^2\right\}. \end{aligned} \tag{2.23}$$

The time-averaged effective potential can be deduced from Equation (2.23). It has a separable form as follows:

$$V_s(\mathbf{R_s}) = A_{sx}\cos(2X_s) + A_{sy}\cos(2Y_s), \tag{2.24}$$

with the potential strength explicitly depending on the driving frequency, ω, and on the characteristic width of the soliton loaded into the lattice, a:

$$\begin{aligned} A_{sx} &= (V_x^2/8\omega^2)\exp\left(-a^2/2\right)\left\{4\left[J_1(X_0)\right]^2 - \left[J_2(X_0)\right]^2\right\}, \\ A_{sy} &= (V_y^2/8\omega^2)\exp\left(-a^2/2\right)\left\{4\left[J_1(Y_0)\right]^2 - \left[J_2(Y_0)\right]^2\right\}. \end{aligned}$$

Taking into account the rocking optical lattice potential given in Equation (2.3) and applying the EPA, we can also derive time-averaged effective potential corresponding to Equation (2.3).

$$\begin{aligned} V_s(X_s) &= \left(\frac{V_0^2 e^{-a^2}}{8\omega^2}\cos(2X_s)\cos(Y_s) + \frac{V_x^2 e^{-2a^2}}{16\omega^2}\cos(4X_s)\right)\left\{4\left[J_1(X_0)\right]^2 - \left[J_2(X_0)\right]^2\right\}, \\ V_s(Y_s) &= \left(\frac{V_0^2 e^{-a^2}}{8\omega^2}\cos(X_s)\cos(2Y_s) + \frac{V_y^2 e^{-2a^2}}{16\omega^2}\cos(4Y_s)\right)\left\{4\left[J_1(Y_0)\right]^2 - \left[J_2(Y_0)\right]^2\right\}. \end{aligned} \tag{2.25}$$

We stress that the time-averaged potentials are *conservative* in the presence of driving at certain values of X_0 and Y_0, time modulation amplitudes of lattices, namely such that $J_0(X_0) = 0$ or $J_0(Y_0) = 0$. When $J_0(X_0) \neq 0$ and $J_0(Y_0) \neq 0$, fast components of the soliton center of mass are dependent to time in quatratic form, such as $\xi \sim t^2$ and $\eta \sim t^2$. This dependency does not allow for the time averaging over fast ocsillations and the effective potential will no longer be conservative.

The time-averaged conservative potentials, V_s, support stationary localized matter-wave soliton solutions. Figure 2.4 presents the family of the solitons in V_s (c-d) corresponding to Equation (2.24). According to the Vakhitov-Kolokolov stability criterion, these solitons are dynamically stable in the entire existence region of the solitons supported by the static lattice potential $V_{\mathrm{OL}}(\mathbf{r}, 0)$. This is due to the fact that the band edge in V_s is shifted to the lower values of the chemichal potential, μ (dashed vertical line Figure 2.4) and indicates that the rocking driving leads to stabilization of the moving solitons below the collapse threshold, as predicted for amplitude-modulated optical lattices [108]. Secondly, for the same values of μ, the mobility of the solitons in the effective potential is expected to be enhanced compared to those in the static lattice due to the lower effective Peierls-Nabarro potential.

2.6 Dynamics and manipulation of matter-waves in 2D rocking optical lattices

First, in order to confirm the predictions of improved mobility of the localized states in the driven lattice, we compare the dynamics of two initially stationary states corresponding to $\mu = -0.7$ and supported by $V_{\mathrm{OL}}(\mathbf{r}, 0)$ and V_s potentials (points a and c in Figure 2.4). The result of this comparison is shown in Figure 2.5. At the time $t = 0$ both the initial states are given a "kick" in the x-direction and the initial velocity of the two solitons are exactly the same. Nevertheless, the soliton, supported by the static optical lattice $V_{\mathrm{OL}}(\mathbf{r}, 0)$ (point a in Figure 2.4) decays almost instantly, whereas the soliton supported by the V_s in the driven lattice (point c in Figure 2.4) engages in ballistic motion and retains its shape. Next, we demonstrate the basic principles of dynamical transport

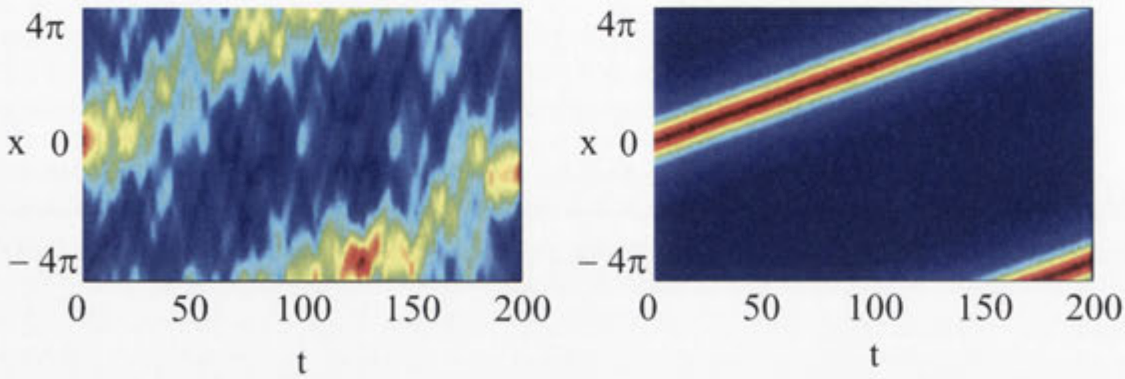

Figure 2.5: Dynamics of a moving soliton in the rocking lattice obtained by solving Equation (2.1) numerically with periodic boundary conditions. Initial states are (a) a stationary soliton of the potential $V(\mathbf{r},\mathbf{0})$ at $\mu = -0.7$ [Figure 2.4 a] and (b) a stationary soliton of the time-averaged potential $V_s(\mathbf{R_s})$ at $Y_0 = 0$, $X_0 = 2.4$, $\mu = -0.7$ [Figure 2.4 c].

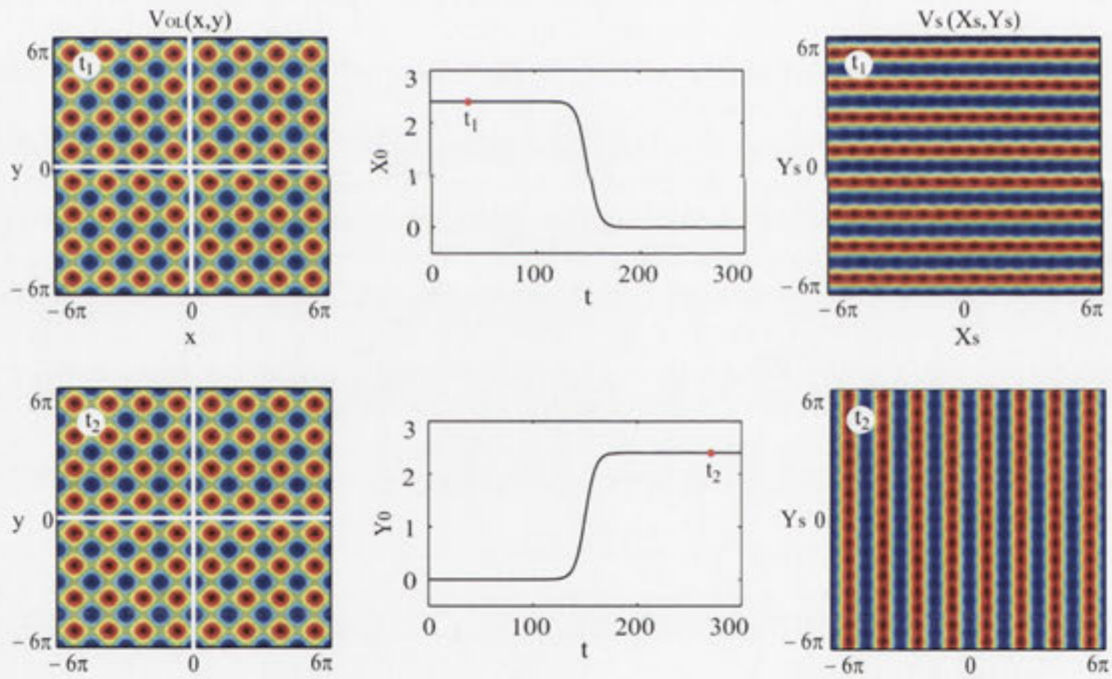

Figure 2.6: Dynamical control of the optical lattice parameters enabling creation and switching of the soliton mobility channels in the time-average potential. Left column: Rocking optical lattice potential V_{OL} at the instances of time t_1 and t_2; the lines marking $x = 0$ and $y = 0$ are guides to the eye. Middle column: Time dependence of the rocking amplitudes. Right column: Time-averaged lattice potential $V_s(\mathbf{R_s})$, corresponding to $Y_0 = 0$, $A_{sy} = 0.5, A_{sx} = 0.002$ (at t_1) and $X_0 = 0$, $A_{sx} = 0.5, A_{sy} = 0.002$ (at t_2).

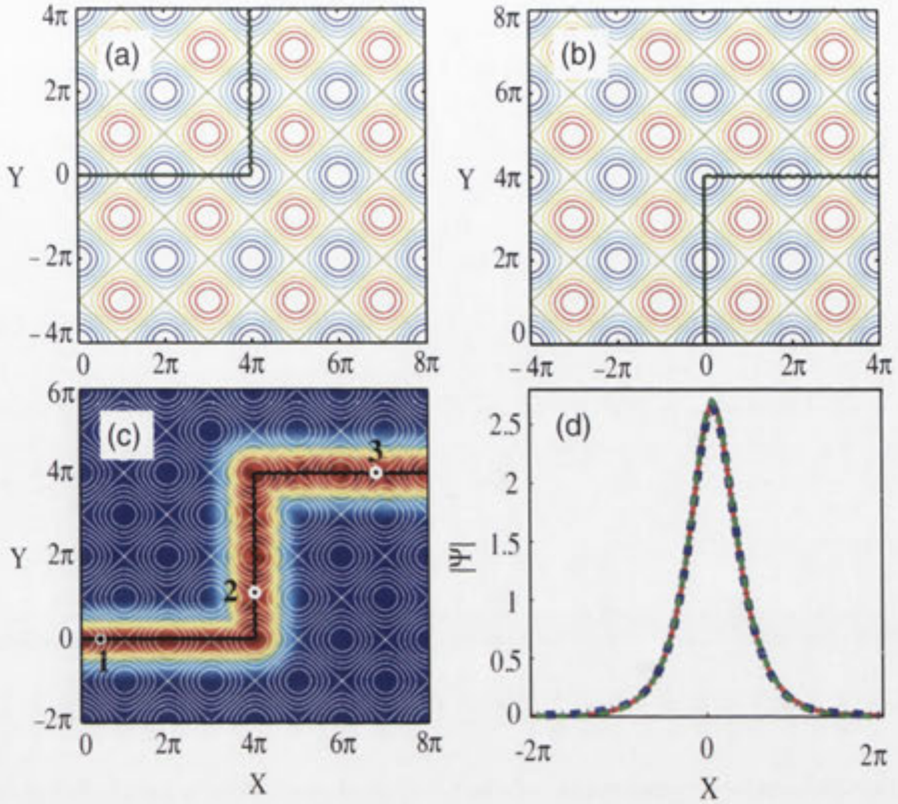

Figure 2.7: (a,b) Center of mass trajectory of a moving soliton corresponding to $\mu = -2$ in a rocking lattice potential $V_{\mathrm{OL}}(x, y, t)$, superimposed onto the contour plot of the potential at $t = 0$, and, in (c), with the density plot of the moving soliton profile. Sharp turning points correspond to the switching of the mobility channels as shown in Figure 2.6. (d) The profiles of the moving soliton corresponding to the points 1 (solid), 2 (dashed), and 3 (dash-dotted) in (c).

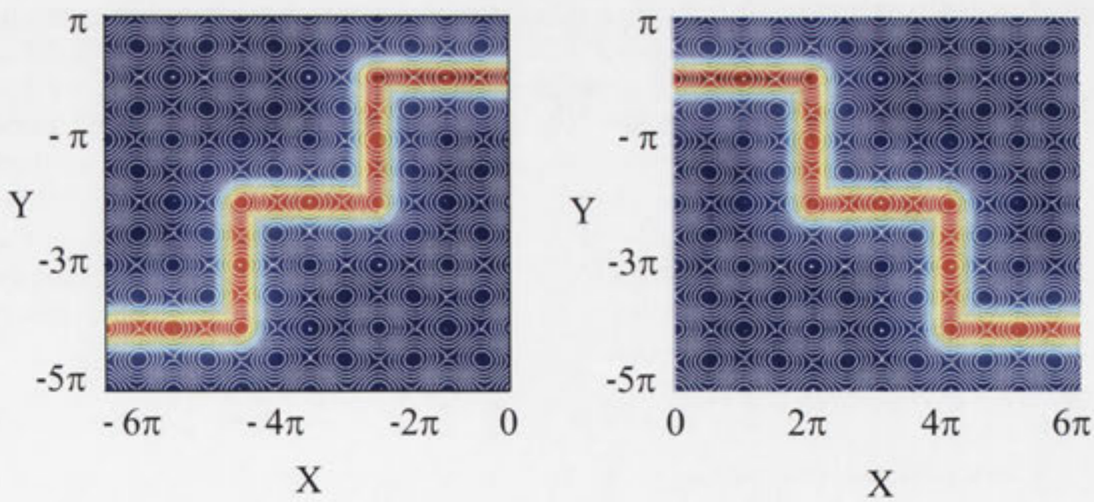

Figure 2.8: Complex center of mass trajectory of a moving soliton corresponding to $\mu = -2$ in a rocking double well lattice potential $V_{\mathrm{OL}}(\mathbf{r}, t)$, superimposed onto the contour plot of the potential at $t = 0$, with the density plot of the moving soliton profile. Sharp turning points correspond to the switching of the mobility channels.

control of the mobile solitons in the driven lattice. While the driven lattice potential, $V_{\rm OL}$ is not stationary, and the positions of its maxima and minima are different at various time instances (cf. instantaneous images of $V_{\rm OL}$ at t_1 and t_2 in Figure 2.6, left column), its action on the soliton center of mass at any given moment of time can be described by the conservative potential V_s. By examining the form of the time-averaged potential in Equation (2.24), one can see that the amplitude of the spatial modulation can be effectively suppressed in one of the orthogonal directions by controlling the amplitude of the periodic driving. The most dramatic example of such suppression is presented in Figure 2.6. During the periods of time when the amplitudes of driving X_0 and Y_0 are kept constant (segments marked by the points t_1 and t_2 in Figure 2.6, middle column), one of the amplitudes, X_0 or Y_0, is set to zero, and the time-averaged potential has a form of a two-dimensional lattice with the spatial modulation amplitude A_{sx} or A_{sy} radically suppressed, but not equal to zero (see Figure 2.6, right column). Thus the mobility channels in one of the orthogonal directions are effectively created in the two-dimensional lattice for any localized state. This effective lattice is fully reconfigurable in real time, as the direction of the mobility channels can be switched as shown in Figure 2.6. The switching period itself is short compared to ω^{-1}, and therefore the time-average potential concept is not applicable during this time. To demonstrate the transport of a matter-wave soliton in the dynamically reconfigurable driven lattice in Equation (2.2), we prepare the initial state in the form Equation (2.7) with $a = 0.735$ so that the norm N is matched to that of the exact stationary soliton of the potential V_s [point (c) in Figure 2.4]. We then load it into the 2D lattice driven with the frequency $\omega = 10$ and the driving amplitudes $X_0 = 2.4$, $Y_0 = 0$. At the time $t = 60$ the driving amplitudes are rapidly, but non-instantaneously, switched to the values $X_0 = 0$, $Y_0 = 2.4$, as shown in Figure 2.6 (middle panel). The resulting trajectory of the soliton's center of mass is shown in Figure 2.7(a). In this figure, the trajectory of the soliton is superimposed with the optical lattice potential $V_{\rm OL}(t = 0)$. The trajectory is easily reconfigurable by changing the sequence of switching, as shown in Figure 2.7. Further, more complex "routing" of the soliton along different orthogonal directions in the lattice can be realized, as shown in Figure 2.7 (c). One can see that, according to our assumption, the center-of-mass trajectory consists of slow (compared to ω^{-1}) motion perturbed by small amplitude fast oscillations, $(\eta(t), \xi(t))$ with the driving frequency. Remarkably, by examining the cross-sections of the soliton profile, we observe that the localized state is only weakly affected by these dynamical manipulations [see Figure 2.7(d)], which justifies our soliton-as-particle approach. Further we applied the method described above for the rocking optical lattice potential given in Equation (2.3). We prepare initial state in the form of an exact stationary soliton supported by the potential V_s in Equation(2.23). Figure 2.8 shows complex trajectory of the soliton's center of mass along different orthogonal directions in the dynamically reconfigurable driven "double-well" lattice potential described by Equation (2.3).

2.7 Concluding remarks

In this chapter we have analysed the propertied of fundametal solitons in BECs with attractive interactions in the rocking optical lattices in the framework of mean-field theory using the GP equation. We have found numerically different families of fundamental solitons in the semi-infinite gap of a shallow 2D rocking optical lattices and time averaged effective potentials. Stability of stationary soliton families corresponding to 2D optical lattices was determined using the Vakhitov Kolokolov stability criterion. Our analytical analysis based on variational approximation and effective particle approach showed that the approximate solution is in good agreement with the exact stationary solution far from the band edge. Finally, we have investigated dynamical properties of 2D bright solitons of BEC as effective classic particles in effective potentials. We demonstrated, theoretically and numerically, that time-modulated optical lattices enable realization of clean, controlled transport of matter waves in more than one spatial dimensions. This work opens up a fascinating possibility to realise transport and routing of matter-wavepackets in two-dimensional lattices of more complex spatial structure, as well as in fully three-dimensional trapping geometry.

Chapter 3

Suppression of collapse for BEC with orbital angular momentum

3.1 Introduction

Since the early days of ultracold atomic physics, the phenomena of matter wave collapse, i.e. unrestricted contraction of the Bose-Einstein condensate with attractive interatomic interactions, has been studied both experimentally [47, 54, 62, 68] and theoretically [61, 63–66, 127]. In particular, it has been shown that a dynamically stable BEC can exist both in 3D and 2D (strongly anisotropic, "pancake") harmonic traps, as long as the number of particles in the condensate is below a critical value which depends on the anisotropy of the trap [67]. The initial dynamics of collapsing coherent matter waves under harmonic confinement is well described by the mean-field Gross-Pitaevskii theory, and is analogous to the collapsing light waves in self-focusing optical fibers [128–133]. However, above the critical number of atoms, the condensate wavefunction undergoes rapid growth in peak density, which triggers three-body recombination losses [65, 66]. The analysis of subsequent dissipative dynamics should, in principle, take into consideration the uncondensed thermal fraction of atoms in the trap, which takes it beyond the standard mean-field theory [134]. Naturally, the problem of collapse control and possible suppression in such systems is of a great fundamental and practical importance. Several suggestions have been made on possible mechanisms to arrest the collapse, e.g. exploiting nonlocal interaction [135, 136], or quintic elastic collisions [137–139]. In particular, it has been argued that raising the energy of the condensate through, e.g., addition of an angular momentum (such as a vortex line) may raise the collapse threshold [64, 140]. It has been also predicted [141] in the context of many-body phenomena that the fragmentation of condensate, i.e. macroscopic population of several single-particle states (or "orbitals"), that correspond to different orbital angular momentum (OAM, [142]) eigenstates of the density functional, can lead to a metastable (i.e. long-lived) state of an attractive condensate with overcritical number of atoms. However, such OAM states are vulnerable to the *azimuthal modulational instability* well known in nonlinear optics [143]. The azimuthal instability leads to spatial modulation and break-up of ring-shaped density envelope around vortex line before the filaments collapse [144].

It was further suggested that for vortex-free, anisotropic (e.g. elliptic) two-dimensional condensate clouds [145], carrying angular momentum [146], the collapse might be completely arrested approach. Similar approach was considered [147–149] in the context of collapse of laser beams in a bulk self-focusing medium [127, 150]. It was shown [149] that imprinting a twisted phase front and thereby transferring OAM onto light beams with elliptic cross-section enables dramatic suppression of their collapse. Although the rotating BEC with attractive interaction was studied in the context of vortex formation [151–154], the fundamental role of OAM in the collapse dynamics of vortex-free trapped BECs, remains an open problem. In this chapter, we analyse vortex-free elliptic BEC clouds carrying OAM in *a quasi-two-dimensional radially-symmetric harmonic trap* and *a quasi-two-dimensional rotating elliptic trap.* Within the framework of the mean-field formalism, we show, both analytically and numerically, that for such rotating (spiraling) clouds the onset of collapse can be drastically suppressed well above the typical threshold numbers of trapped atoms.

3.2 Suppression of collapse for BEC with OAM in a quasi 2D radially-symmetric harmonic trap

3.2.1 Model

We consider a BEC with negative scattering length trapped in a quasi-two-dimensional radially symmetric "pancake" trap with a tight transverse (axial) confinement. By using the appropriate dimensionality reduction procedure [48], the mean-field Gross-Pitaevskii model for the condensate wavefunction can be written in the following dimensionless form:

$$i\partial_t\psi + \Delta\psi - w^{-4}r^2\psi + |\psi|^2\psi = 0, \tag{3.1}$$

here $\Delta = \partial_x^2 + \partial_y^2$, and w defines the depth of the radially-symmetric trapping potential with $r^2 = x^2 + y^2$. The dimensionless form is derived by measuring the time in units of $2/\omega_z$, energy in units of $\hbar\omega_z$, and length in units of the transverse harmonic oscillator length $l_z = \sqrt{\hbar/(m\omega_z)}$, where ω_z is the tight trapping frequency, and m is the mass of the trapped atoms. The three-dimensional wavefunction is factorized under the conditions of the tight azimuthal confinement and the two-dimensional wavefunction $\psi(x, y)$ is renormalized so that the interaction strength characterizing the two-body scattering is scaled to unity. In these units the norm of the two-dimensional wavefunction, $N = \int |\psi|^2\, dxdy$, is related to the number of particles in the condensate, $\mathcal{N}$, as follows: $\mathcal{N} = (1/\sqrt{2\pi})(|l_s|\omega_r)/(l_z\omega_z)N$, where l_s is the two-body scattering length and ω_r is the radial trapping frequency.

The only remaining parameter, $w^4 = \omega_z^2/\omega_r^2$, in model Equation (3.1) can be scaled away (effectively $w \to 1$) by introducing new variables: $t' = t/w^2$, $r' = r/w$, and $\psi' = w\psi$, however, we keep it for numerical convenience. This parameter defines the width of the lowest-order *linear* radially symmetric mode, $\psi_{\rm lin} = \exp\left(-r^2/2w^2 - i\mu t\right)$, here the chemical potential is $\mu = 2w^{-2}$.

The radial symmetry of Equation (3.1) implies conservation of OAM:

$$\partial_t M = 0, \quad M = \mathrm{Im}\int \psi^*\left(x\psi_y - y\psi_x\right)\, dxdy, \tag{3.2}$$

in addition to conservation of the normalized number of atoms, N, and the Hamiltonian:

$$\mathcal{H} = \int \left(|\nabla\psi|^2 + w^{-4}r^2|\psi|^2 - |\psi|^4/2\right)\, dxdy. \tag{3.3}$$

Important for the following is the scaling (or "dilation") transformation of Equation (3.1), which allows to obtain exact periodic nonlinear solutions [129, 132, 133]. Namely, for any solution $\psi(x,y,t)$ to Equation (3.1) there exist another solution, $\tilde{\psi}(x,y,t)$, with the spatial scale $s(t)$, evolution variable $z(t)$, and the additional parabolic wavefront curvature defined by $\alpha(t)$ [132, 133]:

$$\tilde{\psi}(x,y,t) = \frac{1}{s}\psi\left(\frac{x}{s},\frac{y}{s},z\right)\exp\left(i\alpha r^2\right), \tag{3.4}$$

provided the following relations are satisfied:

$$\frac{1}{\mu^2}\frac{d^2 s}{dt^2} + s = \frac{1}{s^3}, \quad \frac{dz}{dt} = \frac{1}{s^2}, \quad \alpha = \frac{1}{4s}\frac{ds}{dt}. \tag{3.5}$$

In particular, without the initial phase chirp, $\alpha_0 = 0$ (here and below the subscript 0 indicates initial value at $t = 0$), the solution to Equation (3.5) reads

$$s^2(t) = s_0^2\cos^2\mu t + s_0^{-2}\sin^2\mu t. \tag{3.6}$$

3.2.2 Variational approach

In order to create an anisotropic rotating matter wave that would mimic the collapse-resistant light beam described in [149], a phase twist should be imprinted onto the BEC cloud. A number of techniques of the transfer of OAM from photons to atoms have already been suggested theoretically and demonstrated experimentally [155–157]. Such techniques, in principle, can enable transfer of OAM readily imprinted onto an optical wave by, e.g., combination of cylindrical lenses [158].

Approximate solutions of Equation (3.1) in the form of such nonlinear rotating modes can be derived using the variational method, by way of standard Ritz minimization procedure [146, 153, 154, 159] with the Lagrangian $\mathcal{L} = \int \frac{i}{2}\left(\psi^*\frac{\partial\psi}{\partial t} - \psi\frac{\partial\psi^*}{\partial t}\right)dxdy - \mathcal{H}$. We use the ansatz suggested for the elliptic spiraling soliton (i.e. a nonlinear self-focused state) in [147–149, 153, 154]:

$$\psi(x,y,t) = A(t)\,G\left[X/b(t)\right]\,G\left[Y/c(t)\right]\,\exp\left(i\chi\right), \tag{3.7}$$

with the Gaussian envelope $G(\xi) = \exp(-\xi^2/2)$ and phase $\chi = B(t)X^2 + \Theta(t)XY + C(t)Y^2 + \varphi(t)$, in the rotating frame $X = x\cos\theta(t) + y\sin\theta(t)$ and $Y = -x\sin\theta(t) + y\cos\theta(t)$. It is instructive to represent the integrals of motion Equations (3.2), (3.3) in laboratory frame (x,y,t) expressed in terms of key variational parameters and the number of particles, $N = \pi A^2 bc$. The OAM is

$$M = \frac{N}{4}\frac{(b^2-c^2)^2}{b^2+c^2}\frac{d\theta}{dt}, \tag{3.8}$$

and the Hamiltonian is similar to that of a classical particle with "effective" mass $N/4$ in a two-dimensional potential

$$H = \frac{N}{8}\left(\frac{db}{dt}\right)^2 + \frac{N}{8}\left(\frac{dc}{dt}\right)^2 + \frac{M}{2}\frac{d\theta}{dt} + \frac{N}{2}\left(\frac{1}{c^2} + \frac{1}{b^2} + \frac{b^2+c^2}{w^4}\right) - \frac{N^2}{4\pi bc}, \tag{3.9}$$

where the last nonlinear term ($\sim N^2$) is the interaction term.

Similar to [149], it is convenient to introduce the spatial scale $a(t)$, $a^2 = (b^2+c^2)/2$, and the ellipticity parameter $\epsilon(t) = \tan^{-1}(c/b)$ with $0 < \epsilon < \pi/2$, then $b = \sqrt{2}\,a\cos\epsilon$ and

$c = \sqrt{2}\, a \sin\epsilon$. The variational equations take the following form:

$$\frac{dn}{dt} = 0, \qquad n = A^2 a^2 \sin 2\epsilon, \tag{3.10}$$

$$\frac{d\sigma}{dt} = 0, \qquad \sigma = \Theta a^2 \cos 2\epsilon, \quad \Theta = \frac{1}{2}\frac{d\theta}{dt}\cos 2\epsilon, \tag{3.11}$$

$$\frac{dK}{dt} = 0, \qquad K = \frac{a^4}{2}\left(\frac{d\epsilon}{dt}\right)^2 + \frac{4 - n\sin 2\epsilon}{2\sin^2 2\epsilon} + \frac{2\sigma^2}{\cos^2 2\epsilon}, \tag{3.12}$$

$$\frac{dh}{dt} = 0, \qquad h = \frac{1}{2}\left(\frac{da}{dt}\right)^2 + \frac{K}{a^2} + \frac{2a^2}{w^4}, \tag{3.13}$$

with rescaled particle number $n = N/\pi$, normalized (per particle) OAM $\sigma = M/N$, normalized Hamiltonian $h = 2\mathcal{H}/N$, and the Ermakov integral of motion K [146–149].

The only difference with the nonlinear system derived in [149] for the same set of parameters is the additional term $2w^{-4}a^2$ in the expression for h in Equation (3.13) which is due to the presence of trapping potential. This term modifies the diffraction and changes the dynamics of spiraling elliptic mode dramatically, compared to nonlinear localized state in a trap-free situation [149]. To demonstrate this difference, we derive the following solution to Equation (3.13) for a particular choice of initial conditions, $da_0/dt = d\epsilon_0/dt = 0$:

$$a^2(t) = a_0^2 \cos^2 \mu t + \frac{K w^4}{2a_0^2}\sin^2 \mu t. \tag{3.14}$$

Here the oscillation frequency coincides with the chemical potential of linear modes above, $\mu = 2w^{-2}$. The analysis of Equation (3.14) shows that for $K > 0$ there is no collapse and the BEC cloud in the trap persists as a stable rotating and oscillating mode, while for $K \leq 0$ the collapse occurs at a finite time (see also [146]):

$$t_{\text{collapse}} = \frac{w^2}{2}\tan^{-1}\left(\frac{a_0^2}{w^2}\sqrt{\frac{2}{|K|}}\right). \tag{3.15}$$

3.2.3 Stationary rotating nonlinear modes

The stationary solution with $a(t) = a_0$ is obtained from Equation (3.14) for a particular choice of the integral of motion $K = 2a_0^4/w^4$. More generally, the stationary solution rotating with constant velocity $d\theta/dt = \omega$ is obtained from Equations (3.12), (3.13) by setting derivatives to zero, $da/dt = d\epsilon/dt = 0$, which require $B = C = 0$. As a result, we obtain a family of stationary rotating nonlinear modes with *two parameters*: the number of particles n and the OAM σ. It is more convenient, however, to derive this family in terms of parameters n and ϵ as follows. For a given scale factor, w, we choose the number of particles n and the envelope ellipticity ϵ_s (here the subscript s indicates stationary solution), and subsequently derive the mode width a_s,

$$a_s = \frac{w}{\sin 2\epsilon_s}\left[1 - \frac{n}{8}\sin 2\epsilon_s\left(1 + \sin^2 2\epsilon_s\right)\right]^{1/4}, \tag{3.16}$$

the amplitude $A_s^2 = n/a_s^2 \sin 2\epsilon_s$, the OAM

$$\sigma_s = \pm\cot^2 2\epsilon_s\left[1 - \frac{n}{8}\sin 2\epsilon_s\right]^{1/2}, \tag{3.17}$$

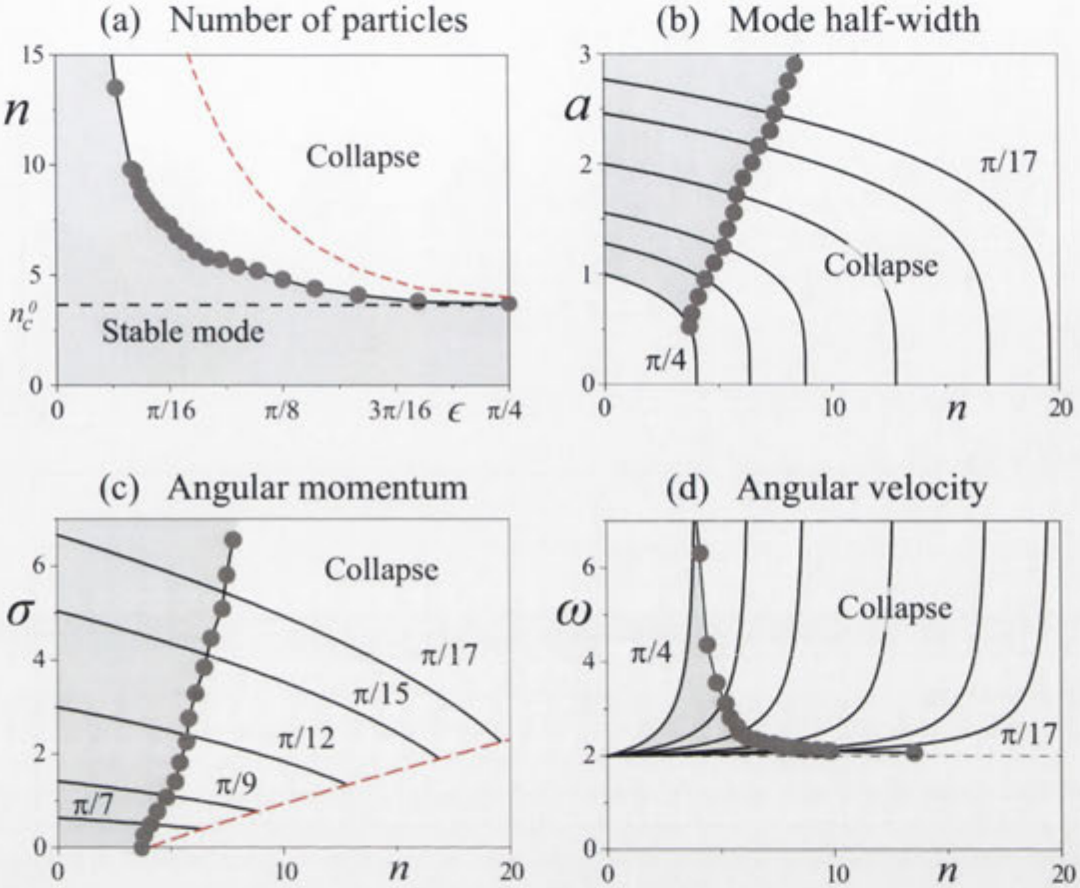

Figure 3.1: (a) Existence and stability diagram for the 2D rotating elliptic matter waves; (b-d) Family of stationary nonlinear rotating modes predicted by the variational approach sampled at fixed values of ellipticity ϵ_s (solid lines). The region of stability against collapse identified via dynamical simulations of model Equation (3.1) is shaded; the large size of circle markers reflects final accuracy of numerically obtained boundary values. Corresponding boundary of mode existence and stability region predicted by variational approach is marked by (red) dashed line.

the rotation velocity $\omega_s = 2\sigma_s/a_s^2 \cos^2 2\epsilon_s$, and finally the phase twist $\Theta_s = (\omega_s/2)\cos 2\epsilon_s$. The signs $\pm$ in Equation (3.17) correspond to two opposite directions of rotation. The family of nonlinear stationary modes described by Equations (3.16) and (3.17) is presented in Figures 3.1(b-d) in the form of the dependencies $a_s(n)$, $\sigma_s(n)$, and $\omega_s(n)$ for several values of ellipticity ϵ_s.

It is instructive to compare such nonlinear elliptic modes with their linear counterparts. The linear Equation (3.1), with the nonlinear interaction term formally set to zero, corresponds to the limit $n \to 0$ in Equations (3.16) and (3.17). Interestingly, this limit allows to recover an *exact linear solution* in the form of a stationary elliptic rotating mode. To prove it, we directly substitute Equation (3.7) into (3.1) (without the nonlinear term) and derive the system of coupled first-order differential equations for the parameters of the trial function (3.7). We are interested here in the mode with stationary profile, $\frac{d}{dt}\{A, b, c\} = 0$, in the frame rotating with constant angular velocity $d\theta/dt = \omega$. Denoting such solution by the subscript l, we obtain $B_l = C_l = 0$, $a_l \sin 2\epsilon_l = w$, and $\sigma_l = \pm\cot^2 2\epsilon_l$,

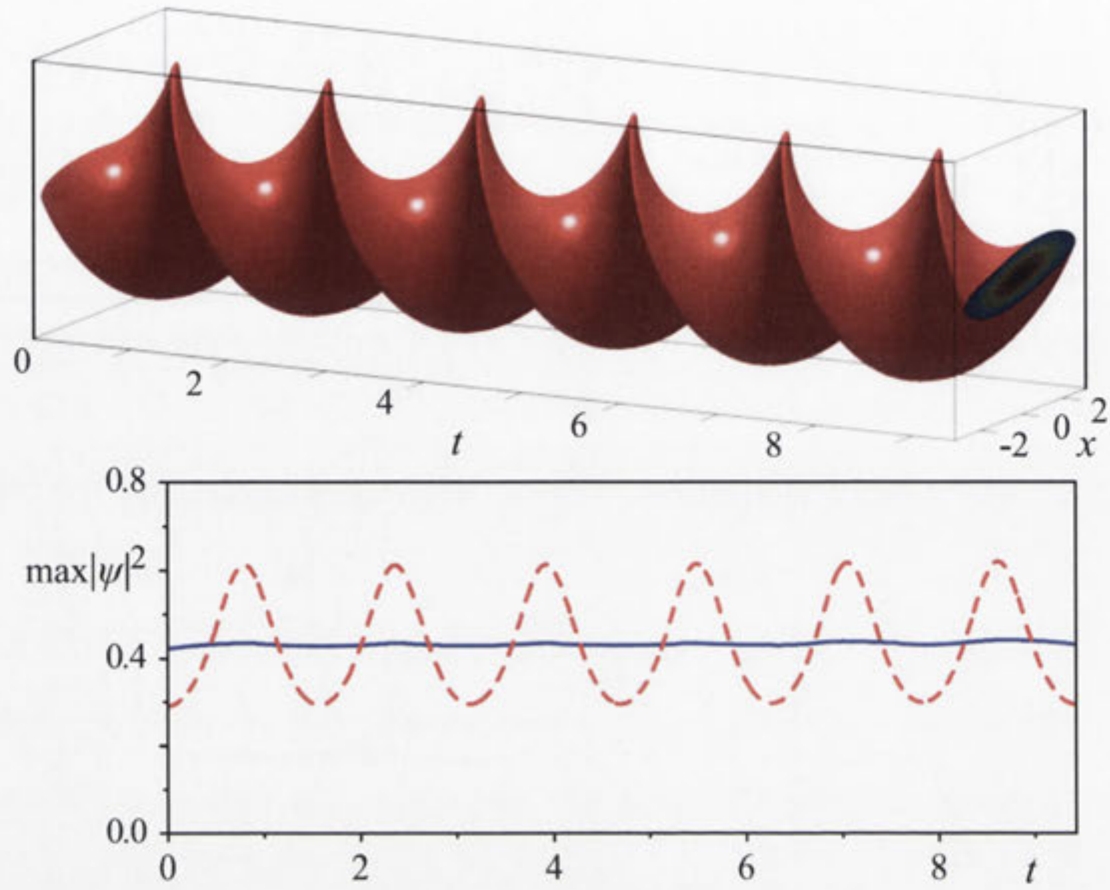

Figure 3.2: Stable dynamics of stationary rotating elliptic matter waves with $n = 1$ and $\epsilon_s = \pi/15$. Shown are (top) surface of equal density at half the peak level, and (bottom) peak density, $\max|\psi|^2$. Dashed line shows the regular oscillations of the peak density of the same state excited by initial "stretching" $s_0 = 1.2$ described by Equation (3.6).

which also follow from equations (3.16, 3.17) with $n = 0$. The chemical potential does not differ from that of the fundamental mode above, $d\varphi_l/dt = -2w^{-2} = -\mu$.

A striking similarity between linear and nonlinear modes is that in both cases there is a continuous family of solutions with different profiles that are stationary in the rotating reference frame (defined by ϵ_l and ϵ_s, respectively). The difference is that, while the rotation velocity of nonlinear mode ω_s strongly depends on the ellipticity ϵ_s and OAM σ_s, the analogous parameter for linear mode, $|\omega_l| = \mu$, is independent of its OAM σ_l.

3.2.4 Collapse threshold and dynamics

As discussed above, the condition for the stability of the nonlinear rotating mode against collapse requires $K > 0$ and the threshold, $K = 0$, defines the mode cut-off, $a_s \to 0$, which is also obvious from Equation (3.16). Namely, for a given ellipticity ϵ_s, the collapse occurs for $n \geq n_c$ with critical number of particles:

$$n_c = \frac{8}{\sin 2\epsilon_s \left(1 + \sin^2 2\epsilon_s\right)}. \tag{3.18}$$

This threshold condition defines a stability boundary in the existence domain of the stationary modes shown in Figure 3.1. In the limit $\epsilon \equiv \pi/4$ and $\sigma \equiv 0$, corresponding to the fundamental radially-symmetric mode, Equations (3.10-3.13) yield well known results. Namely, the collapse threshold defined by Equation (3.18) gives the critical number $n_c^0 = 4$, or $N_c = 4\pi \simeq 12.57$ [160], which is slightly higher than the exact number $N_c = 11.69$ [161]. One can see that the variational theory predicts significant departure from this collapse threshold for elliptical stationary states. As the degree of anisotropy grows, $\epsilon \to 0$, the critical number increases well above the value of $n_c^0 = 4$, as see in Figure 3.1(a).

We test variational predictions by direct numerical solution of the dynamical Equation (3.1) with the split-step wave propagation method based on the fast Fourier transform. As an initial condition we choose the variational trial function with the parameters corresponding to one of the predicted stationary states with a given ellipticity. We note that, while we aim to determine the onset of collapse, it is not our intention to simulate the dynamics of collapsing wavefunction, therefore the simulations are performed on a fairly rough spatial grid (1024x1024) and stopped once the collapse has commenced, i.e., once the spatial extent of the condensate wavefunction becomes comparable with the discretization scale of the numerical grid (see Appendix A). For stable solutions, we simulated the propagation for up to $t = 200$ to make sure that no indication of delayed collapse is evident.

Our results are summarized in Figure 3.1. One can see that the numerical results on the collapse threshold qualitatively agree with the variational predictions. Indeed, the collapse is significantly suppressed for the elliptical rotating states with the normalized number of particles well above the fundamental threshold $n_s = 4$. For relatively low atom numbers the variational solution is remarkably close to the true stationary state and thus serves as an excellent initial condition for demonstration of the stable dynamics. Stable dynamics of the stationary rotating state below the collapse threshold is shown in Figure 3.2 for $n = 1$ and $\epsilon = \pi/15$.

Furthermore, below the critical value the variational theory predicts that the stationary states are dynamically stable. An important observation regarding their dynamics is that, if we introduce the new variables $s(t) = a(t)/a_s$ and $s_0 = a_0/a_s$ into Equation (3.14), together with the expression for the Ermakov integral, $K = K_s = 2a_s^4/w^4$, we recover Equation (3.6). Therefore, although variational ansatz (3.7) is approximate, the description Equation (3.14) of oscillations near stationary solution a_s is exact. Indeed, the numerical evolution of the peak density of initially "stretched" mode in Figure3.2 (dashed line) displays regular oscillations described by Equations (3.6) and (3.14). Such periodic variation of the spatial scale was also obtained by variational method in [146]. As expected, Equation (3.14) with $K = 2 - n/2$ also describes the stable dynamics of the fundamental (ground state) radially-symmetric mode, which for $n < n_c$ exhibits oscillations around stationary state. Remarkably, in all these cases the frequency of oscillations, $\mu = 2w^{-2}$, is independent of the number of particles n.

For larger number of atoms, the variational solution no longer correctly predicts the shape of the stationary rotating mode, although still correctly predicts the stability of the condensate against collapse. Such nonstationary stable dynamics can be seen in Figure 3.3(top panel), where it is clearly seen that the collapse is suppressed. Finally, above the certain numerically determined threshold (the boundary is marked by grey circles in Figure 3.1), the matter wave clearly exhibits a strong collapse in Figure 3.3(middle panel), which is characterized by the unlimited growth of the peak density, as shown in Figure

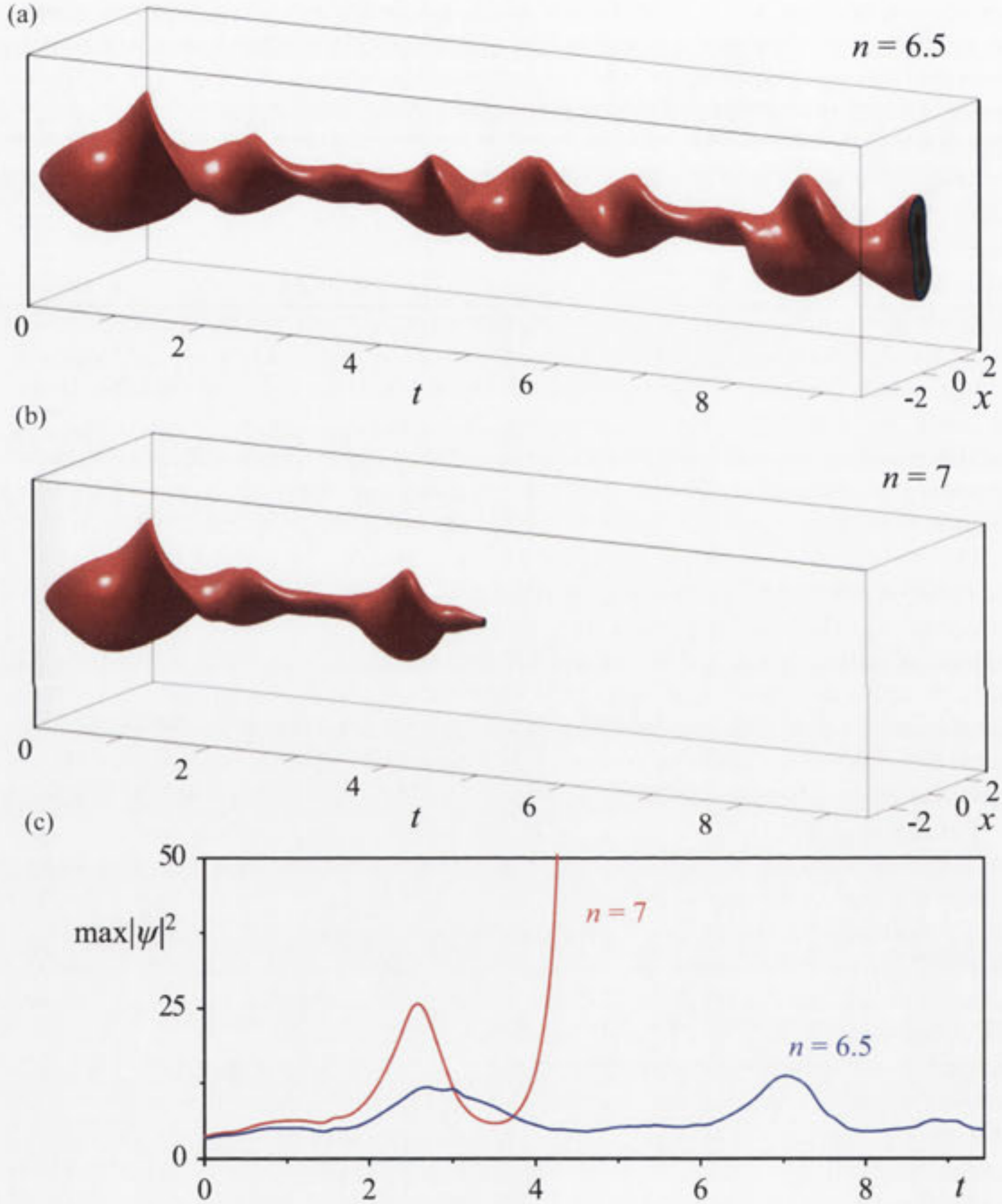

Figure 3.3: (a) Non-stationary and (b) unstable dynamics of rotating elliptic matter waves near and above the collapse threshold, respectively. Shown are (a,b) surface of half-peak density approaching radial delta-function distribution at the final point of evolution, and (c) peak density.

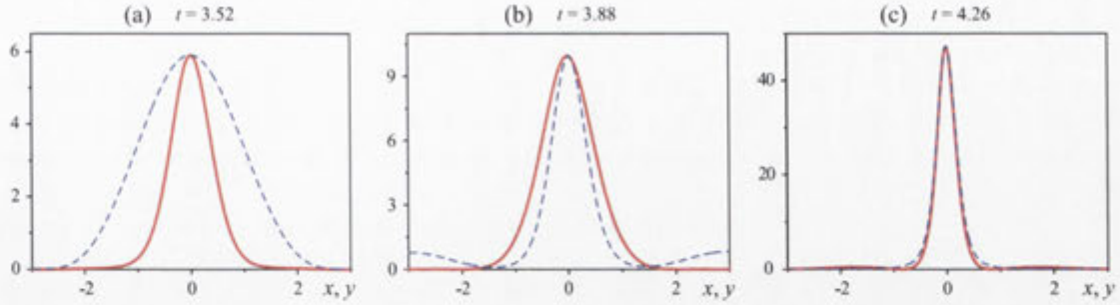

Figure 3.4: Cross-sections along the x- (solid) and y-dimension (dashed) of the density of collapsing matter wave with $n = 7$ at different points in temporal evolution in 3.3 showing convergence to a radially symmetric shape.

3.3(bottom panel).

It is interesting to note that, even for an initially strongly anisotropic condensate cloud, the central region of the condensate becomes radially symmetric as seen in Figure 3.4, displaying the self-similar collapse dynamic well described in the context of radially symmetric geometries of self-focusing nonlinear optical beams [150]. The formation of similar radially-symmetric Townes profile [162] of initially anisotropic collapsing laser beam was observed experimentally in [163].

To stress the role of OAM in suppression of collapse, here we briefly examine the effect of an elliptic deformation without a phase twist [145, 146], $\Theta \equiv 0$, i.e. with zero OAM, $\sigma \equiv 0$. The dynamics is described by variational Equations (3.12) and (3.14), with the collapse threshold defined by the condition $K = 0$, as above. Therefore, variational approach predicts that collapse is suppressed if the number of particles is below the critical value, $n_c = 4/\sin 2\epsilon$, which is up to a factor of two lower than that for the rotating modes in Equation (3.18).

However, the direct numerical simulations show that the actual collapse threshold is much lower than that of rotating modes with nonzero OAM. For example, we found this threshold to be $n_c \simeq 4.7$ for initial ellipticity $\epsilon_0 = \pi/15$, which is much lower than $n_c = 6.8$ for rotating states in Figures 3.2, 3.3, and it is much closer to that of the ground radially-symmetric state, $n_c^0 = 4$. The apparent reason for greater discrepancy with variational predictions is that, in contrast to persistent rotation of modes supported by conservation of OAM, the non-stationary elliptic modes with zero OAM are subject to strong oscillations decaying into a complex pattern with the appearance of radially-symmetric collapsing spike, as in Figure 3.4. This decay is not captured by our variational approach.

3.3 Suppression of collapse for BEC with OAM in a quasi 2D rotating elliptic trap

The elliptic BEC clouds can be naturally obtained by confinement in anisotropic traps. Here we reveal that, similar to elliptic spiraling optical beams, the collapse can be suppressed for matter waves in an elliptic rotating harmonic trap.

3.3.1 Model

Taking into account appropriate dimensionality reduction procedure, we can write the mean-field Gross-Pitaevski equation for attractive BEC in parabolic trap with elliptic profile (semi-axes ω_x and ω_y), rotating with angular velocity ω, in the following dimensionless form,

$$i\partial_t\psi + \Delta\psi - \left(\omega_x^2\xi^2 + \omega_y^2\eta^2\right)\psi + |\psi|^2\psi = 0, \tag{3.19}$$

where $\Delta = \partial_x^2 + \partial_y^2$, $\xi = x\cos\omega t + y\sin\omega t$ and $\eta = -x\sin\omega t + y\cos\omega t$. The number of parameters in Equation (3.19) can be reduced by removing the spatial scale w using $t = w^2t'^2$, $r = \sqrt{x^2+y^2} = wr'$, $\omega = w\omega'$, $\psi = w^{-1}\psi'$, and introducing ellipticity parameter $\lambda = (\omega_y^2 - \omega_x^2)/(\omega_x^2 + \omega_y^2)$ with $\omega_{x,y}^2 = (1 \mp \lambda)/w^4$. In the following we use an equivalent transform in Equation (3.19), $\omega_{x,y}^2 \to (1 \mp \lambda)$, and, without loss of generality, choose the trap elongated in x-direction, $\omega_y > \omega_x$ and $0 < \lambda < 1$. Note that $\lambda = 0$ corresponds to the case of radially symmetric trap considered above.

3.3.2 Variational approach

Variational solutions are derived using the standard Ritz minimization procedure with the Lagrangian

$$\mathcal{L} = \int \frac{\mathrm{i}}{2}\left(\psi^*\frac{\partial\psi}{\partial t} - \psi\frac{\partial\psi^*}{\partial t}\right)\mathrm{d}\mathbf{r} - \mathcal{H}, \tag{3.20}$$

and Hamiltonian

$$\mathcal{H} = \int \left[|\nabla\psi|^2 + \left(\omega_x\xi^2 + \omega_y\eta^2\right)|\psi|^2 - \tfrac{1}{2}|\psi|^4\right]\mathrm{d}\mathbf{r}. \tag{3.21}$$

We introduce a trial function,

$$\psi(x,y,t) = A(t)\,G\left(X/b(t)\right)\,G\left(Y/c(t)\right)\,\exp\left(i\chi\right), \tag{3.22}$$

with the Gaussian envelope $G(t) = \exp(-t^2/2)$ and phase $\chi = B(t)X^2 + \Theta(t)XY + C(t)Y^2 + \varphi(t)$, in the rotating frame $X = x\cos\theta(t) + y\sin\theta(t)$ and $Y = -x\sin\theta(t) + y\cos\theta(t)$. Similar to [149], we introduce the spatial scale $a(z)$, $a^2 = (b^2+c^2)/2$, and the ellipticity parameter $\epsilon(z) = \tan^{-1}(c/b)$, then $b = \sqrt{2}\,a\cos\epsilon$ and $c = \sqrt{2}\,a\sin\epsilon$, $0 < \epsilon < \pi/2$.

For a general dynamic solution, the mode rotation rate is different from that of the trap, $\dot\theta \neq \omega$, and the system is dissipative:

$$\begin{aligned} \dot h &= \omega\dot\sigma, \quad \dot\sigma = -2\lambda a^2\cos 2\epsilon\,\sin(2\theta - 2\omega t), \\ h &= \frac{1}{2}\dot a^2 + \frac{1}{2}a^2\left(\dot\epsilon^2 + \dot\theta^2\cos^2 2\epsilon\right) + \frac{4 - n\sin 2\epsilon}{2a^2\sin^2 2\epsilon} + 2a^2\left(1 - \lambda\cos 2\epsilon\,\cos(2\theta - 2\omega t)\right) \end{aligned} \tag{3.23}$$

here the overdot indicates time derivative. The Hamiltonian $h = 2\mathcal{H}/N$, is normalized here by number of particle $N \equiv \int|\psi|^2 d\mathbf{r} = \pi A^2a^2\sin 2\epsilon$, which is the only conserved quantity in the system, $\dot n = 0$ and $n = N/\pi$. We also use normalized (average per particle) orbital angular momentum (OAM) $\sigma \equiv M/N = a^2\Theta\cos 2\epsilon$ with $\Theta = \frac{1}{2}\dot\theta\ \cos 2\epsilon$, here $M \equiv Im\int\psi^*(x\partial_x\psi - y\partial_x\psi)d\mathbf{r}$.

The system does not seem to have other integrals of motion, thus the numerical solu-

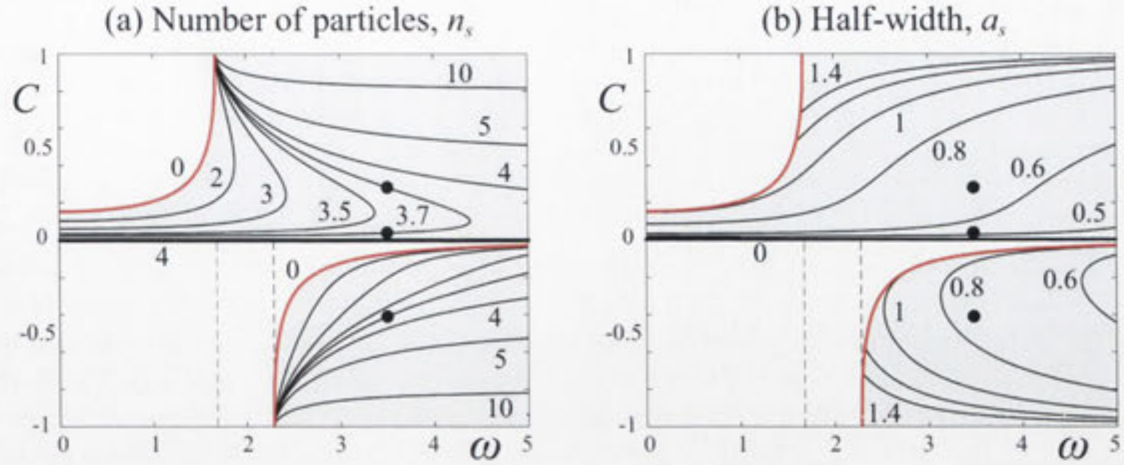

Figure 3.5: Contour lines of (a) number of particles, n_s in Equation (3.26), and (b) half-width, a_s in Equation (3.27). Here $C \equiv \cos 2\epsilon_s$ and $\lambda = 0.3$; the numbers show corresponding contour levels. Red lines: linear modes with $n_s = 0$. Dots: an example of a tri-stable solution (C_1=0.283, C_2=0.038, C_3=-0.41) with $\omega = 3.5$ and $n = 3.7$.

tion of the evolution equations is in order:

$$\begin{aligned}
\frac{d^2\theta}{dt^2} &= 2\dot{\theta}\left(2\dot{\epsilon}\tan 2\epsilon - \dot{a}/a\right) - 4\lambda\sin(2\theta - 2\omega t)/\cos 2\epsilon \\
\frac{d^2\epsilon}{dt^2} &= -2\frac{\dot{a}}{a}\dot{\epsilon} - \dot{\theta}^2\sin 4\epsilon + \frac{8 - n\sin 2\epsilon}{a^4\sin^3 2\epsilon}\cos 2\epsilon - 4\lambda\sin 2\epsilon\,\cos(2\theta - 2\omega t), \\
\frac{d^2a}{dt^2} &= a\left(\dot{\epsilon}^2 + \dot{\theta}^2\cos^2 2\epsilon\right) + \frac{4 - n\sin 2\epsilon}{a^3\sin^2 2\epsilon} - 4a\left(1 - \lambda\cos 2\epsilon\,\cos(2\theta - 2\omega t)\right)
\end{aligned} \tag{3.24}$$

3.3.3 Stationary rotating nonlinear mode

It seems natural to choose the BEC co-rotating with the trap, $\theta(t) = \omega t$, yet this choice does not seem to follow as a particular solution of the system above. Nevertheless, we can force the condition $\dot{\theta} = \omega$ by choice of trial function. The system becomes conservative, $\{\dot{h}, \dot{\sigma}\} = 0$, with $\Theta = \frac{1}{2}\omega\cos 2\epsilon$ and $\sigma = \frac{1}{2}\omega a^2\cos^2 2\epsilon$. The later implies $d(a\cos 2\epsilon)/dt = 0$ and Equation (3.24) is satisfied, $\ddot{\theta} = 0$, because $\dot{a}/a = 2\dot{\epsilon}\tan 2\epsilon$, but

$$\begin{aligned}
\frac{d^2\epsilon}{dt^2} &= -2\frac{\dot{a}}{a}\dot{\epsilon} - \omega^2\sin 4\epsilon + \frac{8 - n\sin 2\epsilon}{a^4\sin^3 2\epsilon}\cos 2\epsilon - 4\lambda\sin 2\epsilon, \\
\frac{d^2a}{dt^2} &= a\left(\dot{\epsilon}^2 + \omega^2\cos^2 2\epsilon\right) + \frac{4 - n\sin 2\epsilon}{a^3\sin^2 2\epsilon} - 4a\left(1 - \lambda\cos 2\epsilon\right), \\
h &= \tfrac{1}{2}\dot{a}^2 + \tfrac{1}{2}a^2\left(\dot{\epsilon}^2 + \omega^2\cos^2 2\epsilon\right) + \frac{4 - n\sin 2\epsilon}{2a^2\sin^2 2\epsilon} + 2a^2\left(1 + \lambda\cos 2\epsilon\right)
\end{aligned} \tag{3.25}$$

Stationary rotating nonlinear mode is given by the solution to the system of Equations (3.25) with all derivatives set to zero, except the rotation rate $\dot{\theta} = \omega$. For given parameters of the trap, λ and ω, we obtain the family of nonlinear modes parameterized by the number of particles n. It is more convenient, however, to express this family versus ellipticity parameter ϵ_s:

$$n_s = \frac{8}{\sin 2\epsilon_s} \frac{(\omega^2-4)\cos 2\epsilon_s + 2\lambda(1+\cos^2 2\epsilon_s)}{\omega^2 \cos 2\epsilon_s (1+\sin^2 2\epsilon_s) + 4(\lambda - \cos 2\epsilon_s)}, \quad (3.26)$$

$$a_s^4 = \frac{4}{\sin 2\epsilon_s} \frac{\cot 2\epsilon_s}{\omega^2 \cos 2\epsilon_s (1+\sin^2 2\epsilon_s) + 4(\lambda - \cos 2\epsilon_s)}, \quad (3.27)$$

and subsequently derive all other parameters, $A_s^2 = n_s/a_s^2 \sin 2\epsilon_s$, $\Theta_s = \frac{1}{2}\omega \cos 2\epsilon_s$ and $\sigma_s = \frac{1}{2}\omega a_s^2 \cos^2 2\epsilon_s$; here and below the subscript s indicates a stationary mode. The family of stationary nonlinear modes described by Equations (3.25) and (3.26) is presented in Figures 3.5(a-b) in the form of contour lines as dependencies $n_s(\omega, C)$ and $a_s(\omega, C)$. Here $C = \cos 2\epsilon_s$ defines the change of ellipticity parameter values.

In the limit $n_s \to 0$ in Equation (3.26) we recover the exact solution for linear mode, which does not exist if the rotation frequency falls into the gap,

$$2\sqrt{1-\lambda} < \omega_{\text{gap}} < 2\sqrt{1+\lambda}. \quad (3.28)$$

It is interesting to note that for angular velocities rates below critical value $\omega < 2\sqrt{1-\lambda}$, the elliptic mode is co-aligned with the trap, $\epsilon_{\text{lin}} = \epsilon_- < \pi/4$, and for supercritical rotation with $\omega > 2\sqrt{1+\lambda}$ the mode is oriented perpendicular to the trap, $\epsilon_{\text{lin}} = \epsilon_+ > \pi/4$, here $\cos 2\epsilon_\pm = p \pm \sqrt{p^2-1}$ with $p = (1-\omega^2/4)/\lambda$. The critical rotation requires infinite eccentricity, $\epsilon_+ \to 0$ and $\epsilon_- \to \pi/2$, and such "explosion" of the wave-function was observed in experiment.

A continuous family of solutions with different profiles for both linear and nonlinear modes are stationary in the rotating frame of elliptic harmonic trap. However, an exsistence of elliptic nonlinear modes does not depend on rotation frequency, which is defined by ellipticity parameter of the trap λ in Equation (3.28). Moreover, for certain number of particles nonlinear modes exsist in a bistable and tri-stable solution forms (see Figure 3.5-3.7).

3.3.4 Variational and numerical stability analysis

To define stability of the nonlinear rotating modes against collapse, we substitute the family of stationary solutions into the system of coupled evolution Equations (3.24). The system is non integrable, therefore, to study the collapse, one can resort to numerical simulations, or the linear stability analysis.

Within our variational approach, we develop the following linear stability analysis. We introduce small perturbations to the nonlinear mode with index "s" and denote them with subscript "1", e.g. $\theta(t) = \omega t + \theta_1(t)$, $a(t) = a_s + a_1(t)$, and $\epsilon(t) = \epsilon_s + \epsilon_1(t)$. Further, we expand Equations (3.24) into series and keep only linear terms in the expansions. Then we will have the following coupled linear system of equations for θ_1, a_1 and ϵ_1:

$$\begin{aligned}
\frac{d^2\theta_1}{dt^2} &= 4\omega \tan 2\epsilon_s \dot{\epsilon}_1 - 2\omega \dot{a}_1 + \frac{8\lambda}{\cos 2\epsilon_s}\theta_1, \\
\frac{d^2\epsilon_1}{dt^2} &= -2\omega \sin 4\epsilon_s \dot{\theta}_1 + \mathcal{C}_1\epsilon_1 + \mathcal{C}_2 a_1, \\
\frac{d^2 a_1}{dt^2} &= 2\omega \cos^2 2\epsilon \dot{\theta}_1 + \mathcal{C}_2\epsilon_1 + 4(-4 + 4\lambda \cos 2\epsilon_s + \omega^2 \cos^2 2\epsilon_s) a_1,
\end{aligned} \quad (3.29)$$

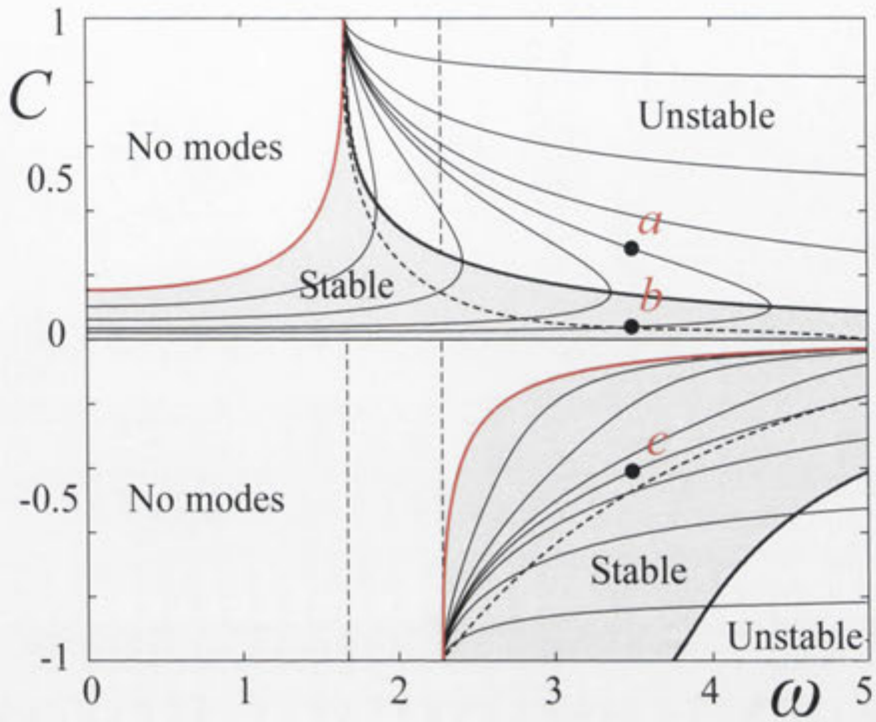

Figure 3.6: Threshold between stable and unstable nonlinear rotating modes predicted by linear stability analysis (black solid line) and by numerical simulations (dashed line) depicted on contour lines of number of particles, n_s.

where $\mathcal{C}_1$ and $\mathcal{C}_2$ are analitically derived coefficients in terms of stationary solution and elliptic trap parameters as follows,

$$\begin{aligned}\mathcal{C}_1 &= -\frac{1}{\cos 2\epsilon_s \sin^2 2\epsilon_s}\left((12-5\omega^2)\cos 2\epsilon_s - 4\lambda\cos 4\epsilon_s + 4\cos 6\epsilon_s\right)\\ &\quad -\frac{1}{\cos 2\epsilon_s \sin^2 2\epsilon_s}\left(2\lambda(-7+\cos 8\epsilon_s) + \omega^2\cos 10\epsilon_s\right),\\ \mathcal{C}_2 &= -8(2\lambda + \omega^2\cos 2\epsilon_s)\sin 2\epsilon.\end{aligned}$$

The coefficients of the coupled system of equations can be estimated numerically. The condition for the stability of the nonlinear rotating mode against collapse requires solutions for parameters θ_1, ϵ_1 and a_1 in the system of Equations (3.29) to have oscillating character, while exponential decay of these parameters correspond to unstable modes. This way we can recover the parameter domain, where collapse threshold is located (see Figure 3.6). Furthermore, the stability region of nonlinear rotating modes can be estimated by numerical simulations solving model Equation (3.19) directly with substituting into it the family of stationary solutions obtained by variational approach. Figure 3.6 shows that numerically calculated stability region is narrow comparing with variational stability region and variational analysis agree with numerical simulations only qualitatively . However, real picture of obtaining stability region of nonlinear rotating modes requires more complex numerical analysis. Moreover, nonlinear rotating modes change their shape for small number of atoms and generate pairs of vortices for large number of atoms in the elliptic trap. As an example we have simulated the model Equation (3.19)

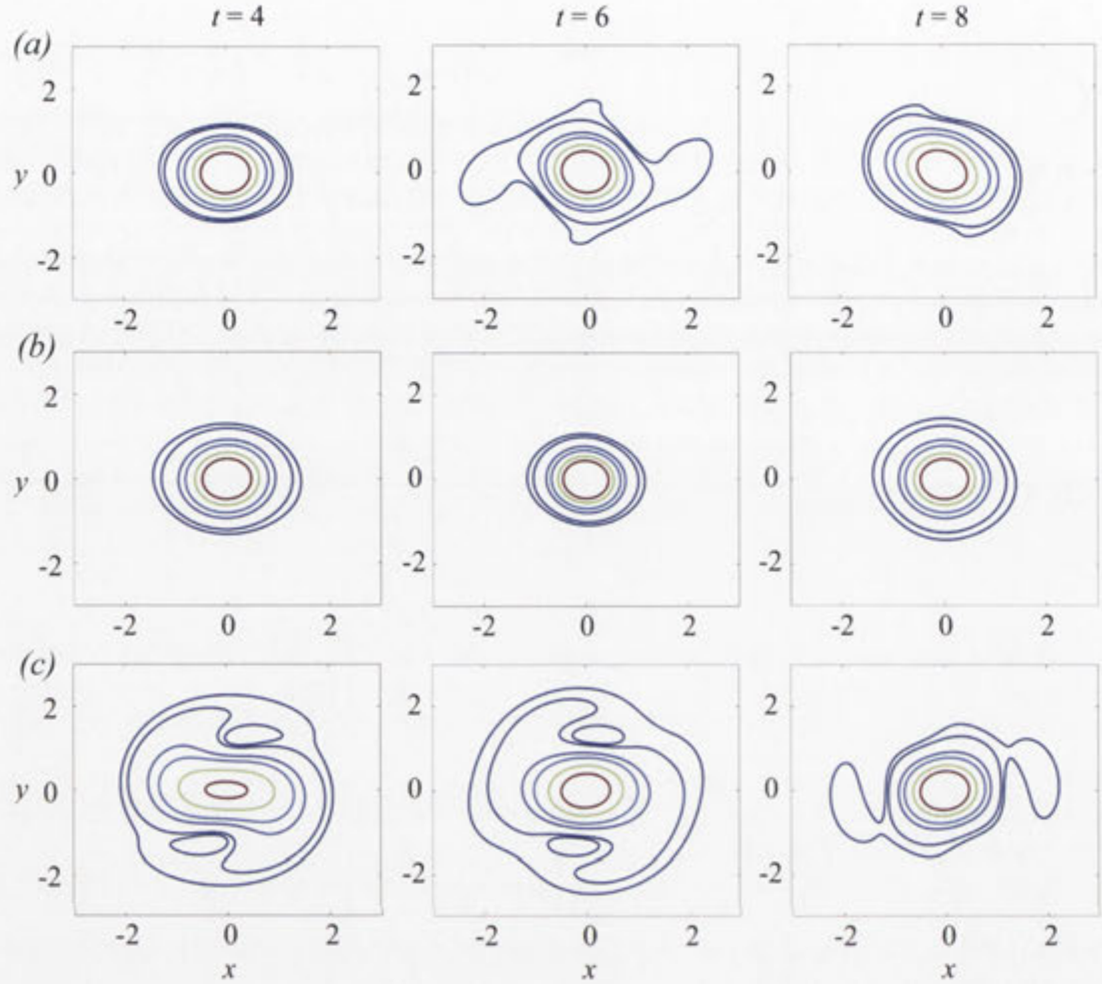

Figure 3.7: Density profiles of nonlinear elliptic rotating modes as indicated by dots in Figure 3.6. There are six contour lines in (a-c) at the levels $(0.001, 0.005, 0.01, 0.05, 0.1, 0.5)|\psi|^2$.

with a tri-stable solution as indicated in Figure 3.5. Figure 3.7 shows profile changes (a-f) and generated pair of vortices (g-i) of a tri-stable solution at times: $t = 4$, $t = 6$ and $t = 8$. The profiles in Figure 3.7 depart significantly from our assumption of elliptic mode. We conclude that the adopted variational approach is unable to describe the collapse dynamics adequately. Therefore, such analysis will require more elaborate anzats and direct numerical experiments.

3.4 Concluding remarks

In this chapter we have explored theoretically the influence of an orbital angular momentum on the dynamics and suppression of collapse of trapped matter waves with attractive inter-atomic interaction. Elliptically shaped spiraling clouds of ultracold atoms supported by radially-symmetric harmonic trap allow for a collapse-free dynamically stable evolution of matter waves with the number of particles greatly exceeding the threshold for radial modes. To achieve the suppression of collapse, one needs to increase ellipticity of the mode and its rotation (spiraling) velocity, by transferring orbital angular momentum to the matter wave, e.g. imprinting a twisted phase front onto an elliptic BEC cloud.

We have also explored spiraling clouds of ultracold atoms supported by elliptic harmonic trap. Our theoretical analysis show that nonlinear rotating modes supported by rotating elliptic trap can have bistable and tri-stable solutions oriented along the trap and perpendicular to the trap. Stability of these modes is calculated analytically using linear stability analysis and numerically solving the model equations. Our numerical results has qualitative agreement with analytical approach. However, variational analysis used in our work fails to describe system quantitatively with all its aspects. To achieve more precise results, one needs to study the system with complex numerical approach, which is our further plan to explore. Due to the formal similarity between the behavior of the coherent matter and light waves, the results could also be readily applied to the dynamics of elliptic "spiraling" modes of nonlinear optical waveguides [129–133].

Chapter 4

Dissipative solitons and vortices in polariton Bose-Einstein condensates

4.1 Introduction

Since the first observation of spontaneous exciton-polariton condensation in a microcavity [5], significant effort in this vigorous field has been directed towards understanding the properties of superfluid flow in the novel nonequilibrium polariton superfluid [7, 73, 74, 164]. Recently, considerable attention was drawn to the controlled creation of spatially localized collective excitations of the exciton-polariton Bose-Einstein condensate. Most notably, moving bright solitons have been predicted [165] and observed in a pioneering proof-of-principle experiment [166]. The properties of polariton solitons, superior to those of optical solitons in semiconductor cavity lasers, namely, the picosecond response times and large nonlinearities, suggest that polariton BEC can offer novel functionalities for information-processing devices [167]. The bright solitons observed in [166] require a resonant excitation regime at nonzero in-plane momentum to make use of the dispersion properties of the lower-polariton branch that allow the polaritons to have a negative effective mass. In this regime, strong repulsive interactions between the quasiparticles can be balanced by the effective dispersion to achieve localization. A similar mechanism for spatial localization via effective mass management is well explored for atomic BECs in optically induced band-gap structures [12, 168, 169]. In the absence of the spectral gap, however, localization by means of effective mass management is only possible in one spatial dimension. The question whether localization of polariton BEC with repulsive interactions can occur in the regime of spontaneous condensation at zero in-plane momentum (positive effective mass) and nonresonant excitation, remains open.

In this chapter we examine, both analytically and numerically, formation and dynamical stability of a steady-state BEC of exciton polaritons in microcavities in the presence of a spatially localized optical pump with a Gaussian profile. By employing the open-dissipative Gross-Pitaevskii model [92] describing an incoherently pumped BEC coupled to the exciton reservoir and successfully used in theoretical description of a number of significant experiments [7, 74], we analyze the mechanisms for creating and sustaining two-dimensional spatially localized structures, such as dissipative solitons and vortices. In addition to the trap-free case, we analyze the structure of the localized states with the addition of external harmonic potentials that can be created, e.g., by engineered stress of the microcavity [82]. In the latter case, the localization of the repulsive polariton BEC is due to both the external potentials and the inhomogeneous pump, in contrast to the case of a trapped atomic BEC with a positive scattering length in thermal equilibrium.

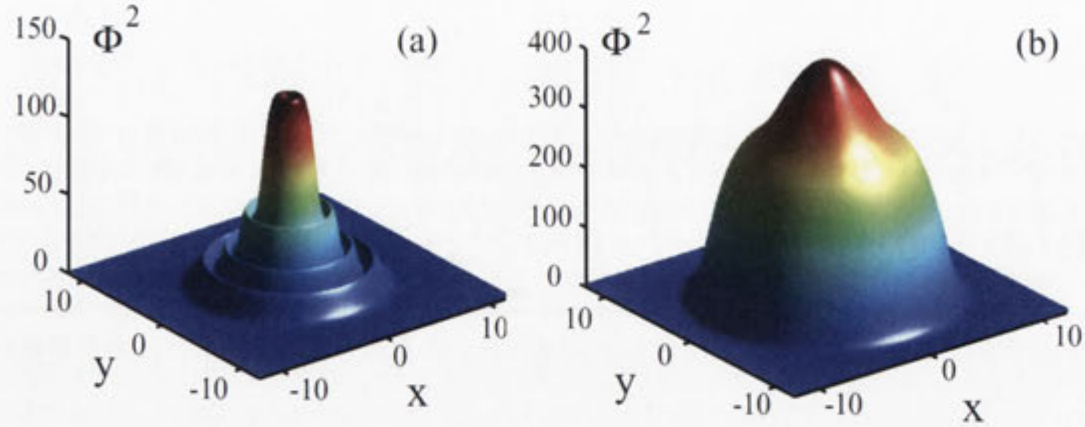

Figure 4.1: Typical steady state density of a harmonically trapped polariton condensate in the regime of (a) narrow and (b) wide pump.

4.2 Localization of polariton condensates in untrapped and trapped regime

In this section we show, analytically and numerically, that, even in the absence of external potentials localization of the steady state polariton BEC occurs due to the effective self-trapping created by the polariton flows. In turn, the polariton flows are created by spatially inhomogeneous off-resonant optical pumping. Spatial localization of the condensate occurs due to the internal balance of superfluid density flows which is identical to that responsible for supporting dissipative "antisolitons" in optical systems. Such localization of continuously self-defocusing solitons occurs despite the repulsive interactions between the quasiparticles, and is analogous to optical gain-guiding effect [170, 171] in its reliance on continuous pumping. Thus a *ground state of the polariton BEC* represents a *dissipative soliton* which is spatially localized and dynamically stable, regardless of the presence of the external potential. A harmonic trapping potential dramatically modifies the structure of the steady state due to the competition with the spatially inhomogeneous pump as seen in Figure 4.1.

A single vortex created in a localized steady-state BEC by phase imprinting is similarly supported by the continuous inhomogeneous pump as a spatially localized *dissipative vortex soliton*. Akin to a vortex line in a trapped atomic BEC with a positive scattering length, it is dynamically unstable [172]. In the absence of potential, a vortex line spirals out of the polariton condensate and the condensate restores to its ground steady state. We show that the addition of fabricated nonrotating harmonic potential modifies the threshold of the optical pumping required to sustain a steady state with an angular momentum and leads to the possibility of a long-term survival of the vortex.

4.3 Model

We consider a spontaneously formed exciton-polariton BEC ($k_{||} = 0$, lower-polariton branch) under the continuous wave nonresonant excitation. The model first suggested in [92] consists of a mean-field equation for the polariton condensate wave function and a rate equation for the inhomogeneous density of the exciton reservoir. We write it here in the form used in [7]:

$$\begin{aligned} i\hbar\frac{\partial \Psi}{\partial t} &= \left[-\frac{\hbar^2}{2m}\nabla_\perp^2 + V(\vec{r},t) + i\frac{\hbar}{2}(Rn_R - \gamma_c)\right]\Psi, \\ \frac{\partial n_R}{\partial t} &= -(\gamma_R + R|\Psi|^2)n_R(\vec{r},t) + P(\vec{r}), \end{aligned} \tag{4.1}$$

where $V(\vec{r},t) = U(\vec{r}) + g_c|\Psi|^2 + g_r n_R(\vec{r},t)$. Here Ψ is the condensate wave function, n_R is the exciton reservoir density, $P(\vec{r})$ is the inhomogeneous optical pump, and $U(\vec{r})$ is the external potential. The critical parameters defining the condensate dynamics are the loss rates of the polaritons γ_c and reservoir excitons γ_R, the stimulated scattering rate R, condensate coupling to the reservoir g_R, and the coefficient g_c quantifying the nonlinear interaction of polaritons. In what follows, we will consider a radially symmetric external trapping potential $U(r) = U_0^2 r^2$, where $U_0 = 0$ in a trap-free case.

The model can be rewritten in dimensionless form by using the following characteristic scaling units of time, energy, and length:

$$T = \frac{1}{\gamma_c}, \quad E = \hbar\gamma_c, \quad L = \sqrt{\frac{\hbar}{m_{LP}\gamma_c}}, \tag{4.2}$$

where m_{LP} is the lower-polariton effective mass. Here, we choose the parameters close to those of the experimental setup of [7], with $m_{LP} = 10^{-4} m_e, g_c = 6 \times 10^{-3} meV\mu m^2, g_R = 2g_c, \gamma_c = 0.33ps^{-1}, \gamma_R = 1.5\gamma_c$, and $R = 0.01\mu m^2 ps^{-1}$. In what follows we use and plot the dimensionless (normalized) variables and parameters. In the experiment polariton properties determined by exciton and cavity photon properties. For instance, experimental lower-polariton mass range is $m_{LP} \approx 10^{-5} - 10^{-3} m_e$ and condensate polariton loss rate can vary from $\gamma_c = 0.01ps^{-1}$ for high-Q samples to $\gamma_c = 0.33ps^{-1}$ for low-Q samples [7].

For small values of $P(\vec{r})$, no condensate is present $\psi_0 = 0$ and the reservoir density is a linear function of the pump intensity $n_R^0 = P/\gamma_R$. This solution is dynamically stable as long as the amplification rate is not able to overcome the losses, i.e. $Rn_R^0 < \gamma_c$. The threshold $P = P_{th}$ corresponds to the value n_R^{th} for the reservoir density, which guarantees equilibrium between amplification and losses, $Rn_R^0 = \gamma_c$. We recall that, in the spatially homogeneous case, one can estimate the threshold pumping power at which the condensate appears in the system, as described in [92]. This threshold is approximately determined by the values of parameters for which stimulated gain equals loss:

$$P_{th} \approx \frac{\gamma_R\gamma_c}{R}. \tag{4.3}$$

The ratio of the polariton n_c to exciton reservoir n_R densities in the steady homogeneous state can then be defined as

$$\frac{n_c}{n_R} = \frac{\gamma_c}{\gamma_R}(\bar{P} - 1), \tag{4.4}$$

where normalized pump is defined as $\bar{P} = P/P_{th} \geq 1$. In general, even in a spatially inhomogeneous case, the typical dynamical behavior of the model Equations (4.1) displays rapid transition to the steady state of the polariton BEC for $\bar{P} > 1$.

Below we consider the properties of the steady state supported by an inhomogeneous

Gaussian optical pump, $P(r) = P_0 \exp(-r^2/\sigma^2)$, with or without an additional trapping potential. The spot size of the optical pump is considered to be small compared to the size of the sample, so that the local density approximation [173] is not applicable.

4.4 Steady state of the condensate

4.4.1 A. Theory

For a general continuous-wave pump, the condensate wave function in the steady state can be looked for in the following general form: $\Psi = \psi(x,y)\exp(-i\mu t)$, where μ is the energy (chemical potential) of the steady state. If both the external potential and the pump are radially symmetric, we can rewrite the model system in polar coordinates $(x,y) \to (r,\theta)$ and reduce the problem to finding radially symmetric steady states $\psi(x,y) = \psi(r)\exp(im\theta)$, where m is the phase winding number [174] (topological charge of a vortex), and the ground state corresponds to $m = 0$.

The steady-state wave function $\psi(r)$ obeys the following stationary equation:

$$\nabla_r^2\psi - 2V(r)\psi - i(Rn_R^0 - \gamma_c)\psi + 2\mu\psi = 0, \tag{4.5}$$

where $\nabla_r^2 = \partial^2/\partial r^2 + (1/r)\partial/\partial r - m^2/r^2, V(r) = g_c|\psi|^2 + g_R n_R^0 + U(r)$ and the staeady-state reservoir density is found from Equations(4.1) as

$$n_R^0 = \frac{P(r)}{\gamma_R + R|\psi|^2}. \tag{4.6}$$

All physical parameters in Equation (4.5) are dimensionless, and under the adopted scaling in Equation (4.2), $\gamma_c = 1$. However, we formally retain this parameter in subsequent formulas.

The stationary wave function can be further separated into the real amplitude and phase: $\psi(x) = \Phi(x)\exp[i\phi(x)]$. Following the analysis suggested in [175] for the generalized complex Ginzburg-Landau equation, we can obtain asymptotic behavior of amplitude and phase of the condensate wave function. In the absence of a trapping potential, $U(r) = 0$, the requirement of spatial localization, $P(r) \to 0, |\psi(r)| \to 0$, imposed on both the pump and the condensate wave function at large r leads to the following asymptotic behavior of the amplitude and the phase at $r \to \infty$:

$$\Phi(r) \sim A\exp(-p_- r), \quad \phi(r) \sim B + p_+ r, \tag{4.7}$$

where $p_\pm = [(\mu^2 + \gamma_c^2/4)^{1/2} \pm \mu]^{1/2}$, and A, B are real constants. This asymptotic behavior shows that the condensate decays slower than the pump field, and therefore the spatial profile of the condensate will significantly differ from that of the pump.

Conversely, at $r \to 0$, the asymptotic behavior is found to be

$$\Phi(r) \sim Cr^{|m|}\exp(-q_- r^2), \quad \phi(r) \sim q_+ r^2, \tag{4.8}$$

where $q_- = (1/2)(1+|m|)^{-1}[V(0) - \mu]$ and $q_+ = (1/4)(1+|m|)^{-1}[Rn_R^0 - \gamma_c]$, and for the ground state $C = \Phi(0) = \Phi_0$. For $V(0) < \mu$, the second derivative of the amplitude changes sign at $r = 0$, i.e., the condensate displays a central "dip" in its density profile and acquires a ring shape, as seen in Figure 4.1(a).

The presence of the harmonic trap $U(r) = U_0^2 r^2$ dramatically modifies the asymptotic behavior of the condensate wave function for $r \to \infty$ [176], so that

$$\begin{aligned} \Phi &\sim A\exp[-U_0^2 r^2 + (\mu - 1/2)\ln(2U_0 r)], \\ \phi &\sim B + \gamma_c \ln(2U_0 r). \end{aligned} \tag{4.9}$$

The asymptotic behavior of a trapped polariton BEC at $r \to 0$ is described by Equation (4.8).

For a spatially localized Gaussian pump, $P(r)$, the spatial localization of the condensate in the absence of an added trapping potential is counterintuitive. Indeed, the effective potential $V(r)$ formed by the repulsive nonlinearity (due to polariton scattering) and interaction with the exciton reservoir is *antitrapping*. Therefore the balance of nonlinearity and dispersion responsible for nonlinear localization in conservative condensate systems cannot be achieved. Physically, the existence of the spatially localized steady state of the polariton condensate can be understood by examining the internal flows of the dissipative polariton superfluid, analogous to the Pointing vector flows in dissipative optical systems [175, 177]. Indeed, by defining the superfluid current density (flux) in the standard way $\vec{j} = Im(\Psi^* \nabla \Psi)$, we can recast Equation (4.5) in the form of coupled equations for the amplitude of the condensate wave function Φ and radial component of the stationary flux $J = j_r = n_c v_r$, where $n_c = \Phi^2(r)$ is the condensate density, and v_r is the radial component of the flow velocity $\vec{v} = (\partial\phi/\partial r)\vec{e}_r + (m/r)\vec{e}_\theta$.The equations for these variables take the following form:

$$\begin{aligned} &\frac{1}{r}\frac{d}{dr}(rJ) - (Rn_R^0 - \gamma_c)\Phi^2 = 0, \\ &\nabla_r^2 \Phi - 2[V(r) - \mu]\Phi - V_J \Phi = 0, \end{aligned} \tag{4.10}$$

where $V_J = J^2 \Phi^{-4} = (\partial\phi/\partial r)^2$. The first equation of the system is the continuity equation for the stationary flow with source and sink. The first term in this equation is simply the divergence of the flux, $D = \nabla \vec{j}$, which serves as a local measure of gain ($D > 0$) or loss ($D < 0$). A steady state exists if generation of the polariton superfluid via continuous pumping is balanced by its dissipation. This condition can be formulated in terms of the flux as follows [177]:

$$\int_0^\infty D(r) r dr = 0. \tag{4.11}$$

Remarkably, this condition can be satisfied *regardless of the sign of the nonlinear interactions* in the systems, i.e., for both repulsive (as in the case of polaritons) and attractive nonlinearities. The nonlinearity affects the energy (chemical potential) of the steady state and its spatial extent according to Equations (4.7) and (4.9). We note that nonlinear eigenstates for a very similar dynamical one-dimensional system with linear loss and spatially localized gain and without additional external potential were found in [171]. The key feature of our system is similar: for the given parameters of gain and loss, the chemical potential, μ, is unique.

The second Equation in (4.10) highlights the composition of the effective potential supporting the condensate wave function as its eigenstate with the corresponding eigenvalue μ. It is clear that the radial flux that exists due to the spatially inhomogeneous phase of the condensate $\phi(r) \neq const$, forms an attractive potential that can trap a spatially localized bound state even in the absence of the external trapping $U_0 = 0$. In the linear limit (i.e., for very small condensates and/or nonlinearity) this effective trapping potential due to the flux is approximately given by

$$V_J(r) \approx \frac{\gamma_c^2}{4}(\bar{P}_0 - 1)^2 r^2. \tag{4.12}$$

The effect of existence of the localized linear modes supported purely by the localized gain is known as "gain guiding" in optics [170].

4.4.2 B. Numerical results

The existence of the localized steady state of the dissipative polariton BEC with the properties described in the previous section can be demonstrated by the numerical simulation of the time-dependent model Equations (4.1). Figure 4.2 shows the typical dynamical behavior and transition to the steady ground state ($m = 0$) of the polariton component for intermediate values of pumping power ($\bar{P}_0 = 3$) in the trap-free regime. In addition, from the numerical simulations we can extractand plot the following dynamical quantity:

$$\mu(t) = -\frac{1}{4}\frac{\int_S [\nabla^2|\Psi|^2 - 2|\nabla\Psi|^2 - 4V|\Psi|^2]d\vec{r}}{\int_S |\Psi|^2 d\vec{r}}, \tag{4.13}$$

where S is the numerical integration domain. In the steady state limit this quantity coincides with the chemical potential of the condensate $\mu(t) \to \mu$. As can be seen from the dynamical simulations for $\bar{P} > 1$ in Figure 4.2, the steady-state regime is reached quickly, and the chemical potential is well defined. Alternatively, the steady state is found by solving the stationary Equation (4.5) by the standard one-dimensional relaxation method. The condensate wave function displays characteristic inhomogeneous amplitude and phase profile $\phi(r)$ in Figure 4.3 with the limiting behavior well described by Equations (4.7) and (4.8).

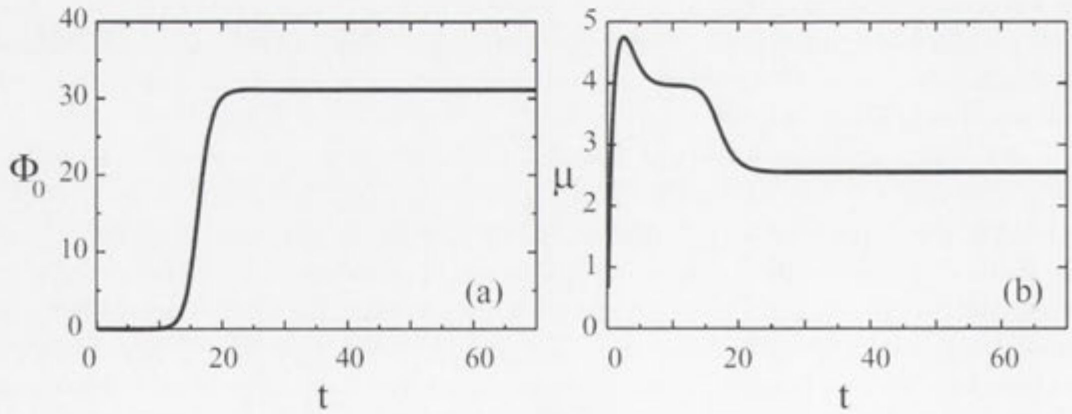

Figure 4.2: Typical time evolution of (a) the condensate peak and (b) the chemical potential for $\bar{P}_0 = 3$, without trapping potential.

From Figure 4.3(c) it is seen that the inhomogeneous phase of the condensate wave function results in the nonzero flux of the polariton superfluid. Due to the spatially localized pump, the polariton superfluid is continuously generated in the core area of the steady state $D > 0$ and dissipated on its wings $D < 0$. Thus the ground state of the strongly repulsive polariton BEC is a spatially localized *dissipative soliton*. Its spatial localization is owed to the balance of the superfluid currents, and the internal structure of the currents is similar to that of a continuously "self-defocusing" dissipative "antisoliton" of the generalized complex Ginzburg-Landau equation described in [177].

The presence of a harmonic trap modifies the asymptotic behavior of the condensate and phase according to Equation (4.9), as shown in Figure 4.3(b). Nevertheless, the structure of the internal flow within the ground state of the condensate remains qualitatively the same, as seen in Figure 4.3(d). In the trapped regime the internal flow of the polariton superfluid currents lead to significant distortions in the condensate density profile, $n_c(r)$. In particular, a wide pump with $\bar{P} \gg 1$ leads to a well-pronounced central peak [shown in Figure 4.1(b) for $\sigma^2 = 40$ and $\bar{P}_0 = 10$] noted in numerical simulations of a similar model of polariton BEC [178] and also hinted at in experimental observations of a trapped exciton-polariton condensate [82].

4.5 Trapped vs trap-free regime

The ground $m = 0$ state of the polariton condensate can be characterized by the dependence of chemical potential μ on the parameters of the pump. In the absence of the trapping potential, this dependence is determined by the flux balance condition, and in the limit of low condensate densities the dependence of μ on the pump intensity is linear $\mu \sim \bar{P}_0 = P_0/P_{th}$. In the presence of the harmonic potential, this condition is modified by the trap, as seen in Figure 4.4.

For a fixed width of the pump, the cut-off value of $\bar{P}_0$ corresponds to the linear limit $|\psi| \to 0$, and deviates quite significantly from the value $\bar{P}_0 = 1$ determined by the threshold behavior (4.3) in the homogeneous excitation case. The linear limit is determined by the cutoff for the ground state in the effective two-dimensional (2D) potential formed by the combination of the external harmonic trap $U(r)$, repulsive potential due to the spatially localized pump $V_R(r) = g_R n_R^0$, and the internal inhomogeneous flux $V_J(r)$ given by Equation (4.12). This cutoff can be estimated from the condition that the effective potential in the linear limit is trapping (attractive) rather than antitrapping (repulsive). Thus, the bound state appears in the effective potential at the value of $\bar{P}_0$ given by the positive root of the equation:

$$\bar{P}_0^2 - 2\left(1 + \frac{4g_R}{\gamma_c R}\frac{1}{\sigma^2}\right)\bar{P}_0 + \left(1 + \frac{4U_0}{\gamma_c^2}\right) = 0. \tag{4.14}$$

According to this formula, for the parameters in Figure 4.4, the ground state appears in the trap-free system at $\bar{P}_0 \approx 1.97$. The presence of the harmonic trap with $U_0^2 = 0.1$ lowers the threshold to $\bar{P}_0 \approx 1.61$. The predicted tendency of the harmonic confinement to *lower* the threshold of the steadystate formation compared to the trap-free case, agrees with the numerically calculated cut-off values in Figure 4.4. Above the threshold, the harmonic trap leads, for the same parameters of the pump, to the formation of the steady-state BEC with stronger spatial localization and higher peak density, as can be seen from comparison of Figures 4.3(a) and 4.3(b).

For a fixed strength of the harmonic confinement, the width of the pump spot de-

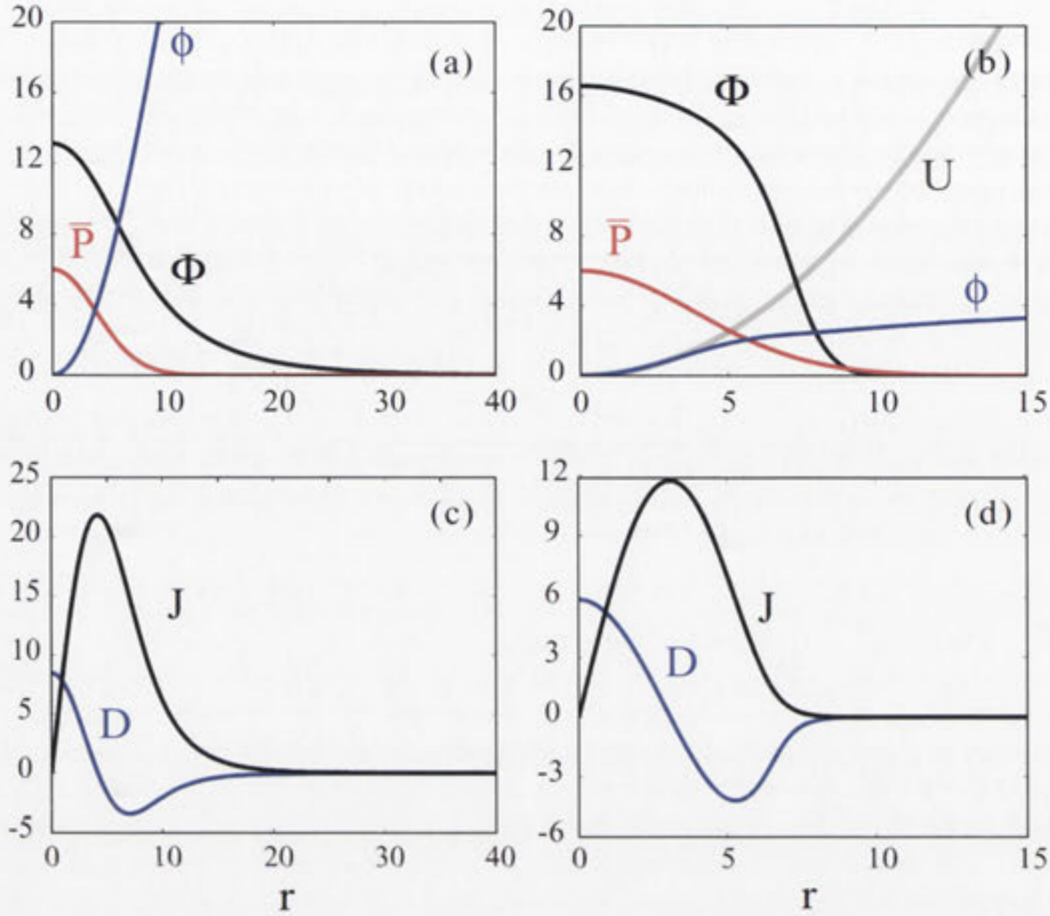

Figure 4.3: Radial profiles of the condensate ground state in (a) trap-free and (b) harmonically trapped case. Both amplitude, $\Phi(r)$, and phase, $\phi(r)$, are shown in comparison to the Gaussian pump profile $P(r)/P_{th}$ with the amplitude $\bar{P}_0 = P(0)/P_{th} = 6$. Profiles of the radial flux J and its divergence D (scaled up by the factor of 10) for the ground state are shown for the (c) trap-free and (d) trapped cases, respectively. The harmonic potential of the depth $U_0^2 = 0.1$ is shown in (b) by the gray curve.

termines different trapping regimes. Intuitively, for an excitation spot much wider than the trap, the limiting behavior should be described by a homogeneous pump approximation $P(r) \approx P_0$ [173, 178]. In the opposite regime of a narrow excitation spot, the limiting behavior should be close to that of a free condensate. Contrary to this intuitive picture, the dependence of the chemical potential μ on the width of the excitation spot σ^2 calculated numerically shows dramatic differences for trapped and free condensates as seen in Figure 4.5. Most notably, a trapped condensate displays well-pronounced bistability, whereby both narrow and wide pumps can support two different steady states with the same energy. In addition, the condensate density profiles are strongly spatially modulated as shown in Figure 4.6. This is due to the presence of two competing spatial scales. One of them, $\sim \sigma$, is defined by the pump, and the other one, $\sim r_{TF}$, is defined by the trapping potential and is given by the characteristic radius of the wave function in the Thomas-Fermi limit. The latter is obtained by neglecting both phase and density

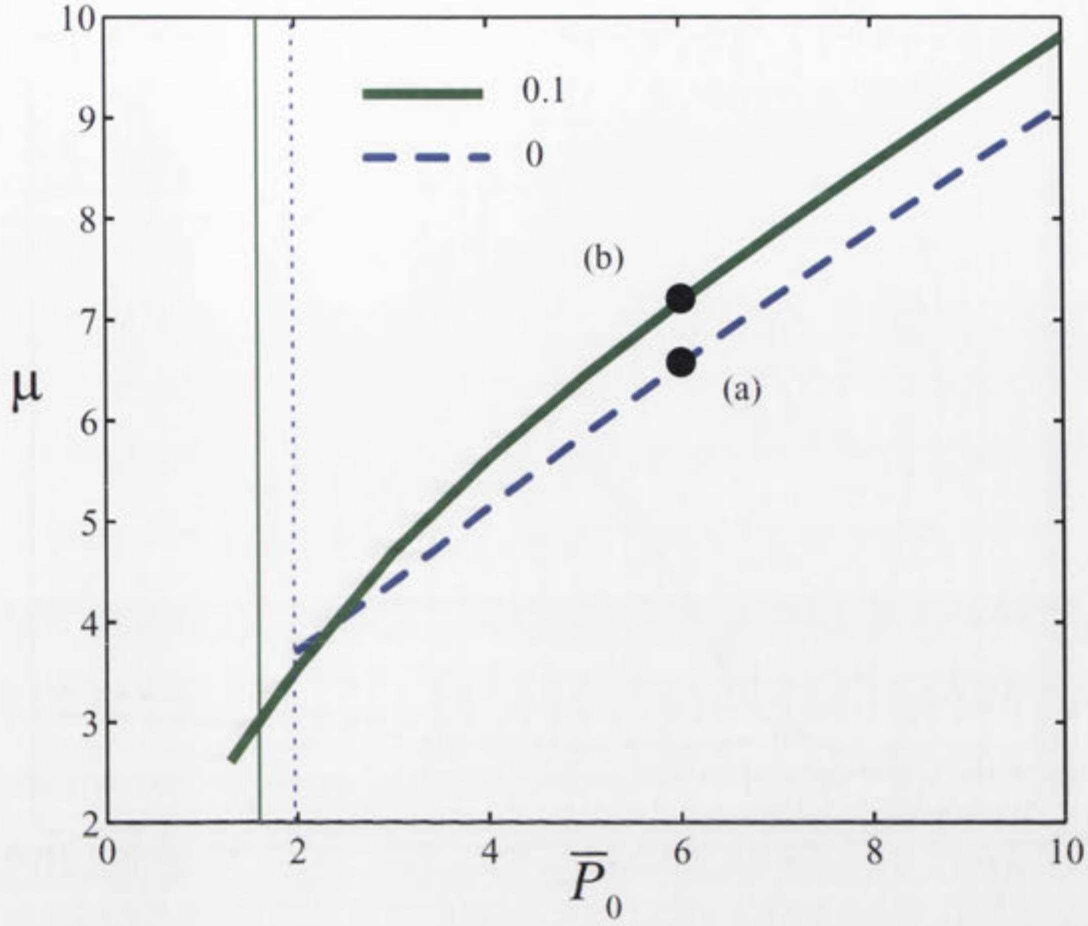

Figure 4.4: Dependence $\mu(\bar{P}_0)$ for the ground state $m = 0$ without the harmonic potential (dashed line) and in the presence of a harmonic trapping potential $U(r) = U_0^2 r^2$ with $U_0^2 = 0.1$ (solid line). Vertical dashed and solid lines indicate the cut-off values of $\bar{P}_0$ for the ground state given by the linear limit in Equation(4.14) . Marked points (a) and (b) correspond to the condensate profiles shown in Figure 4.3. The width of the pump spot is $\sigma^2 = 30$ in both cases.

gradients in Eqsuation (4.10), as the solution to the equation:

$$U_0^2 r_{TF}^2 + \frac{\gamma_c g_R}{R} \bar{P}_0 \exp\left(-\frac{r_{TF}^2}{\sigma^2}\right) = \mu \tag{4.15}$$

In the regime of a wide pump, the condensate density can be reasonably well approximated by the radially symmetric Thomas-Fermi profile with the radius r_{TF} given by Equation (4.15), as can be seen in Figure 4.6(a). In this regime, the ground state in the form of a dissipative soliton becomes dynamically unstable with respect to azimuthal perturbations for $\bar{P} \gg 1$, as established in [178]. There it was shown that this instability can lead to rotational symmetry breaking whereby multiple vortex states enter the condensate.

For a very narrow pump, $\sigma^2 \ll r_{TF}^2$, the Thomas-Fermi radius exactly coincides with the well-known expression for a conservative BEC with repulsive interparticle interactions in a harmonic trapping potential: $r_{TF}^0 = \sqrt(\mu/U_0^2)$. In our numerical simulations

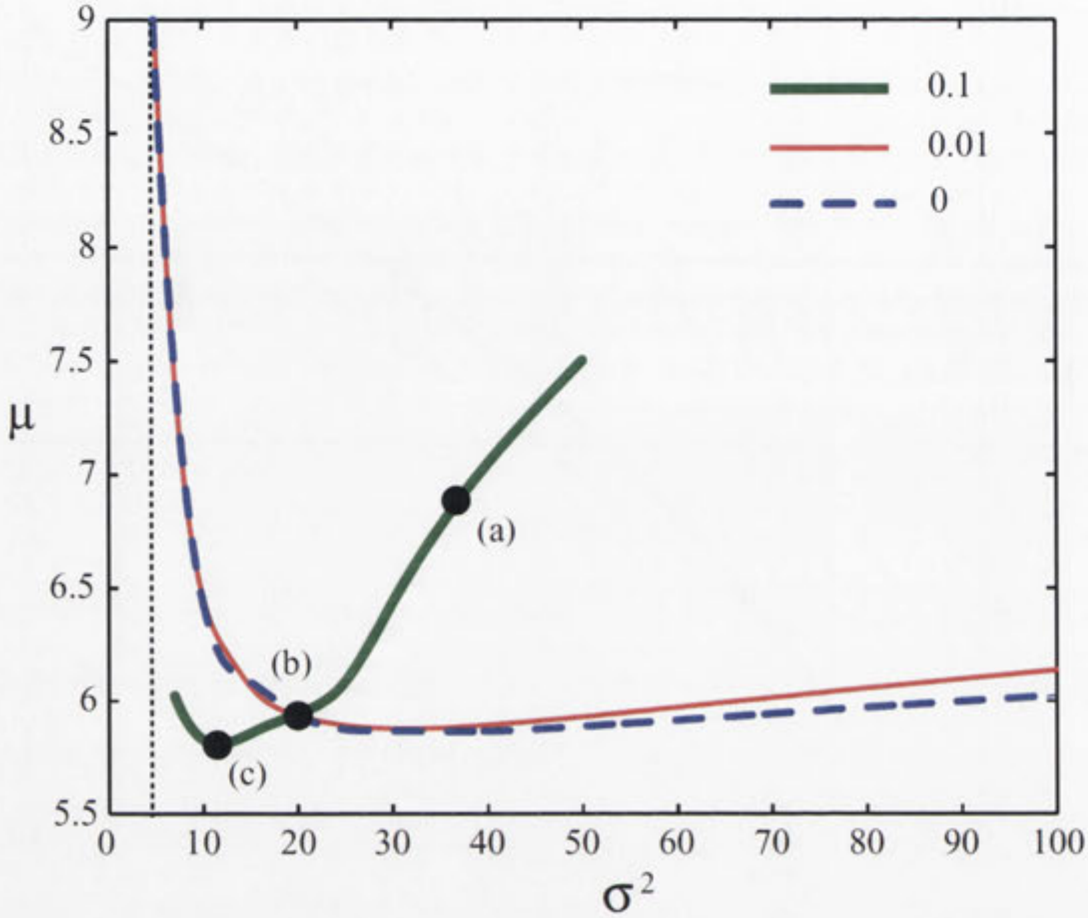

Figure 4.5: Dependence $\mu(\sigma^2)$ for the ground state $m = 0$ achieved at $\bar{P}_0 = 5$ without and with a harmonic trapping potential $U(r) = U_0^2 r^2$ with $U_0^2 = 0$ (dashed), $U_0^2 = 0.01$ (solid), and $U_0^2 = 0.1$ (thick solid line). The vertical dotted linemarks the cut-off value of the pump width for the trap-free ground state given by the linear limit expression (4.14) resolved with respect to σ^2. Marked points [(a)-(c)] correspond to the condensate profiles shown in Figure4.6.

we find that $r_{TF} \approx r_{TF}^0$ for a wide range of values $\sigma < r_{TF}$. In this parameter regime the condensate density profile strongly deviates from the Thomas-Fermi profile [Figures 4.6(b) and 4.6(c)], as neither phase nor density gradients can be neglected. The condensate experiences strong modulations of density with a notable density dip along the line $D = 0$ separating the regions of loss and gain. The condensate peak density is also damped as the pump narrows down and the dip at $r = 0$ appears for the values of σ corresponding to the negative value of q_- in Equation (4.8). We note that the point (b) in Figure 4.5 corresponds to $q_- = 0$ for $U_0^2 = 0.1$. Under the conditions of a strong ($\bar{P}_0 \gg 1$) narrow pump the steady state is dynamically unstable and exhibits strong peak density oscillations.

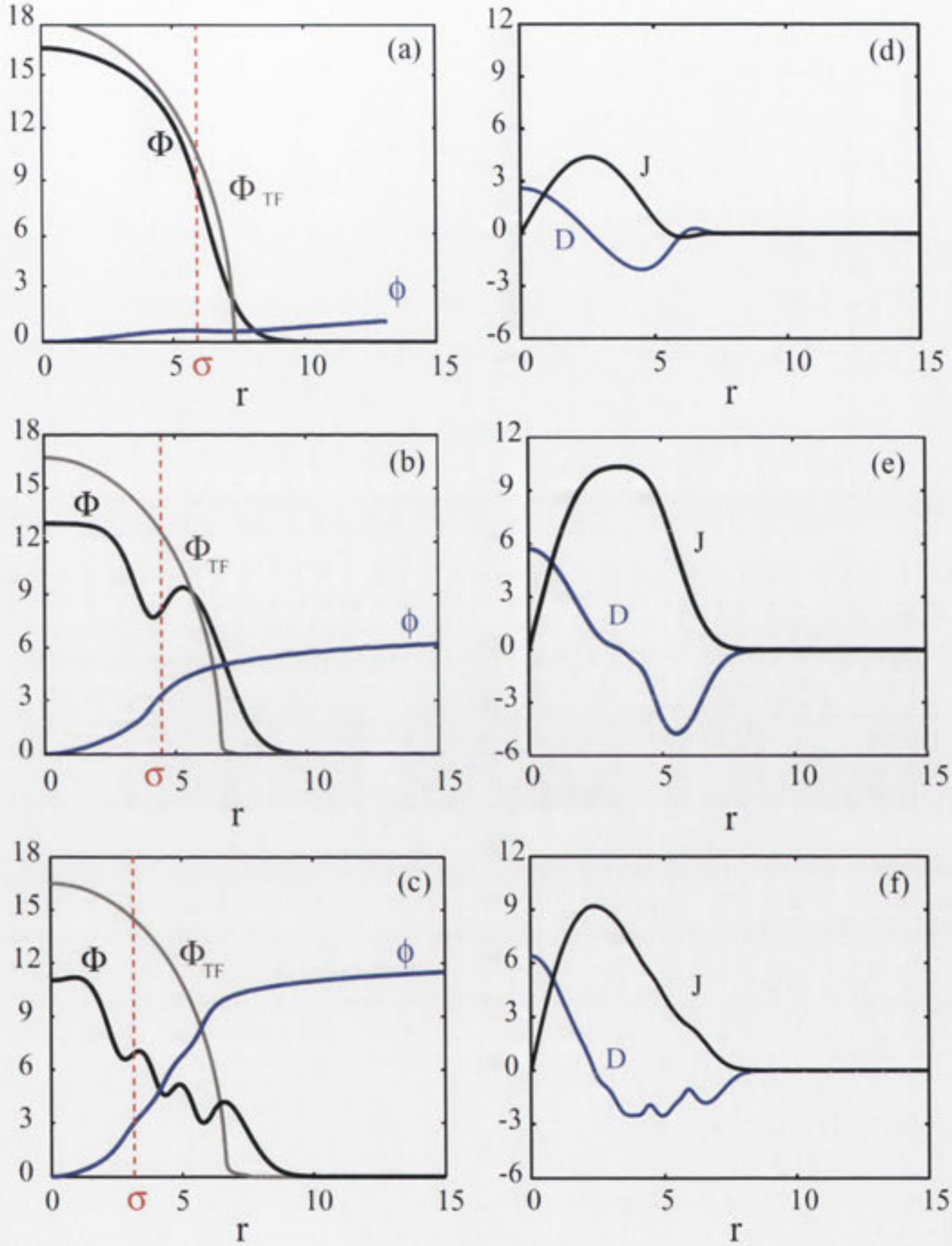

Figure 4.6: Radial shapes of the condensate ground states in the harmonically trapped case for $U_0^2 = 0.1$, $\bar{P}_0 = 5$ and the width of the pump spot σ^2 corresponding to the points marked in Figure4.5 (a)-(c). Both amplitude, $\Phi(r)$, and phase, $\phi(r)$, are shown in comparison to the condensate profile obtained in the Thomas-Fermi approximation, Φ_{TF} (gray). (d)-(f). Profiles of the radial flux J and its divergence D (scaled up by the factor of 10) for the ground states shown in the panels (a)-(c).

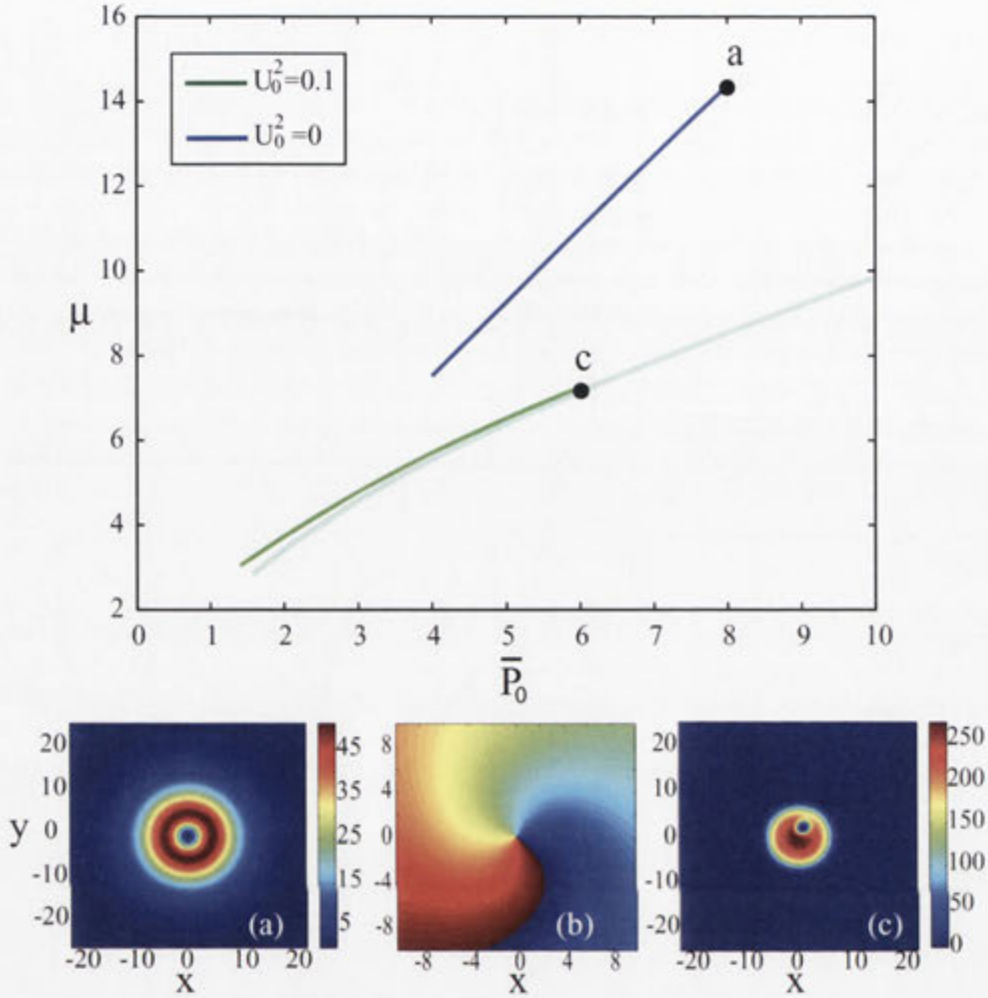

Figure 4.7: Top: Dependence $\mu(\bar{P}_0)$ for the vortex state $m = 1$ without and with the harmonic trapping potential $U(r) = U_0^2 r^2$ for $\sigma^2 = 30$. The semitransparent line indicates the corresponding dependence for a trapped $m = 0$ state from Figure 4.4. Bottom: (a) Condensate density and (b) phase for a dynamically unstable $m = 1$ stationary vortex state in a trap-free condensate at $\bar{P}_0 = 8$. (c) Metastable rotating vortex state supported by a harmonic trap ($U_0^2 = 0.1$) at $\bar{P}_0 = 6$.

4.6 Single vortex state

Spatially localized dissipative vortices are similarly found as higher-order steady states of the system with $m \neq 0$ [179], both in a trap-free and harmonically trapped polariton BEC. Numerically, the system relaxes to a single steadystate vortex when a phase factor $\exp(im\theta)$ is imprinted onto a condensate "seed" at the initial stages of evolution. The dependence of the chemical potential μ on the pump amplitude $\bar{P}_0$ is plotted in Figure 4.7 for a vortex with $m = 1$. As expected, the chemical potential and the cutoff for this excited state are higher than those of the ground state of the trap-free condensate. In contrast, in a harmonic potential the vortex and the ground state become nearly degenerate (see Figure 4.7).

The global phase of the vortex is imposed not only by the vorticity but also by the nonzero flux, and therefore depends on both azimuthal (θ) and radial (r) coordinates.

Using the Expression (4.8) for the radial dependence of the phase near the vortex core, we find that the lines of the constant phase follow a spiral trajectory described by the equations

$$x_s(\theta) = \sqrt{(}\theta/q_+)\cos\theta, \quad y_s(\theta) = \sqrt{(}\theta/q_+)\sin\theta. \tag{4.16}$$

This spiral phase structure is shown in Figure 4.7(b) for the numerically found localized vortex state in Figure 4.7(a), without the trapping potential. It is a signature of the polariton BEC vortex observed in the experiments [74], and also appears as a characteristic feature of vortex states in other dissipative systems [175, 180–182].

The ground state ($m = 0$) of the polariton condensate is dynamically stable in the absence of a trap. In contrast, we find that a single vortex created in a localized steady-state BEC by phase imprinting is dynamically unstable and, in the absence of potential, spirals out of the condensate, as predicted for the case of trapped dissipative BEC of alkali atoms [172, 183]. As can be seen from comparison of Figures 4.4 and 4.7, the addition of a stationary (i.e., nonrotating) harmonic potential dramatically modifies the threshold of the optical pumping required to sustain a steady state of a polariton BEC with an angular momentum and leads to the possibility of a long-term survival of the vortex in the form of an eccentric rotating state shown in Figure 4.7(c). The detailed study of the stabilizing effect of the trapping potential on the vortex dynamics and the dynamics near the onset of rotational symmetry breaking [178] is beyond the scope of this study. However, we have confirmed that a wide pump (corresponding to small density gradients in the harmonic trap) tends to stabilize the vortex state.

4.7 Concluding remarks

In this chapter we have studied and characterized the 2D stationary regime of the polariton BEC in the framework of an open-dissipative Gross-Pitaevskii model coupled to an exciton reservoir and described, both analytically and numerically. Properties of the ground and excited states (vortices) depend on the pump and trapping parameters. We have shown that the spatial localization of the condensate, even in the absence of a trapping potential, is supported by the balance of the internal superfluid flows established by an inhomogeneous nonlinear gain due to optical pump and linear loss due to the decay of the polaritons. The ground state of the condensate can therefore be described as a continuously self-defocusing dissipative soliton. We have also investigated localized dissipative vortex states and have shown that they can display metastable behavior in nonrotating trapping potentials.

Finally, we note that the open-dissipative model with the inhomogeneous pump used here and successfully employed for theoretical description of experiments with microcavity polaritons, has many similarities to optical systems with localized gain landscapes [171, 180]. These and similar studies suggest that the 2D stationary regime of polariton BEC can potentially display a rich variety of localized states which are not exhausted by radially symmetric configurations. In particular, the experiments with polariton BEC excited by the elliptical optical pump have demonstrated pattern formation due to the appearance of standing waves [184]. Furthermore, the recent experiment with polariton BECs created by two pump spots [185] demonstrates novel possibilities arising from interaction of two dissipative solitons with variable separation. The clear understanding of the structure of phase gradients underpinning the existence of steady-state polariton condensates presented in our work enables us to gain immediate insight into the properties and outcomes of such interactions. The possibility to create a rich variety of localized states by varying the spatial properties of the off-resonant optical pump are currently under investigation.

Chapter 5

Self-localization of polariton condensates in periodic potentials

5.1 Introduction

Ultracold atomic gases loaded into periodic potentials created by optical or magnetic lattices continue to provide a fascinating tool for exploring fundamental quantum many-body physics, as well as offering an opportunity to build quantum simulators and scalable quantum information processing systems [186, 187].

In recent years, polariton condensates created in semiconductor microcavities [5] have emerged as an attractive alternative to the atomic systems, owing to the relatively high condensation temperatures, direct momentum and real-space imaging via the cavity photoluminescence, and possibility to manipulate the condensate using both optical pump and structure of the microcavity [188]. Therefore, interest to achieving the polariton condensation in periodic potentials and exploring macroscopic population of the single-particle band-gap spectrum has increased enormously. Considerable effort has also been directed towards achieving the polariton condensation in one- and two-dimensional 'lattice' potentials and observing macroscopic population of the single-particle band-gap spectrum. So far, the majority of the experiments with exciton-polaritons in a periodic potential have been performed in a pulsed excitation regime, which has allowed to populate and image rapidly decaying high momentum states in a periodic potential. The staggered 'π-state' phase structure of the higher-order Bloch states has been demonstrated in a 1D lattice created by metal deposition onto the microcavity [87]. Similarly, condensation into second band has been achieved in a 2D square lattice [89], and the Brillouin zone structure of the Kagome lattice has been mapped out [189]. Recently, condensation into an energy state corresponding to a single-particle spectral gap has been demonstrated in a 1D lattice created by lateral modulation of quantum wires in a microcavity [190]. Apart from the fabricated lattices, condensation in the tuneable acoustically created lattices has been investigated [191, 192].

One of the most fundamental effects due to the band-gap structure is the localization of the condensate *in real space*. In Kagome lattices [189] this, in principle, can be achieved by accessing the flat band of the tight-binding spectrum, which signifies dispersionless dynamics. Alternatively, spatial localization in spectral gaps of the band-gap structure can be achieved due to the balance of repulsive nonlinearity and modified effective dispersion due to the negative effective mass. This mechanism has been thoroughly explored in the context of gap solitons both in photonic [114, 193, 194] and matter-wave [12, 168, 169, 195–197] band-gap structures. Scarce theoretical descriptions of exciton-polaritons in periodic potentials [198, 199] so far disregarded the fact that, unlike the atomic condensate in thermal equilibrium, the polariton condensate is a *driven, highly dissipative system* due to finite lifetime of quasiparticles and the presence of the optical pump. This distinct dissipative nature of the polariton condensate becomes very important in the continuous-wave (CW) non-resonant excitation regime [5], which creates long-living condensates with spontaneously established spatial coherence and long coherence times. The presence of gain-assisted localization and related dynamics may play a critical role for such dissipative condensates [178, 200] in contrast to atomic Bose-Einstein condensates in thermal equilibrium.

In this section, we identify and analyse the mechanism for localization of a dissipative polariton condensate in an off-resonant CW excitation regime, with an external periodic potential. We show that the driven-dissipative nature of the polariton condensate gives rise to additional effective potentials local to the condensate, namely a defect-type potential introduced by the pump-induced polariton reservoir and a potential self-induced by the strongly modulated flow of polaritons away from the excitation spot. Trapping of the polariton condensate in these effective potentials, which *supersede the external lattice potential*, is responsible for its spatial localization.

5.2 Model

We assume that the near-equilibrium polariton condensate is formed via CW incoherent excitation with a spatially inhomogeneous pump. Above condensation threshold, it can be described by the mean field open-dissipative model for a polariton condensate coupled to an incoherent polariton reservoir density [92]:

$$
\begin{aligned}
i\frac{\partial \Psi}{\partial t} &= \left[-\frac{\nabla_\perp^2}{2} + V_{NL} + \frac{i}{2}(Rn_R - \gamma_c) + V_L\right]\Psi, \\
\frac{\partial n_R}{\partial t} &= -(\gamma_R + R|\Psi|^2)n_R(\vec{r},t) + P(\vec{r}).
\end{aligned}
\tag{5.1}
$$

Here Ψ is the condensate wavefunction, $V_L(\vec{r})$ is a linear periodic potential created for the condensate, and $V_{NL} = g_c|\Psi|^2 + g_R n_R$ is an effective nonlinear potential depending both on the condensate density and the reservoir density, n_R, which is determined by the inhomogeneous optical pump $P(\vec{r})$. The parameters defining the condensate dynamics are the relaxation rates of the condensed polaritons γ_c and reservoir polaritons γ_R, the stimulated scattering rate R, and the polariton-polariton interaction strengths g_R, g_c. We have written the model Equations (5.1) in a dimensionless form by using the characteristic scaling units in Equation (4.2) [201]. Under this scaling $\gamma_c = 1$, however we formally retain this parameter hereafter. The scaling units are calculated using the parameters close to those of the experimental setup of [7], with $m_{LP} = 10^{-3} m_e$, $g_c = 6 \times 10^{-3}\ meV\ \mu m^2$, $g_R = 2g_c$, $\gamma_c = 0.02\ ps^{-1}$, $\gamma_R = 1.5\gamma_c$, and $R = 0.01\ \mu m^2\ ps^{-1}$.

5.3 Localization in 1D

We begin our consideration with a simplest, one-dimensional (1D) model of a quasi-1D polariton condensate (e.g., confined in a quantum wire [202]), subject to a periodic potential approximated by a harmonic function $V_{\rm L}(x) = V_0 \sin^2(k_l x)$, with the lattice constant

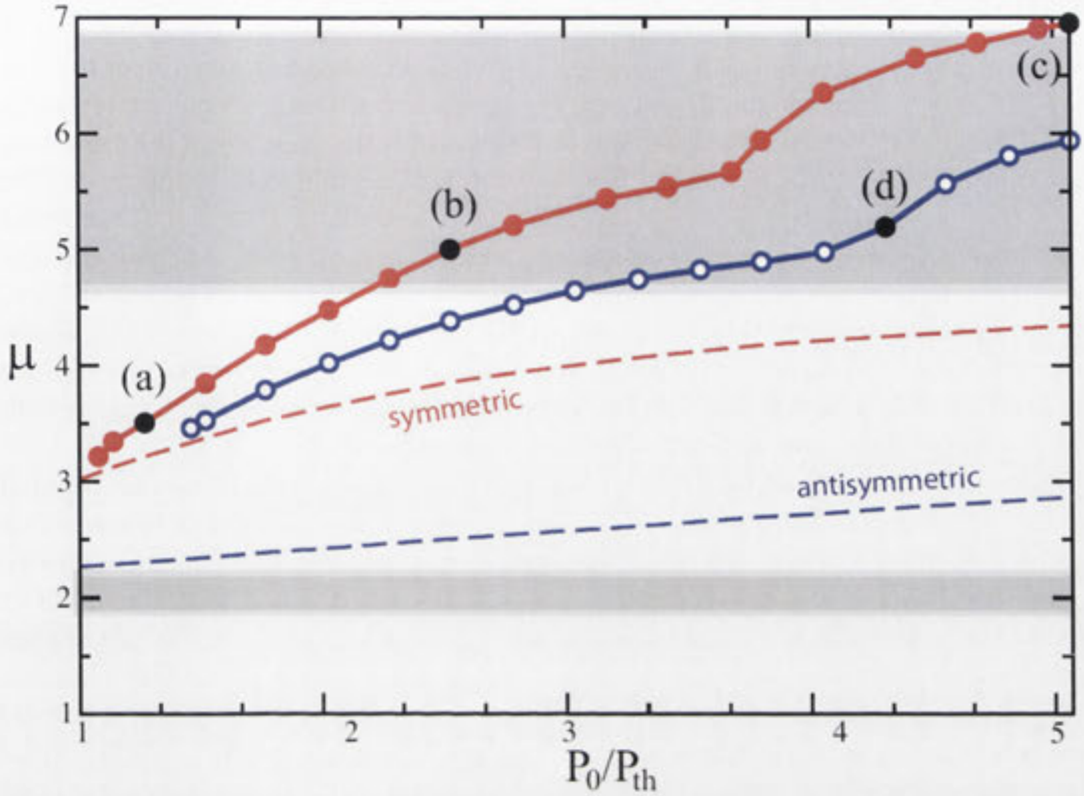

Figure 5.1: Steady state energies of the polariton BEC obtained with CW on-site (closed circles) or $\pi/4$ off-site (open circles) narrow Gaussian pump with the width $\sigma^2 = 0.6$. Shaded (open) areas show bands (gaps) of the Bloch-wave spectrum in the 1D linear lattice potential ($V_0 = 5.0$, $k_l = 1.5$). Dashed lines are linear defect states in the effective potential $V_L(x) + g_R P(x)/\gamma_R$.

$a = \pi/k_l$. The periodicity of the potential imposes a band-gap structure onto the LP branch of the polariton dispersion curve [87], and we can consider population of this band-gap structure by polaritons depending on the pump intensity and width. To this end, we look for the steady state solutions $\Psi(x) = \psi(x)\exp(i\mu t)$ of the model Equation (5.1) governed by the stationary complex Ginzburg-Landau equation with inhomogeneous nonlinear gain and linear loss. We will consider the inhomogeneous Gaussian pump profile $P(x) = P_0 \exp(-\sigma^2 x^2)$ and relate the peak intensity of the pump to the threshold homogeneous pump intensity $P_{th} \approx \gamma_R\gamma_c/R$ [92].

As has been established experimentally [7, 202] and shown theoretically [173, 178, 201], CW of-resonant pump leads to spatial localization of polariton BEC *even without an external potential*. This effect, resulting in formation of *dissipative solitons* [201, 203] is due to the balance of gain and loss in the system and occurs irrespective of the sign of the nonlinear interactions. This mechanism is dramatically different from conventional balance of nonlinearity and dispersion (diffraction) responsible for formation of bright solitons in the coherent fields. The repulsive polariton-polariton interaction then leads to considerable spatial extension spot [178, 200–202] and results in density deformations which are especially pronounced in the presence of a trap [82, 178, 201]. In what follows, we will demonstrate that spatial localization of the condensate due to the balance between gain an loss persists in the presence of a periodic potential.

5.3.1 Narrow excitation

A spatially narrow excitation, $P(x)$, can selectively target a single lattice site of the size up to 1 μm and therefore we can distinguish between an on-site and off-site excitation. In the later case, the peak of the excitation spot can be arbitrarily offset from the minimum of the lattice potential. As can be seen from examining Equation (5.1), in the case of the pump intensity near the threshold for the condensate formation, $P_0/P_{th} \sim 1$, nonlinear effects can be neglected. In this case, assuming a straightforward balance of gain and loss terms, Equation (5.1) would describe a condensate in a linear periodic potential $V_L(x)$ with the addition of a linear defect induced by the pump, $g_R n_R^0 \approx (g_R/\gamma_R)P(x)$, where $n_R^0 = P/(\gamma_R + R|\psi|^2)$ is the steady state reservoir density. The energy of the lowest order linear defect modes is plotted as a function of pump intensity in Figure 5.1, together with the band-gap spectrum imposed by the linear periodic potential.

Taking this spectrum as a frame of reference, we can examine the energy and spatial structure of the localized steady state depending on the pump intensity. The respective dependence is plotted in Figure 5.1 and shows that, near the threshold on-site excitation, the energy of the localized state is indeed very close to that of a symmetric linear defect mode. As the ratio P_0/P_{th} grows, so does the energy of the localized state until it crosses into the band of the linear band-gap spectrum. This is in contrast to dissipative photonic lattice solitons [204] and defect states [205], which have been previously found to exist exclusively in the gaps of the band-gap spectrum. An additional feature of the polariton steady states is transition, with growing pump intensity, from narrow states localized in a vicinity of a single potential well Figure 5.2(a) to broader states with exponentially decaying and spatially modulated tails Figure 5.2(b,c).

To understand the spatial structure of these localized states, we perform the standard Madelung transformation on the condensate wave function, $\Psi(x) = \sqrt{\rho(x)}\exp[i\phi(x)]$, and write down the steady state equations for the condensate density $\Phi(x) = \sqrt{\rho(x)}$ and phase gradient (flow velocity) $v(x) = d\phi(x)/dx$:

$$\begin{gathered}\frac{1}{2}\frac{d^2\Phi}{dx^2} - \left(V_L + g_c\Phi^2 + g_R n_R^0 + \frac{v^2}{2}\right)\Phi + \mu\Phi = 0, \\ \frac{d}{dx}(\Phi^2 v) - (Rn_R^0 - \gamma_c)\Phi^2 = 0,\end{gathered} \tag{5.2}$$

Given the rapid decay of the inhomogeneous pump at large x, we can immediately see that the asymptotic behaviour of the condensate near-linear density away from the pump spot is determined by the combination of the linear periodic potential $V_L(x)$ and a sel-induced effective potential due to the phase gradient, $v^2(x)/2$. These two potentials for the narrow and wide states (a) and (b,c) in Figures 5.1,5.2 are shown in Figure 5.3 (a-c). The strong contribution of the Bloch states from the edges of the Brillouin zone into the composition of the localized state [Figure 5.3(d)] leads to steep spatial gradients of the phase, $\phi(x)$. As a result, the flow of the condensate out of the excitation spot induces a periodic, tight-binding Kronig-Penney-like potential [Figure 5.3(a)], and the band-gap spectrum due to the linear lattice potential becomes of *little relevance* to the energy eigenstates. The sharp peaks of the effective potential are offset from the maxima of the lattice potential, which leads to the fact that the condensate density peaks can coincide with the *maxima* of the lattice potential [see Figure 5.2(a)]. The tunnelling of the condensate out of the excitation spot is strongly inhibited by the tight-binding effective potential, until the

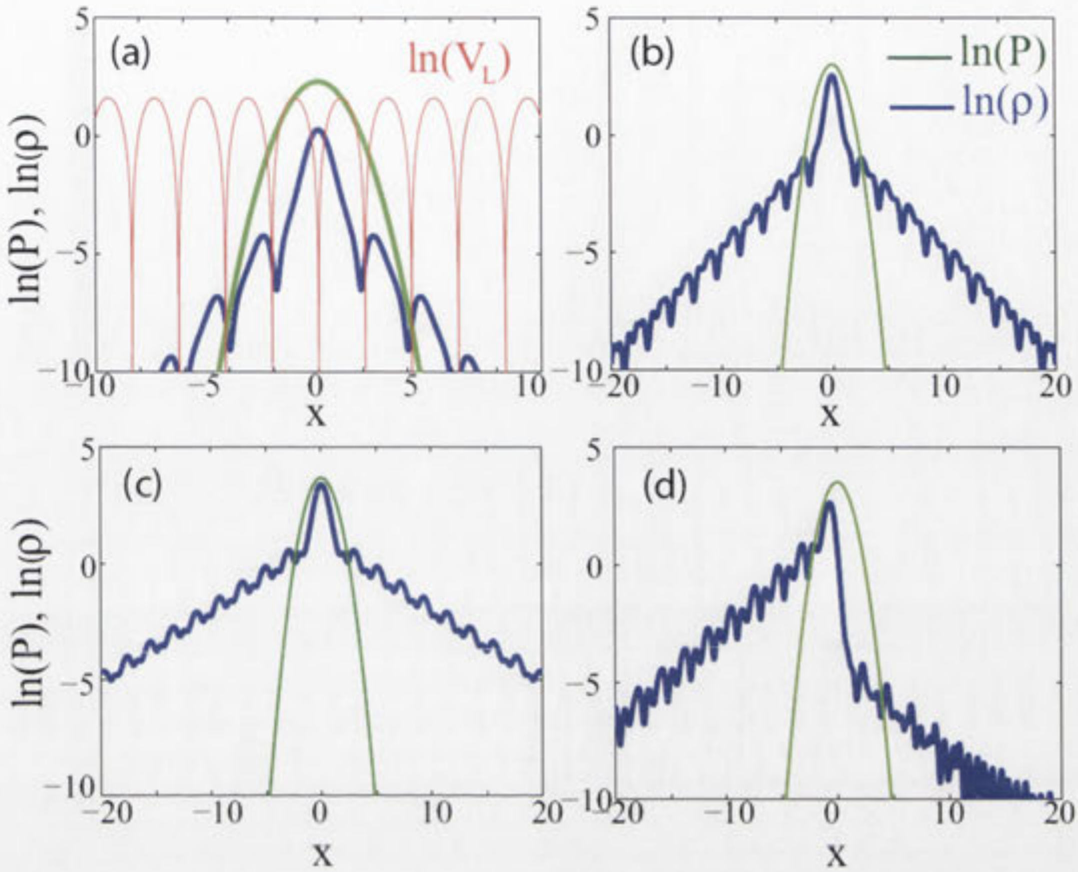

Figure 5.2: Spatial profiles of the condensate density $\ln(\rho(x))$ and pump intensity $\ln(P(x))$ in a periodic 1D lattice potential $V_L(x)$ with $V_0 = 5.0$ and $k_l = 1.5$, corresponding to the peak pump intensity $P_0/P_{th} = 1.27$ [point (a) in Figure 5.1], $P_0/P_{th} = 2.53$ [point (b)], $P_0/P_{th} = 5.06$ [point (c)], and $P_0/P_{th} = 4.30$ [point (d)]. In addition, panel (a) shows the lattice potential $\ln(V_L)$.

modulations of the flow are smoothed out by the stronger pump. As demonstrated in Figures 5.2(b,c) the strongly pumped condensate density then extends over many wells of the periodic potential. We stress that, in contrast to the lattice potential which exists regardless of the condensate formation, the self-induced potential can become physically meaningless far on the "tails" of the condensate [shaded areas in Figure 5.3(a)], where the density is negligible and any dynamical fluctuations can quickly destroy regular phase structure. Although the narrow gap states [Figure 5.2(a)] greatly resemble well localized gap solitons of a conservative BEC [12, 168, 169, 195–197], they have no connection to the Bloch states at the band edge of the first Brillouin zone in the linear lattice potential, rather branching off the linear defect states. Their spatial extent is determined purely by the phase gradients established due to the balance of gain and and loss in the system. The energy of the localized state can lie in either a spectral gap or band of the lattice potential since it is supported by the effective potentials created by the polariton flow.

In the off-site excitation regime, the localized states can also be formed both within gaps and bands of the linear band-gap spectrum of the potential $V_L(x)$ [Figure 5.1], and the threshold for the formation of these states is higher than that of the on-site state. Remarkably, the asymmetry of the defect created by the offset pump translates to the

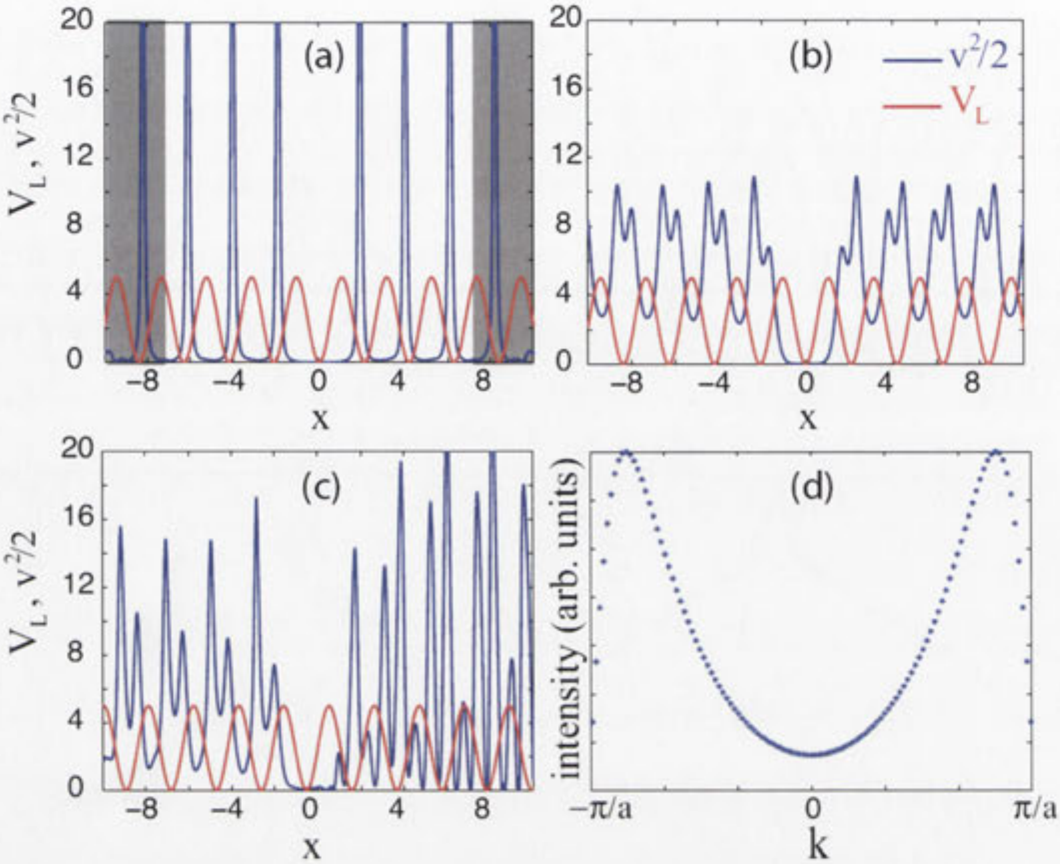

Figure 5.3: Spatial profiles of the lattice potential $V_L(x)$ ($V_0 = 5.0$, $k_l = 1.5$) and the effective linear potential due to the phase gradient $v^2/2$ corresponding to the peak on-site pump intensities (a) $P_0/P_{th} = 1.27$, (b) $P_0/P_{th} = 5.06$, and (c) a non-centered pump ($\pi/4$ off-site) with $P_0/P_{th} = 4.30$. Panel (d) shows the k-space spectrum of the steady state [(a) in Figure 5.2] corresponding to the effective potential in (a).

asymmetry of both the effective potential generated by the polariton flow and the condensate density [Figure 5.2(d) and Figure 5.3(c)]. Such asymmetric localized states are supported by the interface between two different effective potentials, and therefore resemble "mixed-gap" interface states of an atomic BEC in anharmonic lattices [206].

5.3.2 Wide excitation

By fixing the pump intensity and extending the width of the pump spot significantly beyond the single lattice well, we find a variety of spatially extended nearly energy-degenerate localized states. One example of such a gap state and its supporting effective potential is presented in Figures 5.4(a,b). These states strongly resemble "flat gap states" formed by the nonlinearity-induced truncation of nonlinear Bloch states in a conservative condensate [207–209]. However, the localization in this case is due to the effective potential created by the polariton flow out of the finite gain region.

A very wide, locally homogeneous pump near condensation threshold generates extended states that locally resemble a ground state Bloch wave [Figure 5.4(c)] of the linear

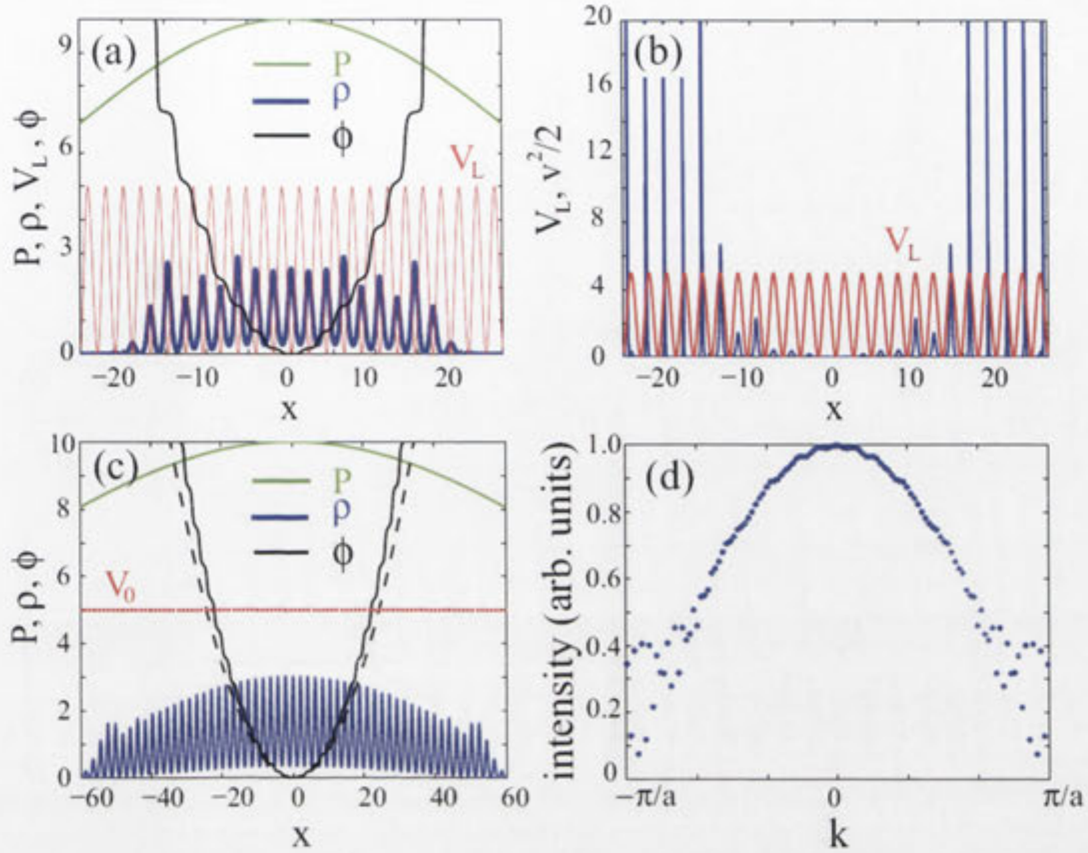

Figure 5.4: (a,c) Spatial profiles of the condensate density $\rho(x)$, phase $\phi(x)$, and lattice potential $V_L(x)$ ($V_0 = 5.0$, $k_l = 1.5$) corresponding to the peak on-site pump intensity $P_0/P_{th} = 1.27$ and widths $\sigma^2 = 6 \times 10^{-4}$ and $\sigma^2 = 6 \times 10^{-5}$, respectively. Dashed curve in (c) is analytical approximation to the phase profile, Equation (5.3). (b) Lattice potential V_L and the effective linear potential $v^2(x)$ corresponding to (a). (d) Spectrum of the state (c) within the first Brillouin zone of the lattice potential.

lattice potential $V_L(x)$. In this regime, the asymptotic approximation of the phase profile at $x \to 0$, derived in [201] for the case of untrapped polariton condensate becomes valid for the most of the excitation region [Figure 5.4(c), dashed line] and the effective potential due to the polariton flow becomes harmonic:

$$v^2(x) \approx \frac{\gamma_c^2}{4} \left[P_0/P_{th} - 1\right]^2 x^2. \tag{5.3}$$

The density profile is a typical ground state supported by the combination of the periodic and harmonic effective potential [Figure 5.4(c)], and its k-space spectrum [Figure 5.4(d)] displays localization around $k = 0$ characteristic of the ground state in the lattice [87]. Thus, in this regime the dissipative condensate in a periodic potential mimics the behaviour of a conservative condensate in the *combined* periodic and harmonic potentials.

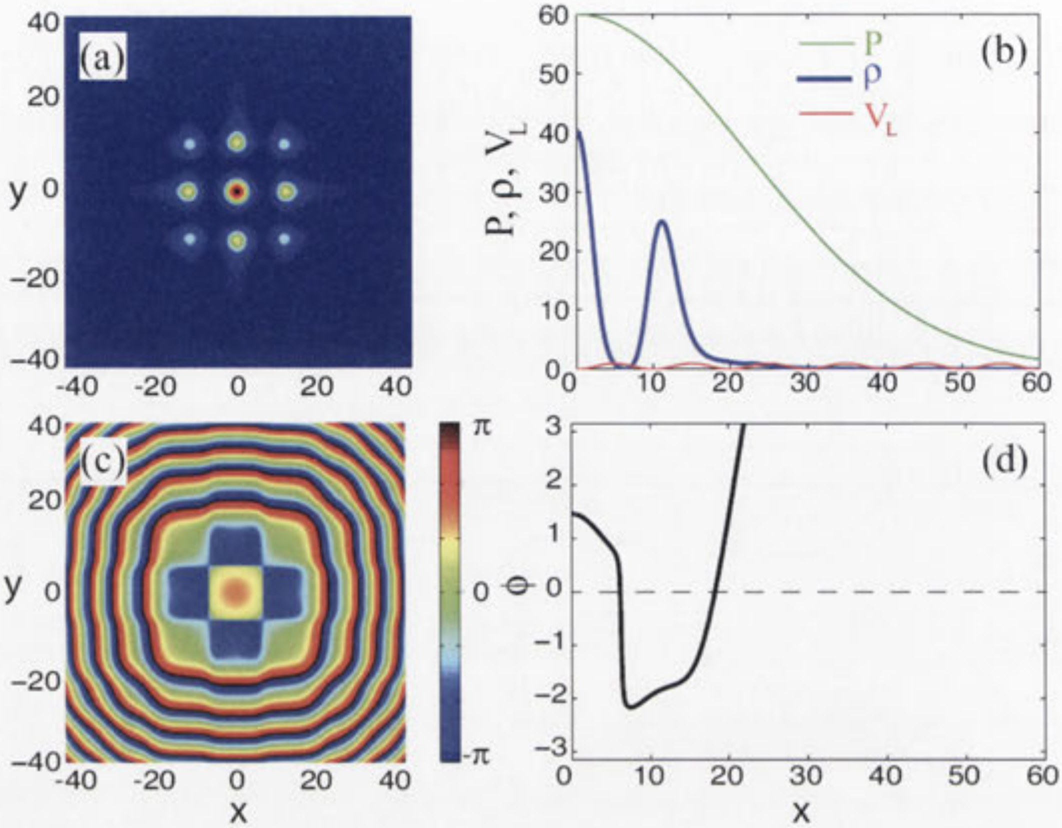

Figure 5.5: Spatial profiles and cross-sections of the (a,b) condensate density and (c,d) phase, corresponding to the narrow gap state in a 2D lattice ($V_0 = 2.0$, $k_l = \pi/4$).

5.4 Localization in 2D

Similarly to the case of 1D periodic potential, we find that narrow and wide excitation spots can create narrow and wide localized steady states of the polariton condensate both in the gaps and bands of the single-particle band-gap spectrum corresponding to a 2D 'square' lattice potential $V_L = V_0[\sin^2(k_l x) + \sin^2(k_l y)]$. Examples of the narrow state density and its phase are shown in Figure 5.5 for the case of a weak lattice. We note that the phase structure displays sharp domain walls associated the strong phase gradients, similar to those in 1D case, which leads to the tight spatial localization of the condensate.

5.5 Concluding remarks

In this chapter we have demonstrated that, under the conditions of spatially inhomogeneous off-resonant CW excitation, a polariton condensate can be spatially localized in a periodic in-plane potential owing to the polariton flows established due to the balance between gain and loss. Periodic potential strongly modulates the velocity of the polariton flow out of the pumping region, and the polaritons become self-trapped in the resulting effective potential. This novel mechanism of localization ensures that, depending on the pump intensity, condensate can be formed and localized both in gaps and bands of the linear single-particle band-gap spectrum of the periodic potential. Localization of the dissipative condensate is therefore irrelevant to the requirement of the negative effective mass which is essential for the gap soliton formation in conservative (atomic) BECs with repulsive interparticle interactions [12, 168, 169, 195–197]. The predicted features of the real-space localization of a dissipative polariton condensate subject to a periodic potential are expected to have strong consequences for any proposed polariton-based devices incorporating modulated potentials, and should be investigated further, both theoretically and experimentally.

Appendix A

Matlab code for solving the GPE numerically in order to study collapse suppression

```
(* ::Package:: *)

clear all;
close all;

aviobj = avifile('mymovie.avi','compression','None');
fout=fopen('data','wt');

%%% spatial grid size and time
N=1024; Lx=200;
tend=200; dt=0.01;
nsteps=tend/dt;

dx=Lx/N; x=-Lx*(1-1/N)/2:dx:Lx*(1-1/N)/2;
kx=[0:N/2-1 -N/2:-1]*2*pi/Lx;
[X, Y]=meshgrid(x, -x); [KX, KY]=meshgrid(kx, kx);
Cen=[]; OMX=[];

%%% initial profile
Nu=4.8; eps=pi/8;
s2=sin(2*eps);c2=cos(2*eps);
p=8/s2/(1+s2^2);
a=(w/s2)*(1-(Nu/8)*s2*(1+s2^2))^(0.25);
sigma = sqrt(1-Nu*s2/8)*cot (2*eps)^2;
om=2*sigma/(a*c2)^2;
T=sigma/a/a/c2;
b=sqrt(2)*a*cos(eps); c=sqrt(2)*a*sin(eps);
A=sqrt (Nu/s2)/a;
U=A*exp(-((X/b).^2+(Y/c).^2)/2 + 1i*T*X.*Y);

%%% boundary condition
sink=0.5*tanh (5.*(X+Lx/2)).*tanh(5.*(Y+Lx/2))+...
     0.5*tanh (5.*(-X+Lx/2)).*tanh(5.*(-Y+Lx/2));
```

```
%%% fast fourier transform
smul=exp(-1i*(KX.^2+KY.^2)*dt);
fftw('planner','estimate');

%%% potential
w=4; Pot=(X.*X+Y.*Y)/w^4;

dum=1;
%%% time, norm, momentum, hamiltonian, amplitude
T=[];P=[];Mom=[];Ham=[];Am=[];

%%% split-step method
for n=1:(nsteps+1)
t=(n-1)*dt;

  U=ifft2(smul.*fft2(U));
  U=U.*exp(1i*(-Pot+abs (U).^2)*dt);
  U=U.*sink;

 if ( n==dum)
  disp(t)
  T=[T; t];
  Int= abs (U).^2;

%%% condition for collape
  half1=abs(U(N/2+3,N/2+3));
  half3=abs(U(N/2-2,N/2+3));
  half2=abs(U(N/2+3,N/2-2));
  half4=abs(U(N/2-2,N/2-2));

  MaxCur2=max (abs(U(:)))/2;
  if (MaxCur2>= half1 || MaxCur2>= half2 || MaxCur2>= half3 || MaxCur2>= hal
     display('Collapse');
     aviobj=close(aviobj);
     return
  end

  Pc=trapz(trapz(Int))*dx*dx;
  P=[P; Pc];
  Ic=4*MaxCur2^2;
  Am=[Am; Ic];
  ImU=imag(U); ReU=real(U);
   [IUx, IUy] = gradient(ImU, dx, -dx);
   [RUx, RUy] = gradient(ReU, dx, -dx);
   FunU = ReU.*(X.*IUy - Y.*IUx) - ImU.*(X.*RUy - Y.*RUx);
   Mc=dx*dx*trapz(trapz(FunU));
   Mom =[Mom; Mc];
```

```
    Hamilt = RUx.^2+RUy.^2+IUx.^2+IUy.^2+Pot.*Int-Int.*Int/2;
    Hc=dx*dx*trapz(trapz(Hamilt));
    Ham = [Ham;Hc];

    fprintf(fout,'%4 .2f %4 .2f %4 .2f %4 .2f %4 .2f \n',...
       [t Ic Pc Mc Hc]);

   hf=figure;
   set(gcf,'Color','w','Position',[300 200 300 300],...
           'Visible','on','PaperUnits','inches');
   set(gca,'Position',[0 0 1 1])
   imagesc(x,x,Int)
   axis([-15 15 -15 15])
   axis square
   axis off
   text(-4,-13,['Time: ' num2str(t,'%4 .1f')],...
       'FontName','TimesNewRoman','FontSize',12,'Color','w')

    aviobj = addframe(aviobj,hf);
    close(hf);
    dum=dum+20;
   end
end;
aviobj=close(aviobj);
fclose(fout);
close all;

figure(1)
plot(T,P/P(1),'*b',T,Mom/Mom(1),'-r',T,Ham/Ham(1),'--g')
figure(2)
plot(T,Am,'-k')
```

.

Bibliography

[1] A. Griffin, "A brief history of our understanding of BEC: From Bose to Beliaev," (1999), vol. 140, pp. 1–13. Varenna Summer School, Italy, Jul 7-17, 1998.

[2] M. Anderson, J. Ensher, M. Matthews, C. Wieman, and E. Cornell, "Observation of Bose-Einstein condensation in a dilute atomic vapor," SCIENCE **269**, 198 (1995).

[3] K. Davis, M. Mewes, M. Andrews, N. Vandruten, D. Durfee, D. Kurn, and W. Ketterle, "Bose-Einstein condensation in a gas of sodium atoms," PHYSICAL REVIEW LETTERS **75**, 3969 (1995).

[4] C. Bradley, C. Sackett, J. Tollett, and R. Hulet, "Evidence od Bose-Einstein Condensation in an atomic gas with attractive interactions," PHYSICAL REVIEW LETTERS **75**, 1687–1690 (1995).

[5] J. Kasprzak, M. Richard, S. Kundermann, A. Baas, P. Jeambrun, J. M. J. Keeling, F. M. Marchetti, M. H. Szymanska, R. Andre, J. L. Staehli, V. Savona, P. B. Littlewood, B. Deveaud, and L. S. Dang, "Bose-Einstein condensation of exciton polaritons," NATURE **443**, 409 (2006).

[6] F. Dalfovo, S. Giorgini, L. Pitaevskii, and S. Stringari, "Theory of Bose-Einstein condensation in trapped gases," REVIEWS OF MODERN PHYSICS **71**, 463 (1999).

[7] G. Roumpos, M. D. Fraser, A. Löffler, S. Höfling, A. Forchel, and Y. Yamamoto, "Single vortex-antivortex pair in an exciton-polariton condensate," NATURE PHYSICS **7**, 129 (2011).

[8] S. Burger, K. Bongs, S. Dettmer, W. Ertmer, K. Sengstock, A. Sanpera, G. Shlyapnikov, and M. Lewenstein, "Dark solitons in Bose-Einstein condensates," PHYSICAL REVIEW LETTERS **83**, 5198 (1999).

[9] J. Denschlag, J. Simsarian, D. Feder, C. Clark, L. Collins, J. Cubizolles, L. Deng, E. Hagley, K. Helmerson, W. Reinhardt, S. Rolston, B. Schneider, and W. Phillips, "Generating solitons by phase engineering of a Bose-Einstein condensate," SCIENCE **287**, 97–101 (2000).

[10] L. Khaykovich, F. Schreck, G. Ferrari, T. Bourdel, J. Cubizolles, L. Carr, Y. Castin, and C. Salomon, "Formation of a matter-wave bright soliton," SCIENCE **296**, 1290 (2002).

[11] K. Strecker, G. Partridge, A. Truscott, and R. Hulet, "Formation and propagation of matter-wave soliton trains," NATURE **417**, 150 (2002).

[12] B. Eiermann, T. Anker, M. Albiez, M. Taglieber, P. Treutlein, K. Marzlin, and M. Oberthaler, "Bright Bose-Einstein gap solitons of atoms with repulsive interaction," PHYSICAL REVIEW LETTERS **92** (2004).

[13] M. Matthews, B. Anderson, P. Haljan, D. Hall, C. Wieman, and E. Cornell, "Vortices in a Bose-Einstein condensate," PHYSICAL REVIEW LETTERS **83**, 2498 (1999).

[14] B. Anderson, P. Haljan, C. Regal, D. Feder, L. Collins, C. Clark, and E. Cornell, "Watching dark solitons decay into vortex rings in a Bose-Einstein condensate," PHYSICAL REVIEW LETTERS **86**, 2926 (2001).

[15] E. Donley, N. Claussen, S. Thompson, and C. Wieman, "Atom-molecule coherence in a Bose-Einstein condensate," NATURE **417**, 529 (2002).

[16] G. Agrawal, *Nonlinear fiber optics* (Academic Press, San Diego, 2001), 3rd ed.

[17] Y. Kivshar and G. Agrawal, *Optical solitons: From fibers to photonic crystals* (Academic press, San Diego, 2003).

[18] A. Leggett, "Topics in the theory of the ultracold dilute alkali gases," MODERN PHYSICS LETTERS B **14**, 1 (2000).

[19] D. Fried, T. Killian, L. Willmann, D. Landhuis, S. Moss, D. Kleppner, and T. Greytak, "Bose-Einstein condensation of atomic hydrogen," PHYSICAL REVIEW LETTERS **81**, 3811 (1998).

[20] M. Andrews, C. Townsend, H. Miesner, D. Durfee, D. Kurn, and W. Ketterle, "Observation of interference between two Bose condensates," SCIENCE **275**, 637 (1997).

[21] K. Bongs, S. Burger, D. Hellweg, M. Kottke, S. Dettmer, T. Rinkleff, L. Cacciapuoti, J. Arlt, K. Sengstock, and W. Ertmer, "Spectroscopy of dark soliton states in Bose-Einstein condensates," JOURNAL OF OPTICS B-QUANTUM AND SEMICLASSICAL OPTICS **5**, S124 (2003).

[22] P. Engels, I. Coddington, P. Haljan, and E. Cornell, "Nonequilibrium effects of anisotropic compression applied to vortex lattices in Bose-Einstein condensates," PHYSICAL REVIEW LETTERS **89** (2002).

[23] B. Anderson and M. Kasevich, "Macroscopic quantum interference from atomic tunnel arrays," SCIENCE **282**, 1686 (1998).

[24] J. Denschlag, J. Simsarian, H. Haffner, C. McKenzie, A. Browaeys, D. Cho, K. Helmerson, S. Rolston, and W. Phillips, "A Bose-Einstein condensate in an optical lattice," JOURNAL OF PHYSICS B-ATOMIC MOLECULAR AND OPTICAL PHYSICS **35** (2002).

[25] E. Cornell and C. Wieman, "Nobel Lecture: Bose-Einstein condensation in a dilute gas, the first 70 years and some recent experiments," REVIEWS OF MODERN PHYSICS **74**, 875 (2002).

[26] D. Durfee and W. Ketterle, "Experimental studies of Bose-Einstein condensation," OPTICS EXPRESS **2**, 299 (1998).

[27] R. Kubo, *Statistical Mechanics* (North-Holland, Amsterdam,1993).

[28] A. Leggett, "Bose-Einstein condensation in the alkali gases: Some fundamental concepts," REVIEWS OF MODERN PHYSICS **73**, 307 (2001).

[29] S. Chu, L. Holloberg, J. Bjorkholm, A. Cable, and A. Ashkin, "Thee dimensional viscous confinement and cooling of atoms by resonance radiation pressure," PHYSICAL REVIEW LETTERS **55**, 48 (1985).

[30] P. Lett, W. Phillips, S. Rolston, C. Tanner, R. Watts, and C. Westbrook, "OPTICAL MOLASSES," JOURNAL OF THE OPTICAL SOCIETY OF AMERICA B-OPTICAL PHYSICS **6**, 2084 (1989).

[31] C. Cohen Tannoudji, "Manipulating atoms with photons," REVIEWS OF MODERN PHYSICS **70**, 707 (1998).

[32] H. Hess, G. Kochanski, J. Doyle, N. Masuhara, D. Kleppner, and T. Greytak, "Magnetic trapping of spin-polarized atomic hydrogen," PHYSICAL REVIEW LETTERS **59**, 672–675 (1987).

[33] G. Askar'yan, "Effects of the gradient of a strong electromagnetic beam on electrons and atoms," SOVIET PHYSICS JETP-USSR **15**, 1088 (1962).

[34] V. Letokhov, "Narrowing of the Doppler width in a standing light wave," JETP LETTERS-USSR **7**, 272 (1968).

[35] A. Ashkin, "Acceleration and trapping of particles by radiation pressure," PHYSICAL REVIEW LETTERS **24**, 156 (1970).

[36] J. Bjorkholm, R. Freeman, A. Ashkin, and D. Pearson, "Observation of focusing of neutral atoms by the dipole forces of resonance-radiation pressure," PHYSICAL REVIEW LETTERS **41**, 1361–1364 (1978).

[37] S. Chu, J. Bjorkholm, A. Ashkin, and A. Cable, "Experimental observation of optically trapped atoms," PHYSICAL REVIEW LETTERS **57**, 314–317 (1986).

[38] R. Grimm, M. Weidemuller, and Y. Ovchinnikov, *Optical dipole traps for neutral atoms*, vol. 42 (2000).

[39] J. Weiner, V. Bagnato, S. Zilio, and P. Julienne, "Experiments and theory in cold and ultracold collisions," REVIEWS OF MODERN PHYSICS **71**, 1–85 (1999).

[40] B. Laud, *Electromagnetics* (New Age International, 1987).

[41] L. P. Pitaevskii and S. Stringari, *Bose-Einstein condensation*, vol. 116 (Clarendon press, 2003).

[42] F. Cattani, A. Kim, M. Lisak, D. Anderson, and Y. Stin, "Interactions of electromagnetic radiation with Bose-Einstein condensates: Manipulating ultra-cold atoms with light," INTERNATINAL JOURNAL OF MODERN PHYSICS B **27**, 1–68 (2013).

[43] C. J. Pethick and H. Smith, *Bose-Einstein condensation in dilute gases* (Cambridge university press, 2002).

[44] G. Grynberg and C. Robilliard, "Cold atoms in dissipative optical lattices," PHYSICS REPORTS-REVIEW SECTION OF PHYSICS LETTERS **355**, 335–451 (2001).

[45] O. Morsch and M. Oberthaler, "Dynamics of Bose-Einstein condensates in optical lattices," REVIEWS OF MODERN PHYSICS **78**, 179 (2006).

[46] O. Morsch, J. Muller, M. Cristiani, D. Ciampini, and E. Arimondo, "Bloch oscillations and mean-field effects of Bose-Einstein condensates in 1D optical lattices," PHYSICAL REVIEW LETTERS **87** (2001).

[47] C. Bradley, C. Sackett, and R. Hulet, "Bose-Einstein condensation of lithium: Observation of limited condensate number," PHYSICAL REVIEW LETTERS **78**, 985 (1997).

[48] V. Perez-Garcia, H. Michinel, and H. Herrero, "Bose-Einstein solitons in highly asymmetric traps," PHYSICAL REVIEW A **57**, 3837 (1998).

[49] N. Zabusku and M. Kruskal, "Interaction of solitons in an collisionless plasma and recurrence of initial states," PHYSICAL REVIEW LETTERS **15**, 240 (1965).

[50] C. Gardner, J. Greene, M. Kruskal, and R. Miura, "Method for solving Korteweg-de Vries equation," PHYSICAL REVIEW LETTERS **19**, 1095 (1967).

[51] V. Zakharov and A. Shabat, "Exact theory of two-dimensional self-focusing and one-dimensional self-modulation of waves in nonlinear media," SOVIET PHYSICS JETP-USSR **34**, 62 (1972).

[52] V. Zakharov and A. Shabat, "Interaction between solutions in a stable medium," SOVIET PHYSICS JETP-USSR **64**, 1627–1639 (1973).

[53] S. Cornish, S. Thompson, and C. Wieman, "Formation of bright matter-wave solitons during the collapse of attractive Bose-Einstein condensates," PHYSICAL REVIEW LETTERS **96** (2006).

[54] E. Donley, N. Claussen, S. Cornish, J. Roberts, E. Cornell, and C. Wieman, "Dynamics of collapsing and exploding Bose-Einstein condensates," NATURE **412**, 295–299 (2001).

[55] M. Berry, "Making waves in physics," NATURE **403**, 21 (2000).

[56] L. M. Pismen, *Vortices in nonlinear fields: From liquid crystals to superfluids, from non-equilibrium patterns to cosmic strings*, vol. 100 (Oxford University Press, 1999).

[57] J. Williams and M. Holland, "Preparing topological states of a Bose-Einstein condensate," NATURE **401**, 568–572 (1999).

[58] K. Madison, F. Chevy, W. Wohlleben, and J. Dalibard, "Vortex formation in a stirred Bose-Einstein condensate," PHYSICAL REVIEW LETTERS **84**, 806–809 (2000).

[59] C. Raman, J. Abo-Shaeer, J. Vogels, K. Xu, and W. Ketterle, "Vortex nucleation in a stirred Bose-Einstein condensate," PHYSICAL REVIEW LETTERS **87**, 210402 (2001).

[60] S. Ghosh, "Vortices in atomic Bose-Einstein condensates: an introduction," PHASE TRANSITIONS **77**, 625 (2004).

[61] P. Ruprecht, M. Holland, K. Burnett, and M. Edwards, "Time-dependent solution of the nonlinear Schrödinger equation for Bose condensed trapped neutral atoms," PHYSICAL REVIEW A **51**, 4704–4711 (1995).

[62] J. Gerton, D. Strekalov, I. Prodan, and R. Hulet, "Direct observation of growth and collapse of a Bose-Einstein condensate with attractive interactions," NATURE **408**, 692–695 (2000).

[63] A. Gammal, L. Tomio, and T. Frederico, "Critical numbers of attractive Bose-Einstein condensed atoms in asymmetric traps," PHYSICAL REVIEW A **66** (2002).

[64] L. Pitaevskii, "Dynamics of collapse of a confined Bose gas," PHYSICS LETTERS A **221**, 14–18 (1996).

[65] L. Santos and G. Shlyapnikov, "Collapse dynamics of trapped Bose-Einstein condensates," PHYSICAL REVIEW A **66** (2002).

[66] M. Ueda and H. Saito, "A Consistent Picture of a Collapsing Bose-Einstein Condensate," JOURNAL OF THE PHYSICAL SOCIETY OF JAPAN **72SC**, 127–133 (2003).

[67] M. Wadati and T. Tsurumi, "Ground State of a Bose-Einstein Condensate under Axially Symmetric Magnetic Trap," JOURNAL OF THE PHYSICAL SOCIETY OF JAPAN **68**, 3840–3847 (1999).

[68] J. Roberts, N. Claussen, S. Cornish, E. Donley, E. Cornell, and C. Wieman, "Controlled collapse of a Bose-Einstein condensate," PHYSICAL REVIEW LETTERS **86**, 4211–4214 (2001).

[69] J. M. Blatt, K. Böer, and W. Brandt, "Bose-Einstein condensation of excitons," PHYSICAL REVIEW **126**, 1691 (1962).

[70] Y. Yamamoto, S. Machida, and G. Björk, "Microcavity semiconductor laser with enhanced spontaneous emission," PHYSICAL REVIEW A **44**, 657 (1991).

[71] Y. Yamamoto, F. Matinaga, S. Machida, A. Karlsson, J. Jacobson, G. Björk, and T. Mukai, "Quantum electrodynamic effects in semiconductor microcavities-Microlasers and coherent exciton-polariton emission," LE JOURNAL DE PHYSIQUE IV **3**, C5–39 (1993).

[72] A. Imamog, R. Ram, S. Pau, Y. Yamamoto *et al.*, "Nonequilibrium condensates and lasers without inversion: Exciton-polariton lasers," Physical Review A **53**, 4250 (1996).

[73] A. Amo, S. Pigeon, D. Sanvitto, V. G. Sala, R. Hivet, I. Carusotto, F. Pisanello, G. Lemenager, R. Houdre, E. Giacobino, C. Ciuti, and A. Bramati, "Polariton Superfluids Reveal Quantum Hydrodynamic Solitons," SCIENCE **332**, 1167–1170 (2011).

[74] K. G. Lagoudakis, M. Wouters, M. Richard, A. Baas, I. Carusotto, R. Andre, L. E. S. I. Dang, and B. Deveaud-Pledran, "Quantized vortices in an exciton-polariton condensate," NATURE PHYSICS **4**, 706–710 (2008).

[75] Y. E. Lozovik and V. Yudson, "A new mechanism for superconductivity: pairing between spatially separated electrons and holes," ZHURNAL EKSPERIMENTALNOI I TEORETICHESKOI FIZIKI **71**, 738–753 (1976).

[76] S. Shevchenko, "Theory of superconductivity of systems with pairing of spatially separated electrons and holes," SOVIET JOURNAL OF LOW TEMPERATURE PHYSICS **2** (1976).

[77] E. Hanamura and H. Haug, "Condensation effects of excitons," PHYSICS REPORTS **33**, 209–284 (1977).

[78] H. Deng, H. Haug, and Y. Yamamoto, "Exciton-polariton Bose-Einstein condensation," REVIEWS OF MODERN PHYSICS **82**, 1489 (2010).

[79] V. Savona, Z. Hradil, A. Quattropani, and P. Schwendimann, "Quantum theory of quantum-well polaritons in semiconductor microcavities," PHYSICAL REVIEW B **49**, 8774 (1994).

[80] H. Deng, G. Weihs, C. Santori, J. Bloch, and Y. Yamamoto, "Condensation of semiconductor microcavity exciton polaritons," SCIENCE **298**, 199–202 (2002).

[81] J. Hopfield, "Theory of the contribution of excitons to the complex dielectric constant of crystals," PHYSICAL REVIEW **112**, 1555 (1958).

[82] R. Balili, V. Hartwell, D. Snoke, L. Pfeiffer, and K. West, "Bose-Einstein condensation of microcavity polaritons in a trap," SCIENCE **316**, 1007–1010 (2007).

[83] S. Christopoulos, G. B. H. Von Högersthal, A. Grundy, P. Lagoudakis, A. Kavokin, J. Baumberg, G. Christmann, R. Butté, E. Feltin, J.-F. Carlin *et al.*, "Room-temperature polariton lasing in semiconductor microcavities," PHYSICAL REVIEW LETTERS **98**, 126405 (2007).

[84] A. Bramati, *Physics of Quantum Fluids: New Trends and Hot Topics in Atomic and Polariton Condensates*, vol. 177 (Springer, 2013).

[85] R. Houdré, C. Weisbuch, R. Stanley, U. Oesterle, and M. Ilegems, "Nonlinear emission of semiconductor microcavities in the strong coupling regime," PHYSICAL REVIEW LETTERS **85**, 2793 (2000).

[86] R. Stevenson, V. Astratov, M. Skolnick, D. Whittaker, M. Emam-Ismail, A. Tartakovskii, P. Savvidis, J. Baumberg, and J. Roberts, "Continuous wave observation of massive polariton redistribution by stimulated scattering in semiconductor microcavities," PHYSICAL REVIEW LETTERS **85**, 3680 (2000).

[87] C. W. Lai, N. Y. Kim, S. Utsunomiya, G. Roumpos, H. Deng, M. D. Fraser, T. Byrnes, P. Recher, N. Kumada, T. Fujisawa, and Y. Yamamoto, "Coherent zero-state and p-state in an exciton-polariton condensate array," NATURE **450**, 529 (2007).

[88] S. Utsunomiya, L. Tian, G. Roumpos, C. Lai, N. Kumada, T. Fujisawa, M. Kuwata-Gonokami, A. Löffler, S. Höfling, A. Forchel *et al.*, "Observation of Bogoliubov excitations in exciton-polariton condensates," NATURE PHYSICS **4**, 700–705 (2008).

[89] N. Y. Kim, K. Kusudo, C. Wu, N. Masumoto, A. Löffler, S. Höfling, N. Kumada, L. Worschech, A. Forchel, and Y. Yamamoto, "Dynamical d-wave condensation of exciton-polaritons in a two-dimensional square-lattice potential," NATURE PHYSICS **7**, 681 (2011).

[90] O. El Daïf, A. Baas, T. Guillet, J.-P. Brantut, R. I. Kaitouni, J.-L. Staehli, F. Morier-Genoud, and B. Deveaud, "Polariton quantum boxes in semiconductor microcavities," APPLIED PHYSICS LETTERS **88**, 061105 (2006).

[91] F. Cataliotti, S. Burger, C. Fort, P. Maddaloni, F. Minardi, A. Trombettoni, A. Smerzi, and M. Inguscio, "Josephson junction arrays with Bose-Einstein condensates," SCIENCE **293**, 843–846 (2001).

[92] M. Wouters and I. Carusotto, "Excitations in a nonequilibrium Bose-Einstein condensate of exciton polaritons," PHYSICAL REVIEW LETTERS **99** (2007).

[93] A. D. Cronin, J. Schmiedmayer, and D. E. Pritchard, "Optics and interferometry with atoms and molecules," REVIEWS OF MODERN PHYSICS **81**, 1051–1129 (2009).

[94] M. Nest, Y. Japha, R. Folman, and R. Kosloff, "Dynamic matter-wave pulse shaping," PHYSICAL REVIEW A **81** (2010).

[95] R. Folman, P. Kruger, J. Schmiedmayer, J. Denschlag, and C. Henkel, "Microscopic atom optics: From wires to an atom chip," in "ADVANCES IN ATOMIC, MOLECULAR, AND OPTICAL PHYSICS, VOL 48," , vol. 48 of *Advances In Atomic Molecular and Optical Physics*, Bederson, B and Walther, H, ed. (2002), p. 263.

[96] M. Greiner, I. Bloch, T. Hansch, and T. Esslinger, "Magnetic transport of trapped cold atoms over a large distance," PHYSICAL REVIEW A **63** (2001).

[97] H. Lewandowski, D. Harber, D. Whitaker, and E. Cornell, "Observation of anomalous spin-state segregation in a trapped ultracold vapor," PHYSICAL REVIEW LETTERS **88** (2002).

[98] T. Gustavson, A. Chikkatur, A. Leanhardt, A. Gorlitz, S. Gupta, D. Pritchard, and W. Ketterle, "Transport of Bose-Einstein condensates with optical tweezers," PHYSICAL REVIEW LETTERS **88** (2002).

[99] M. Kasevich and S. Chu, "Atomic interferometry using stimulated Raman transitions," PHYSICAL REVIEW LETTERS **67**, 181–184 (1991).

[100] S. Potting, M. Cramer, C. Schwalb, H. Pu, and P. Meystre, "Coherent acceleration of Bose-Einstein condensates," PHYSICAL REVIEW A **64** (2001).

[101] M. BenDahan, E. Peik, J. Reichel, Y. Castin, and C. Salomon, "Bloch oscillations of atoms in an optical potential," PHYSICAL REVIEW LETTERS **76**, 4508–4511 (1996).

[102] S. Kuhr, W. Alt, D. Schrader, M. Muller, V. Gomer, and D. Meschede, "Deterministic delivery of a single atom," SCIENCE **293**, 278 (2001).

[103] O. Mandel, M. Greiner, A. Widera, T. Rom, T. Hansch, and I. Bloch, "Coherent transport of neutral atoms in spin-dependent optical lattice potentials," PHYSICAL REVIEW LETTERS **91** (2003).

[104] S. Schmid, G. Thalhammer, K. Winkler, F. Lang, and J. H. Denschlag, "Long distance transport of ultracold atoms using a 1D optical lattice," NEW JOURNAL OF PHYSICS **8** (2006).

[105] D. Poletti, T. J. Alexander, E. A. Ostrovskaya, B. Li, and Y. S. Kivshar, "Dynamics of Matter-Wave Solitons in a Ratchet Potential," PHYSICAL REVIEW LETTERS **101** (2008).

[106] T. Salger, S. Kling, T. Hecking, C. Geckeler, L. Morales-Molina, and M. Weitz, "Directed Transport of Atoms in a Hamiltonian Quantum Ratchet," SCIENCE **326**, 1241 (2009).

[107] R. Scharf and A. Bishop, "Length-scale competition for the one-dimensional nonlinear schrödinger equation with spatially periodic potentials," PHYSICAL REVIEW E **47**, 1375 (1993).

[108] G. Burlak and B. A. Malomed, "Dynamics of matter-wave solitons in a time-modulated two-dimensional optical lattice," PHYSICAL REVIEW A **77** (2008).

[109] G. Montesinos, V. Perez-Garcia, and H. Michinel, "Stabilized two-dimensional vector solitons," PHYSICAL REVIEW LETTERS **92** (2004).

[110] P. Pedri and L. Santos, "Two-dimensional bright solitons in dipolar Bose-Einstein condensates," PHYSICAL REVIEW LETTERS **95** (2005).

[111] B. Baizakov, B. Malomed, and M. Salerno, "Multidimensional solitons in periodic potentials," EUROPHYSICS LETTERS **63**, 642–648 (2003).

[112] B. A. Malomed, *Soliton management in periodic systems* (Springer New York, 2006).

[113] O. M. Braun and Y. S. Kivshar, *The Frenkel-Kontorova model: concepts, methods, and applications* (Springer Verlag, 2004).

[114] Y. S. Kivshar and G. Agrawal, *Optical solitons: from fibers to photonic crystals* (Academic Press, 2003).

[115] L. Hadzievski, A. Maluckov, M. Stepic, and D. Kip, "Power controlled soliton stability and steering in lattices with saturable nonlinearity," PHYSICAL REVIEW LETTERS **93** (2004).

[116] T. R. O. Melvin, A. R. Champneys, P. G. Kevrekidis, and J. Cuevas, "Radiationless traveling waves in saturable nonlinear Schrodinger lattices," PHYSICAL REVIEW LETTERS **97** (2006).

[117] H. Susanto, P. G. Kevrekidis, R. Carretero-Gonzalez, B. A. Malomed, and D. J. Frantzeskakis, "Mobility of discrete solitons in quadratically nonlinear media," PHYSICAL REVIEW LETTERS **99** (2007).

[118] H. Lignier, C. Sias, D. Ciampini, Y. Singh, A. Zenesini, O. Morsch, and E. Arimondo, "Dynamical control of matter-wave tunneling in periodic potentials," PHYSICAL REVIEW LETTERS **99** (2007).

[119] T. Mayteevarunyoo and B. A. Malomed, "Gap solitons in rocking optical lattices and waveguides with undulating gratings," PHYSICAL REVIEW A **80** (2009).

[120] B. Baizakov, B. Malomed, and M. Salerno, "Multidimensional solitons in a low-dimensional periodic potential," PHYSICAL REVIEW A **70** (2004).

[121] S. Burger, F. Cataliotti, C. Fort, P. Maddaloni, F. Minardi, and M. Inguscio, "Quasi-2D Bose-Einstein condensation in an optical lattice," EUROPHYSICS LETTERS **57**, 1–6 (2002).

[122] G. Grynberg, B. Lounis, P. Verkerk, J.-Y. Courtois, and C. Salomon, "Quantized motion of cold cesium atoms in two-and three-dimensional optical potentials," PHYSICAL REVIEW LETTERS **70**, 2249 (1993).

[123] J. Sebby-Strabley, M. Anderlini, P. Jessen, and J. Porto, "Lattice of double wells for manipulating pairs of cold atoms," PHYSICAL REVIEW A **73** (2006).

[124] J. Yang and T. I. Lakoba, "Universally-convergent squared-operator iteration methods for solitary waves in general nonlinear wave equations," STUDIES IN APPLIED MATHEMATICS **118**, 153 (2007).

[125] B. Baizakov, V. Konotop, and M. Salerno, "Regular spatial structures in arrays of Bose-Einstein condensates induced by modulational instability," JOURNAL OF PHYSICS B-ATOMIC MOLECULAR AND OPTICAL PHYSICS **35**, 5105–5119 (2002).

[126] N. Vakhitov and A. Kolokolov, "Stability of stationary solutions of nonlinear wave equations," Radiophys. Quantum Electron **16**, 783 (1975).

[127] L. Berge and J. Rasmussen, "Collapsing dynamics of attractive Bose-Einstein condensates," PHYSICS LETTERS A **304**, 136–142 (2002).

[128] M. Karlsson, D. Anderson, and M. Desaix, "Dynamics of self focusing and self-phase modulation in a parabolic index optical fiber," OPTICS LETTERS **17**, 22–24 (1992).

[129] J. Manassa, "Collapse of the two dimensional spatial soliton in a parabolic index material," OPTICS LETTERS **17**, 1259 (1992).

[130] L. Berge, "Self-focusing dynamics of nonlinear waves in media with parabolic-type inhomogeneities," PHYSICS OF PLASMAS **4**, 1227 (1997).

[131] T. Alexander and L. Berge, "Ground states and vortices of matter-wave condensates and optical guided waves," PHYSICAL REVIEW E **65** (2002).

[132] S. Longhi, "Modulational instability and space-time dynamics in nonlinear parabolic-index optical fibers," OPTICS LETTERS **28**, 2363 (2003).

[133] S. Longhi and D. Janner, "Self-focusing and nonlinear periodic beams in parabolic index optical fibres," JOURNAL OF OPTICS B-QUANTUM AND SEMICLASSICAL OPTICS **6**, S303 (2004).

[134] S. Wüster, B. J. Dabrowska-Wüster, A. S. Bradley, M. J. Davis, P. B. Blakie, J. J. Hope, and C. M. Savage, "Quantum depletion of collapsing Bose-Einstein condensates," PHYSICAL REVIEW A **75** (2007).

[135] A. Parola, L. Salasnich, and L. Reatto, "Structure and stability of bosonic clouds: Alkaki-metal atoms with negative scattering length," PHYSICAL REVIEW A **57**, R3180 (1998).

[136] V. Perez-Garcia, V. Konotop, and J. Garcia-Ripoll, "Dynamics of quasicollapse in nonlinear Schrödinger systems with nonlocal interactions," PHYSICAL REVIEW E **62**, 4300 (2000).

[137] A. Bulgac, "Dilute quantum droplets," PHYSICAL REVIEW LETTERS **89** (2002).

[138] A. Gammal, T. Frederico, L. Tomio, and P. Chomaz, "Liquid-gas phase transition in Bose-Einstein condensates with time evolution," PHYSICAL REVIEW A **61** (2000).

[139] H. Hammer and D. Son, "Universal properties of two-dimensional Boson droplets," PHYSICAL REVIEW LETTERS **93** (2004).

[140] S. Adhikari, "Collapse of attractive Bose-Einstein condensed vortex states in a cylindrical trap," PHYSICAL REVIEW E **65** (2002).

[141] M. C. Tsatsos, A. I. Streltsov, O. E. Alon, and L. S. Cederbaum, "Fragmented many-body states of definite angular momentum and stability of attractive three-dimensional condensates," PHYSICAL REVIEW A **82** (2010).

[142] L. Allen, S. Barnett, and M. Padgett, *Orbital Angular Momentum* (2003).

[143] A. Desyatnikov, Y. Kivshar, and L. Torner, "Optical vortices and vortex solitons," in "PROGRESS IN OPTICS, VOL 47," , vol. 47 of *Progress in Optics*, Wolf, E, ed. (2005), pp. 291–391.

[144] L. Vuong, T. Grow, A. Ishaaya, A. Gaeta, G. 't Hooft, E. Eliel, and G. Fibich, "Collapse of optical vortices," PHYSICAL REVIEW LETTERS **96** (2006).

[145] V. Yukalov and E. Yukalova, "Optimal trap shape for a Bose gas with attractive interactions," PHYSICAL REVIEW A **72** (2005).

[146] F. Haas, "Anisotropic Bose-Einstein condensates and completely integrable dynamical systems," PHYSICAL REVIEW A **65** (2002).

[147] A. Goncharenko, Y. Logvin, A. Samson, and P. Shapovalov, "Rotating elliptic Gaussian beams in nonlinear media," OPTICS COMMUNICATIONS **81**, 225 (1991).

[148] A. Goncharenko, Y. Logvin, A. Samson, P. Shapovalov, and S. Turovets, "Ermakov Hamiltonian systems in nonlinear optics of elliptic Gaussian beams," PHYSICS LETTERS A **160**, 138 (1991).

[149] A. S. Desyatnikov, D. Buccoliero, M. R. Dennis, and Y. S. Kivshar, "Suppression of Collapse for Spiraling Elliptic Solitons," PHYSICAL REVIEW LETTERS **104** (2010).

[150] R. W. Boyd, S. G. Lukishova, and Y. Shen, *Self-focusing: Past and Present: Fundamentals and Prospects*, vol. 114 (Springer, 2008).

[151] A. Collin, E. Lundh, and K. Suominen, "Center-of-mass rotation and vortices in an attractive Bose gas," PHYSICAL REVIEW A **71** (2005).

[152] A. Collin, "Collective modes and the broken symmetry of a rotating attractive Bose gas in an anharmonic trap," PHYSICAL REVIEW A **73** (2006).

[153] T. Ghosh, "Vortex formation in a fast rotating Bose-Einstein condensate," PHYSICAL REVIEW A **69** (2004).

[154] T. Ghosh, "Vortex formation in a slowly rotating Bose-Einstein condensate confined in a harmonic-plus-Gaussian laser trap," EUROPEAN PHYSICAL JOURNAL D **31**, 101 (2004).

[155] J. Tabosa and D. Petrov, "Optical pumping of orbital angular momentum of light in cold cesium atoms," PHYSICAL REVIEW LETTERS **83**, 4967 (1999).

[156] M. F. Andersen, C. Ryu, P. Clade, V. Natarajan, A. Vaziri, K. Helmerson, and W. D. Phillips, "Quantized rotation of atoms from photons with orbital angular momentum," PHYSICAL REVIEW LETTERS **97** (2006).

[157] S. Thanvanthri, K. T. Kapale, and J. P. Dowling, "Arbitrary coherent superpositions of quantized vortices in Bose-Einstein condensates via orbital angular momentum of light," PHYSICAL REVIEW A **77** (2008).

[158] J. Courtial, K. Dholakia, L. Allen, and M. Padgett, "Gaussian beams with very high orbital angular momentum," OPTICS COMMUNICATIONS **144**, 210 (1997).

[159] B. Malomed, "Variational methods in nonlinear fiber optics and related fields," in "PROGRESS IN OPTICS, VOLUME 43," , vol. 43 of *Progress in Optics*, Wolf, E, ed. (Elsevier Science BV, 2002), pp. 71–193.

[160] M. Desaix, D. Anderson, and M. Lisak, "Variational approach to collapse of optical pulses," JOURNAL OF THE OPTICAL SOCIETY OF AMERICA B-OPTICAL PHYSICS **8**, 2082–2086 (1991).

[161] Y. Silberberg, "Collapse of optical pulses," OPTICS LETTERS **15**, 1282–1284 (1990).

[162] R. Chiao, E. Garmire, and C. Townes, "Self-trapping of optical beams," PHYSICAL REVIEW LETTERS **13**, 479–& (1964).

[163] K. Moll, A. Gaeta, and G. Fibich, "Self-similar optical wave collapse: Observation of the Townes profile," PHYSICAL REVIEW LETTERS **90** (2003).

[164] G. Nardin, G. Grosso, Y. Leger, B. Pietka, F. Morier-Genoud, and B. Deveaud-Pledran, "Hydrodynamic nucleation of quantized vortex pairs in a polariton quantum fluid," NATURE PHYSICS **7**, 635 (2011).

[165] O. A. Egorov, A. V. Gorbach, F. Lederer, and D. V. Skryabin, "Two-Dimensional Localization of Exciton Polaritons in Microcavities," PHYSICAL REVIEW LETTERS **105** (2010).

[166] M. Sich, D. N. Krizhanovskii, M. S. Skolnick, A. V. Gorbach, R. Hartley, D. V. Skryabin, E. A. Cerda-Mendez, K. Biermann, R. Hey, and P. V. Santos, "Observation of bright polariton solitons in a semiconductor microcavity," NATURE PHOTONICS **6**, 50 (2012).

[167] N. N. Rosanov, "Dissipative polariton solitons: Proof of existence," NATURE PHOTONICS **6**, 6 (2012).

[168] H. Pu, L. Baksmaty, W. Zhang, N. Bigelow, and P. Meystre, "Effective-mass analysis of Bose-Einstein condensates in optical lattices: Stabilization and levitation," PHYSICAL REVIEW A **67** (2003).

[169] E. Ostrovskaya and Y. Kivshar, "Photonic crystals for matter waves: Bose-Einstein condensates in optical lattices," OPTICS EXPRESS **12**, 19 (2004).

[170] A. Siegman, "Propagating modes in gain-guided optical fibers," JOURNAL OF THE OPTICAL SOCIETY OF AMERICA A-OPTICS IMAGE SCIENCE AND VISION **20**, 1617 (2003).

[171] D. A. Zezyulin, Y. V. Kartashov, and V. V. Konotop, "Solitons in a medium with linear dissipation and localized gain," OPTICS LETTERS **36**, 1200 (2011).

[172] A. Fetter and A. Svidzinsky, "Vortices in a trapped dilute Bose-Einstein condensate," JOURNAL OF PHYSICS-CONDENSED MATTER **13**, R135 (2001).

[173] M. Wouters, I. Carusotto, and C. Ciuti, "Spatial and spectral shape of inhomogeneous nonequilibrium exciton-polariton condensates," PHYSICAL REVIEW B **77** (2008).

[174] A. Desyatnikov, Y. Kivshar, and L. Torner, "Optical vortices and vortex solitons," (ELSEVIER SCIENCE BV, 2005), p. 291.

[175] N. Rozanov, S. Fedorov, and A. Shatsev, "Energy-flow patterns and bifurcations of two-dimensional cavity solitons," JOURNAL OF EXPERIMENTAL AND THEORETICAL PHYSICS **98**, 427 (2004).

[176] M. Edwards and K. Burnett, "Numerical solution of the nonlinear Schrödinger equation for small samples of trapped neutral atoms," PHYSICAL REVIEW A **51**, 1382 (1995).

[177] A. Ankiewicz, N. Devine, N. Akhmediev, and J. M. Soto-Crespo, "Continuously self-focusing and continuously self-defocusing two-dimensional beams in dissipative media," PHYSICAL REVIEW A **77** (2008).

[178] J. Keeling and N. G. Berloff, "Spontaneous rotating vortex lattices in a pumped decaying condensate," PHYSICAL REVIEW LETTERS **100** (2008).

[179] Y. Kivshar, T. Alexander, and S. Turitsyn, "Nonlinear modes of a macroscopic quantum oscillator," PHYSICS LETTERS A **278**, 225 (2001).

[180] V. E. Lobanov, Y. V. Kartashov, V. A. Vysloukh, and L. Torner, "Stable radially symmetric and azimuthally modulated vortex solitons supported by localized gain," OPTICS LETTERS **36**, 85 (2011).

[181] A. Sergeev and V. Petviashvili, "Spiral Solitons in active media with excitation thresholds," DOKLADY AKADEMII NAUK SSSR **276**, 1380 (1984).

[182] L. Crasovan, B. Malomed, and D. Mihalache, "Stable vortex solitons in the two-dimensional Ginzburg-Landau equation," PHYSICAL REVIEW E **63** (2001).

[183] P. Fedichev and G. Shlyapnikov, "Dissipative dynamics of a vortex state in a trapped Bose-condensed gas," PHYSICAL REVIEW A **60**, R1779 (1999).

[184] F. Manni, K. G. Lagoudakis, T. C. H. Liew, R. Andre, and B. Deveaud-Pledran, "Spontaneous Pattern Formation in a Polariton Condensate," PHYSICAL REVIEW LETTERS **107** (2011).

[185] G. Tosi, G. Christmann, N. G. Berloff, P. Tsotsis, T. Gao, Z. Hatzopoulos, P. G. Savvidis, and J. J. Baumberg, "Sculpting oscillators with light within a nonlinear quantum fluid," NATURE PHYSICS **8**, 190 (2012).

[186] I. Bloch, "Exploring quantum matter with ultracold atoms in optical lattices," JOURNAL OF PHYSICS B-ATOMIC MOLECULAR AND OPTICAL PHYSICS **38**, S629 (2005).

[187] M. Lewenstein, A. Sanpera, and V. Ahufinger, *Ultracold Atoms in Optical Lattices: Simulating quantum many-body systems* (OUP Oxford, 2012).

[188] D. Sanvitto and V. Timofeev, "Exciton polaritons in microcavities: New frontiers," SPRINGER SER. SOLID-STATE SCI **172** (2012).

[189] N. Masumoto, N. Y. Kim, T. Byrnes, K. Kusudo, A. Löffler, S. Höfling, A. Forchel, and Y. Yamamoto, "Exciton-polariton condensates with flat bands in a two-dimensional kagome lattice," NEW JOURNAL OF PHYSICS **14** (2012).

[190] D. Tanese, H. Flayac, D. Solnyshkov, A. Amo, A. Lemaitre, E. Galopin, R. Braive, P. Senellart, I. Sagnes, G. Malpuech, and J. Bloch, "Polaritons in a 1D periodic potential: condensation in gap states," Proceedings of the PLMCN12 Conference (2012).

[191] E. A. Cerda-Mendez, D. N. Krizhanovskii, M. Wouters, R. Bradley, K. Biermann, K. Guda, R. Hey, P. V. Santos, D. Sarkar, and M. S. Skolnick, "Polariton condensation in dynamic acoustic lattices," PHYSICAL REVIEW LETTERS **105** (2010).

[192] E. A. Cerda-Mendez, D. N. Krizhanovskii, K. Biermann, R. Hey, M. S. Skolnick, and P. V. Santos, "Wavefunction of polariton condensates in a tunable acoustic lattice," NEW JOURNAL OF PHYSICS **14** (2012).

[193] W. Chen and D. L. Mills, "Gap solitons and the nonlinear optical response of superlattices," PHYSICAL REVIEW LETTERS **58**, 160 (1987).

[194] C. M. de Sterke and J. E. Sipe, "Envelope-function approach for the electrodynamics of nonlinear periodic structures," PHYSICS REVIEW A **38**, 5149 (1988).

[195] T. Anker, M. Albiez, B. Eiermann, M. Taglieber, and M. Oberthaler, "Linear and nonlinear dynamics of matter wave packets in periodic potentials," OPTICS EXPRESS **12**, 11 (2004).

[196] P. Louis, E. Ostrovskaya, C. Savage, and Y. Kivshar, "Bose-Einstein condensates in optical lattices: Band-gap structure and solitons," PHYSICAL REVIEW A **67** (2003).

[197] N. Efremidis and D. Christodoulides, "Lattice solitons in Bose-Einstein condensates," PHYSICAL REVIEW A **67** (2003).

[198] A. V. Gorbach, B. A. Malomed, and D. V. Skryabin, "Gap polariton solitons," PHYSICS LETTERS A **373**, 3024 (2009).

[199] T. Byrnes, P. Recher, and Y. Yamamoto, "Mott transitions of exciton polaritons and indirect excitons in a periodic potential," PHYSICAL REVIEW B **81** (2010).

[200] G. Roumpos, W. H. Nitsche, S. Höfling, A. Forchel, and Y. Yamamoto, "Gain-induced trapping of microcavity exciton-polariton condensates," PHYSICAL REVIEW LETTERS **104** (2010).

[201] E. A. Ostrovskaya, J. Abdullaev, A. S. Desyatnikov, M. D. Fraser, and Y. S. Kivshar, "Dissipative solitons and vortices in polariton Bose-Einstein condensates," PHYSICAL REVIEW A **86** (2012).

[202] E. Wertz, L. Ferrier, D. D. Solnyshkov, R. Johne, D. Sanvitto, A. Lemaitre, I. Sagnes, R. Grousson, A. V. Kavokin, P. Senellart, G. Malpuech, and J. Bloch, "Spontaneous formation and optical manipulation of extended polariton condensates," NATURE PHYSICS **6**, 860 (2010).

[203] N. Akhmediev and A. Ankiewicz, *Dissipative solitons: from optics to biology and medicine*, vol. 751 (Springer, 2008).

[204] H. Sakaguchi and B. A. Malomed, "Gap solitons in Ginzburg-Landau media," PHYSICAL REVIEW E **77** (2008).

[205] Y. V. Kartashov, V. V. Konotop, V. A. Vysloukh, and L. Torner, "Vortex lattice solitons supported by localized gain," OPTICS LETTERS **35**, 3177 (2010).

[206] T. J. Alexander, M. Salerno, E. A. Ostrovskaya, and Y. S. Kivshar, "Matter waves in anharmonic periodic potentials," PHYSICAL REVIEW A **77** (2008).

[207] T. Anker, M. Albiez, R. Gati, S. Hunsmann, B. Eiermann, A. Trombettoni, and M. Oberthaler, "Nonlinear self-trapping of matter waves in periodic potentials," PHYSICAL REVIEW LETTERS **94** (2005).

[208] T. Alexander, E. Ostrovskaya, and Y. Kivshar, "Self-trapped nonlinear matter waves in periodic potentials," PHYSICAL REVIEW LETTERS **96** (2006).

[209] J. Wang, J. Yang, T. J. Alexander, and Y. S. Kivshar, "Truncated-Bloch-wave solitons in optical lattices," PHYSICAL REVIEW A **79** (2009).